The impact of surface modifications on the properties of α-$SnWO_4$ photoanodes for photoelectrochemical water splitting

vorgelegt von

M. Sc.

Patrick Schnell

an der Fakultät II – Mathematik und Naturwissenschaften

der Technischen Universität Berlin

zur Erlangung des akademischen Grades

Doktor der Ingenieurwissenschaften

- Dr.-Ing. -

genehmigte Dissertation

Promotionsausschuss:

Vorsitzender: Prof. Dr. Maria Andrea Mroginski

Gutachter: Prof. Dr. Roel van de Krol

Gutachter: Prof. Dr. Menny Shalom

Tag der wissenschaftlichen Aussprache: 18. November 2021

Berlin 2021

Abstract

Increasing pollution and global warming will challenge the life of humanity on planet Earth in the 21st century and beyond. In order to mitigate the impact on environment, society, and economy, the shift towards a renewable energy system is inevitable. Hydrogen is a clean and renewable fuel that has the potential to become an essential part of the future energy system. A potential low-cost and resource-saving production route for hydrogen is photo-electrochemical water splitting. Semiconductor materials are the key component in this process, which are required to split water into hydrogen and oxygen with the help of sunlight. In order to become economically viable, the semiconductor materials should ideally be made from cheap and earth-abundant elements. These criteria can be met by metal oxide photoelectrodes. Although significant research efforts have been devoted to the search for suitable materials, the ideal photoabsorber has not been found thus far. A promising photoelectrode material is α-$SnWO_4$, which recently has been prepared by pulsed laser deposition. However, the factors that limit the performance of α-$SnWO_4$ are not yet understood.

Several challenges of α-$SnWO_4$ and α-$SnWO_4$/NiO_x photoelectrodes are addressed in this thesis. First, the photovoltage limitation is investigated in detail. The photoelectrochemical analysis of the α-$SnWO_4$ and α-$SnWO_4$/NiO_x films verified the photovoltage limitation, which depends on the NiO_x layer thickness. The combination of synchrotron-based hard X-ray photoelectron spectroscopy, density functional theory calculations, and Monte Carlo-based peak intensity simulations suggested the formation of a thin oxide layer at the interface of α-$SnWO_4$ and NiO_x. Such a layer can not only affect the photocurrent of the sample negatively, but also the photovoltage. In the further analysis, a relation between the oxide layer thickness and the photovoltage loss was indeed found.

The next part aimed for more detailed understanding of the reason for the photovoltage loss. Surface photovoltage measurements suggested the modification of the charge redistribution and relaxation in α-$SnWO_4$ films upon deposition of NiO_x. The interface between α-$SnWO_4$ and SnO_2, which represents the nature of the proposed interfacial layer, was investigated by hard X-ray photoelectron spectroscopy. Overall, the combination of surface photovoltage measurements and photoelectron spectroscopy suggested the presence of intra-band gap states. These states are proposed to be responsible for the observed photovoltage loss.

For the practical production of hydrogen, the (photo)electrochemical stability is an essential requirement of a photoelectrode material. The stability of α-$SnWO_4$ films was investigated in

detail as a function of the photoelectrochemical conditions. Strong dependence of the stability on the pH of the electrolyte was found by a combination of inductively coupled plasma - optical emission spectroscopy, X-ray photoelectron spectroscopy, and X-ray diffraction. The experimentally observed stability window is compared with a theoretical potential-pH (Pourbaix) diagram. More insight into the stability was obtained by in-situ spectro(photo)electrochemistry measurements. Moreover, the self-passivation of α-$SnWO_4$ is demonstrated in neutral pH electrolyte. This inhibits further film dissolution by the formation of a passivating oxide layer on the surface of α-$SnWO_4$. Due to the self-passivation effect, the presence of pinholes in the protection layer will not lead to corrosion of the film underneath the protection layer. Overall, this work provides important understanding of α-$SnWO_4$ photoelectrodes. This understanding provides the basis for the development of suitable strategies to further enhance the performance of α-$SnWO_4$ photoelectrodes.

Kurzfassung

Zunehmende Luftverschmutzung und globale Erwärmung sind eine Herausforderung für das Leben der Menschheit im 21. Jahrhundert und darüber hinaus. Um die Auswirkungen auf die Umwelt, Gesellschaft und Wirtschaft abzumildern, ist ein Übergang in ein nachhaltiges Energiesystem unerlässlich. Wasserstoff ist ein sauberer und regenerierbarer Brennstoff, der das Potenzial hat ein entscheidender Bestandteil in einem zukünftigen Energiesystem zu werden. Ein potenziell kostengünstiger und ressourcenschonender Ansatz für die Wasserstoffproduktion ist die photoelektrochemische Spaltung von Wasser. In diesem Verfahren sind Halbleitermaterialien das Schlüsselelement, um Wasser mit der Hilfe von Sonnenlicht in Wasserstoff und Sauerstoff aufzuspalten. Um ökonomische Rentabilität zu erreichen, sollten diese Halbleitermaterialien idealerweise mit kostengünstigen Ausgangsstoffen hergestellt werden, die auf der Erde ausreichend vorhanden sind. Diese Anforderungen können mit Metalloxid Photoelektroden erreicht werden. Obwohl mit großen Forschungsanstrengungen nach geeigneten Materialien gesucht wird, wurde ein idealer Photoabsorber bis jetzt nicht gefunden. Ein vielversprechendes Photoelektrodenmaterial ist α-$SnWO_4$, welches vor kurzem mit gepulster Laserablation hergestellt wurde. Allerdings wurden die Faktoren, die die Leistungsfähigkeit von α-$SnWO_4$ limitieren, bis jetzt noch nicht ausreichend verstanden.

Verschiedene Herausforderungen von α-$SnWO_4$ und α-$SnWO_4$/NiO_x Photoelektroden werden in dieser Arbeit behandelt. Im ersten Teil wird die Limitierung der Photospannung im Detail untersucht. Die photoelektrochemische Analyse der α-$SnWO_4$ und α-$SnWO_4$/NiO_x Proben bestätigte die Limitierung der Photospannung, die mit der NiO_x Schichtdicke zusammenhängt. Die Kombination von Synchrotron-basierter harter Röntgen-Photoelektronenspektroskopie, Dichtefunktionaltheorie Berechnungen und Monte-Carlo basierter Peak Intensitäts-simulationen deutete auf die Entstehung einer dünnen Oxidschicht an der Grenzfläche von α-$SnWO_4$ und NiO_x hin. Diese Schicht kann nicht nur den Photostrom limitieren, sondern auch die Photospannung. Tatsächlich wurde mir der weiteren Analyse eine Beziehung zwischen der Oxidschichtdicke und der Photospannung gefunden.

Der nächste Teil zielte auf ein noch genaueres Verständnis der zugrunde liegenden Ursache der Limitierung der Photospannung ab. Oberflächenphotospannungsmessungen an α-$SnWO_4$ Schichten deuteten auf die Modifikation der Ladungstrennung und Relaxation hin, hervorgerufen durch die Abscheidung von NiO_x. Die Grenzfläche zwischen α-$SnWO_4$ und SnO_2, welche die Eigenschaften der vorgeschlagenen Grenzflächenschicht repräsentiert, wurde ebenfalls mittels harter Röntgen-Photoelektronenspektroskopie untersucht. Insgesamt zeigt

die Kombination von Oberflächenphotospannungsmessungen und Photoelektronen-spektroskopie, dass Intraband-Zustände existieren. Es wird vorgeschlagen, dass diese Zustände für die beobachteten Photospannungsverluste verantwortlich sind.

Für die praktische Erzeugung von Wasserstoff ist die (photo)elektrochemische Stabilität eine entscheidende Anforderung an ein Photoelektroden Material. Die Stabilität von α-$SnWO_4$ Schichten wurde detailliert in Abhängigkeit der photoelektrochemischen Bedingungen untersucht. Eine starke Abhängigkeit der Stabilität von den Messbedingungen wurde gefunden, durch eine Kombination von optischer Emissionsspektroskopie mit induktiv gekoppeltem Plasma, Röntgenphotoelektronenspektroskopie und Röntgenbeugung. Der experimentell beobachtete Stabilitätsbereich wird mit einem theoretischen Potential-pH (Pourbaix) Diagramm verglichen. Weitere Einblicke in die Stabilität wurden durch spektro(photo)elektrochemische Messungen gewonnen. Außerdem wird die Selbstpassivierung von α-$SnWO_4$ Schichten in neutralen Elektrolyten demonstriert. Dieser Mechanismus verhindert die weitere Schichtauflösung durch die Bildung von passivierenden Oxidschichten auf der Oberfläche von α-$SnWO_4$. Durch die Selbstpassivierung führt das Vorhandensein von Pinholes in der Schutzschicht nicht zur Korrosion der α-$SnWO_4$ Photoelektrode. Insgesamt betrachtet stellt diese Arbeit wichtiges Verständnis von α-$SnWO_4$ Photoelektroden bereit. Dieses Verständnis bildet die Basis für die weitere Entwicklung geeigneter Strategien, um die Leistungsfähigkeit von α-$SnWO_4$ Photoelektroden weiter zu erhöhen.

Contents

1. Introduction

1.1. Global warming and the challenge of energy production

The continuing pursuit of humanity for economic growth and wealth is inevitably connected to a continuous increase of the world energy consumption. In the past, the energy demand has mainly been satisfied by a steady increase of fossil fuel consumption. For instance, in the year 2018 an annual increase of the energy consumption of 2.3 % was reported, which is even higher than the long-term annual average increase of 1.3 %. In total an estimated ~19 TW of energy was consumed in 2018 compared to ~13 TW in 2000. The share of fossil fuels in 2018 was 81 %, and was more or less the same as in the year 2000. At the same time a significant increase of the energy related CO_2 emission was observed, from ~23 Gt in 2000 to ~33 Gt in 2018.[1] In addition to CO_2, other greenhouse gases are emitted such as methane and nitrous oxide, which have an even stronger greenhouse effect than CO_2.[2-3] Projected into the future, a significant increase of the energy demand is expected. One of the main driving forces for this increasing demand is the increase of the world population.[1, 4]

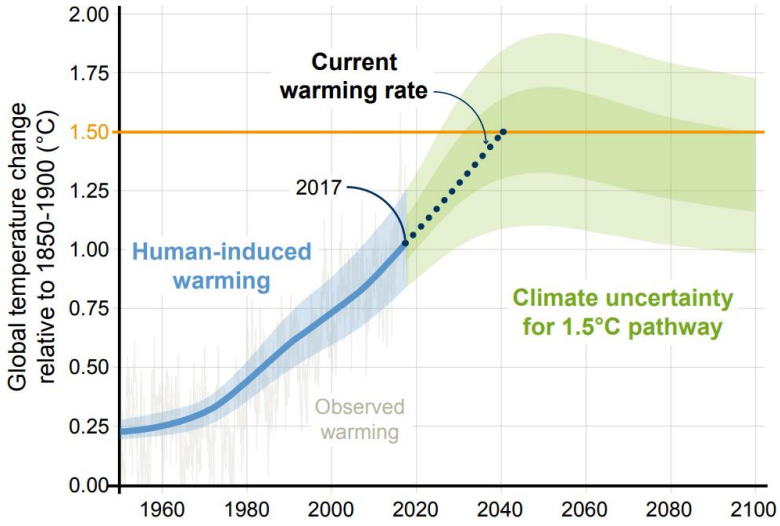

Figure 1.1. Change of the global average temperature due to human-induced warming in the past, and projection into the future. The temperature change is defined by the deviation from the 30-year global average. With the current rise of the average temperature of 0.2 ± 0.1°C per decade, the 1.5°C threshold would be reached in 2040. Different mitigation strategies for greenhouse gas reduction result in a relatively large "climate uncertainty" for the 1.5°C pathway. Figure adapted from the 2018 IPCC special report, chapter 1, page 82.[5]

The significant increase of greenhouse gases in the atmosphere has been accompanied by a steady increase of the global average temperature as shown in Figure 1.1. A severe impact of the rising average temperature and CO_2 concentration on ecosystems is expected as well as the

occurrence of extreme weather events.[6-9] The threat of climate change directly or indirectly affects all humans living on this planet and can only be tackled by cooperative efforts. Within the United Nations the Intergovernmental Panel on Climate Change (IPCC) tries to find a common pathway for the mitigation of further global warming and its impacts. As formulated in the 2015 Paris agreement, global warming should be ideally limited to 1.5°C or at least well below 2°C. When extrapolating the current rate of temperature change of 0.2 ± 0.1°C per decade, the 1.5°C limit would already be reached in 2040. As discussed in the IPCC special report in 2018, several strategies exist to stay within the limit of 1.5°C.[10] All of them are based on a significant reduction of CO_2 to a net zero emission or even negative CO_2 emission. The outcomes of these different mitigation scenarios are projected to lie within the green shaded "climate uncertainty" for the 1.5°C pathway in Figure 1.1.

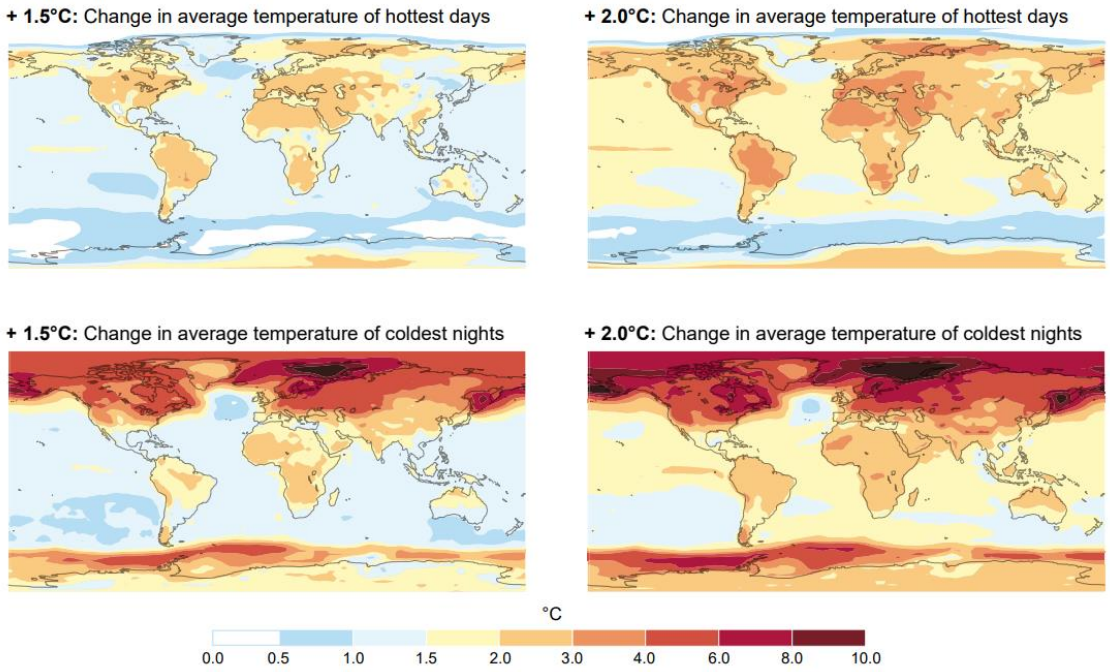

Figure 1.2. Projected impact of an average global warming of 1.5°C and 2°C. The local change in temperature is indicated for the extreme cases of the average temperature of hottest days and coldest nights. The local change of temperature can be well above the average temperture change. Figure adapted from the 2018 IPCC special report, chapter 3, page 283.[11]

It is important to understand how severe the effects of seemingly small differences in the average temperature can be. In Figure 1.2 the local temperature changes in the 1.5°C and 2°C scenarios are projected. A comparison of the extreme cases of the temperature change of the hottest days with the change in the coldest nights shows locally higher temperature rises than expected from the average difference of 0.5°C. Overall, the increase of the temperature is not evenly distributed across the globe. Continental areas experience a higher increase than

oversea areas. Specific regions may experience a significantly higher temperature rise than the average. Although it is highly challenging to stay within the 1.5°C pathway, this is still considered to be feasible.[5, 10] In any case, these projections emphasize the urgent need for sustainable energy sources.

1.2. Hydrogen as an energy carrier in a future sustainable energy system

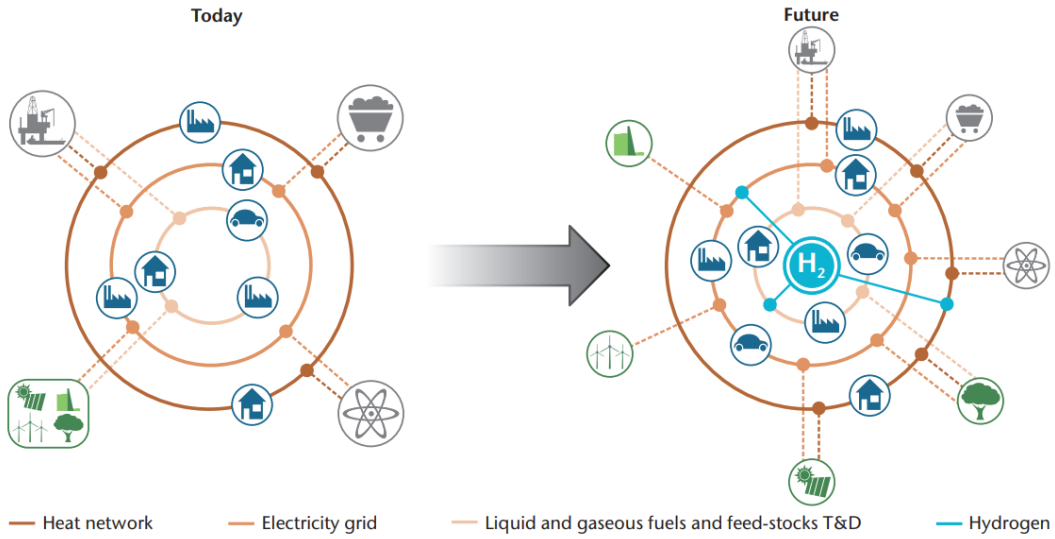

Figure 1.3. Illustration of the transition into of a future sustainable energy system with H_2 as a central energy carrier in combination with several other sustainable energy production routes. Adapted from reference [12].

Several strategies are available to generate energy from renewable sources.[13-14] For instance, electricity can be generated in large amounts by wind turbines, solar cells, or from bio-mass. Among the different renewable energy sources, sunlight has the highest potential for power generation.[15] However, the intermittent (seasonal and diurnal) nature of sunlight as well as the often-low sunlight intensity in northern countries are limitations. Energy therefore needs to be transported from places with high sun intensity and/or needs to be stored in some way. Storage of energy is one of the main challenges for a sustainable energy society. One possibility is to store electricity using batteries, as for instance used in electric cars.[16-17] On the other hand, energy may be stored in the form of chemical fuels. These have the advantage of a higher energy storage density compared to batteries.[15] Chemical fuels also have the advantage of an already existing infrastructure, much of which can be easily modified for the specific needs of the respective fuels. In principle, CO_2 can be used as a feedstock for the production of chemical fuels. This is, however, difficult to achieve in practice and a more promising approach is the use of H_2. [18-19] Hydrogen can play a central role in the transition to a future sustainable energy system as schematically illustrated in Figure 1.3. In this scenario, H_2 is the main energy vector

of the energy system in combination with electricity. H_2 can be directly used as an energy carrier in fuel cells,[20] or hydrocarbons may be synthesized from H_2 and used as chemical fuel.[15] This can be done on the basis of well-established Fischer-Tropsch processes.[21] The usage of H_2 as energy carrier has several advantages. Combustion of H_2 results in low pollution and H_2 is generally non-toxic.[22] Also the infrastructure for chemical fuels is already established. Although storage of H_2 can be challenging, mainly because of the low volumetric energy density of H_2, several storage options exist. For instance, high-pressure tanks, metal organic frameworks (MOFs), or metal hydrides.[23-24] Of course, H_2 also needs to be produced. Several routes for H_2 production are available. Currently, however, large amounts of H_2 are produced with conventional techniques relying on fossil fuels. Several chemical approaches exist such as thermal decomposition (pyrolysis), partial oxidation, and steam reforming of fossil (hydro)carbons.[22] In these processes a syngas is produced, which contains H_2 and CO. This is followed by the water-gas shift reaction, which results in the generation of CO_2. Consequently, H_2 produced in this way cannot provide the basis for a sustainable H_2 economy. In addition to the use of H_2 as energy carrier, H_2 is an important feedstock for the large-scale production of NH_3 via the Haber Bosch process.[25] NH_3 is an important basis for the production of fertilizers.[26] We should keep in mind that the fertilizer production is of eminent importance for the world food production, and also here a sustainable H_2 source is urgently needed.

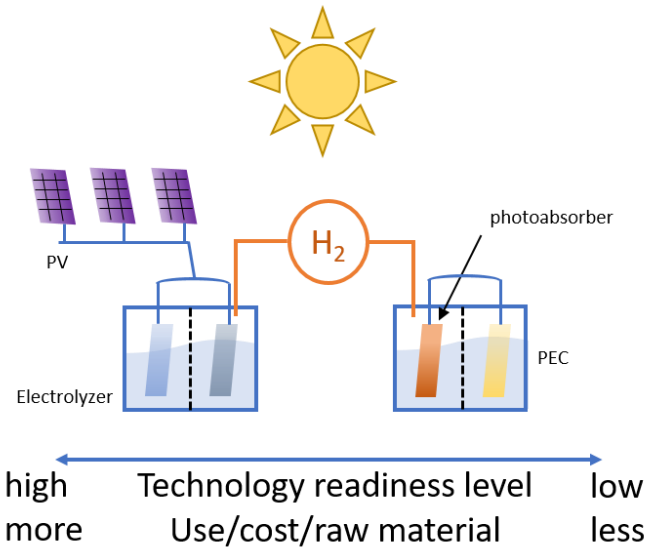

Figure 1.4. Comparison of two different technologies for solar hydrogen production. On the top left side electrolysis based on photovoltaics (PV-electrolysis) is schematically illustrated, and on the right side photoelectrochemistry (PEC) is shown. This illustration was made on the basis of figure 1 in reference [27].

Alternatively, H_2O can be used as an abundant source for the sustainable sunlight-driven production of H_2. The existing strategies can be classified into electrolysis based on photovoltaics (PV-electrolysis) and photoelectrochemistry (PEC).[27-29] In PV-driven electrolysis, two independent components are used. The photovoltaics component (i.e., one or multiple solar cells) provides the voltage needed to drive the second compartment, the electrolyzer. This can either be an alkaline electrolyzer[30] or a proton exchange membrane (PEM) electrolyzer.[27] The latter one is more technologically advanced and provides higher current densities and efficiencies, but is also more expensive.[27] In the PEC approach only one integrated component is required. The "light harvesting element" (i.e., the photoabsorber) is here directly part of the H_2 generator. This can reduce the cost and the use of raw material as illustrated in Figure 1.4. The device integration in the PEC approach is an important advantage in comparison to PV-electrolysis. However, the technological readiness level of PEC is clearly lower compared to PV-electrolysis. When comparing the demonstrated efficiencies of both approaches, PV-electrolysis has an advantage. A solar-to-hydrogen efficiency (STH) of 30 % has been demonstrated for 48 h, with a combination of a PEM electrolyzer and a triple-junction solar cell.[31] For a similar time period of > 40 h an STH efficiency of 10 % was demonstrated for a PEC device.[32] Reports with higher efficiencies exist as well, but are not demonstrated for comparable time periods.[33-34] Further advantages of PEC water splitting are the lower current densities, and thus lower required overpotentials as well as the better heat management. In a PEC cell, the sunlight induced heating can lead to an improvement due to enhanced electrochemical kinetics, in contrast to a PV-electrolyzer setup, where heating of the photovoltaic component results in efficiency losses.[35-37] Recently it was shown that good thermal management is important to operate a PEC device at -20°C.[38] Similar temperatures can be found in many places on the globe. Consequently, this demonstration further broadens the versatility of PEC-based water splitting devices.

For the further development of PEC water splitting, several aspects need to be addressed. Most importantly, a suitable semiconducting material needs to found. This is the key component in a PEC waster splitting device. Suitable materials may be found in the class of metal oxide semiconductors, as discussed in more detail in the following sections. At the same time, efforts are required on device upscaling, engineering, and simulation.[39-41] Economic viability of PEC devices is another important aspect that will determine the success of this technology in the coming decades.[42-45]

1.2. Photoelectrochemical water splitting

In a typical photoelectrochemical (PEC) setup, a suitable semiconductor is immersed in an electrolyte solution as schematically depicted in Figure 1.5. A simplified description based on literature is as follows:[46-47] the semiconductor is irradiated with (simulated) sunlight. The absorption of photons with an energy larger than the band gap of the semiconductor generates electron-hole pairs. In the case of a photoanode (i.e., n-type semiconductor) the holes (h^+) are moving to the surface and drive the oxygen evolution reaction (OER). Through an external wire, electrons (e^-) are transported to the counter electrode, which is in the simplest configuration a metal such as Pt. This is immersed in the electrolyte solution as well. The hydrogen evolution reaction (HER) proceeds here by the consumption of the electrons. The half reactions of the OER and HER depend on the pH of the electrolyte and can be formulated for an alkaline medium as follows:

$$4H_2O + 4e^- \leftrightarrow 2H_2 + 4OH^- \qquad \text{HER (1.1)}$$

$$4OH^- + 4h^+ \leftrightarrow 2H_2O + O_2 \qquad \text{OER (1.2)}$$

The same reactions can also be defined for acidic media:

$$4H^+ + 4e^- \leftrightarrow 2H_2 \qquad \text{HER (1.3)}$$

$$2H_2O + 4h^+ \leftrightarrow O_2 + 4H^+ \qquad \text{OER (1.4)}$$

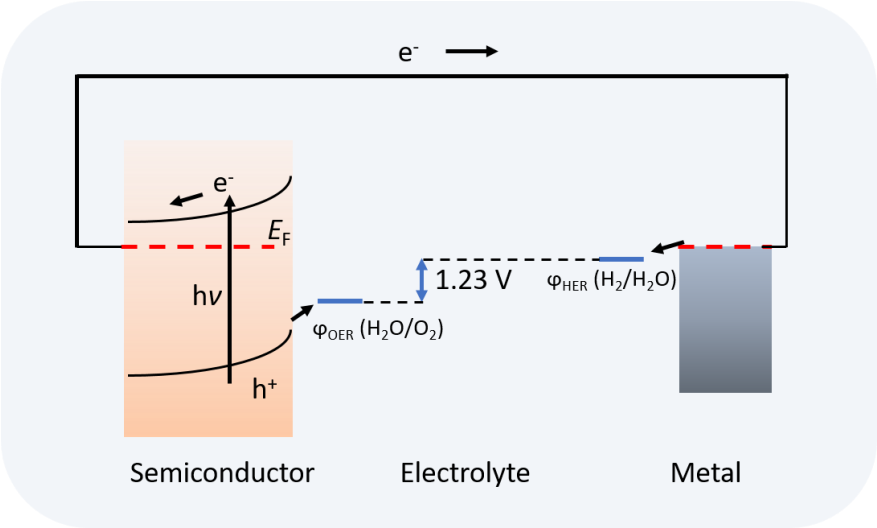

Figure 1.5. Schematic illustration of a photoelectrochemical cell consisting of a single photoabsorber and a metal counter electrode. The oxygen evolution reaction (OER) takes place at the photoanode and the hydrogen evolution reaction (HER) takes place at the (metal) counter electrode. The redox potentials of water, φ_{OER} (H_2O/O_2) and φ_{HER} (H_2/H_2O), are indicated.

Based on the half reactions, the overall water splitting reaction can be formulated in equation 1.5. The reaction is thermodynamically uphill and a Gibbs free energy of ΔG = 237.2 kJ mol^{-1} needs to be invested to enable the reaction. As defined in equation 1.6, this can be translated to 1.23 eV per electron and consequently ΔE = 1.23 V.

$$\text{Overall reaction: } 2\mathrm{H_2O} \leftrightarrow 2\mathrm{H_2} + \mathrm{O_2} \quad \Delta G = 237.2 \text{ kJ mol}^{-1} \tag{1.5}$$

$$\Delta G = -nF\Delta E \tag{1.6}$$

Here, F is the Faradaic constant and n describes the number of electrons. ΔE defines the minimum photovoltage required to drive the water splitting reaction, when using a single photoabsorber.

An important property of a water splitting device is the solar-to-hydrogen (STH) efficiency as defined in equation 1.7. J_{photo} is the photocurrent density and V_{redox} is 1.23 V. The power of the incident light is given by P_{in}. For AM1.5 illumination this corresponds to 1000 mW m^{-2}. In this definition, it is assumed that no bias voltage is applied between the working and counter electrodes and that the faradaic efficiency is 1.

$$\mathrm{STH}\ (\%) = \frac{V_{\mathrm{redox}} \times J_{\mathrm{photo}}(\mathrm{mA\ cm^{-2}})}{P_{\mathrm{in}}(\mathrm{mW\ cm^{-2}})} \tag{1.7}$$

In addition to J_{photo}, the photovoltage is an important metric. The origin of the photovoltage is conceptually described for a photoanode in Figure 1.6. Here, E_{CB} denotes the conduction band minimum energy and E_{VB} the valence band maximum energy. For the sake of simplicity, in this description it is assumed that in contact with water under dark equilibrium conditions, the Femi level E_F of the semiconductor equilibrates with the redox potential of the liquid φ_{OER} (H_2O/O_2). In reality, however, this is not necessarily the case. There is considerable uncertainty of the *exact* position of E_F under equilibrium conditions in the dark. The exact position of E_F depends, for instance, on the electrochemical reaction that dominates in the dark. At the surface of the semiconductor band bending is present. The band bending can result from the dissociative adsorption of water molecules at the surface.[15] Electronic states in the band gap can then be formed by OH^- groups at the surface. These electronic states are occupied by electron transfer from the semiconductor. The depletion of electrons at the surface of the semiconductor results in an increase of the ionized donor density. Consequently, a space charge layer is formed, which has a width W. In an aqueous solution (water) OH^- and H^+ ions from the liquid are adsorbed on the surface in an dynamic equilibrium.[15] Ions in solution are surrounded by attached water molecules. The distance between the adsorbed ions on the surface and the closest ions in the

solution is defined as the Helmholtz layer, which has a width W_H of typically 2 - 5 Å.[15] Across the Helmholtz layer a potential drops in the order of ~0.1 - 0.5 eV.[15]

Under illumination the equilibrium condition is not valid anymore, and as indicated in Figure 1.6b, the Fermi level splits up in the quasi Fermi levels of the electrons $E_{qF,n}$ and holes $E_{qF,p}$. The photovoltage ΔV_{photo} depends on the splitting of the quasi Fermi levels. For the sake of brevity, the underlying physical principles of semiconductors are not discussed in more detail here, and can be found elsewhere.[15]

Another important metric in PEC water splitting is the flatband potential. This is defined as the potential that needs to be applied to achieve a flat band situation.[15, 48] For an n-type semiconductor this potential is, in theory, the most negative potential at which a photocurrent can still be observed. In practice, however, potentials more positive than the flatband potential usually need to be applied to extract a photocurrent. This may have several origins such as surface charge accumulation or recombination in the space charge layer.[15, 49]

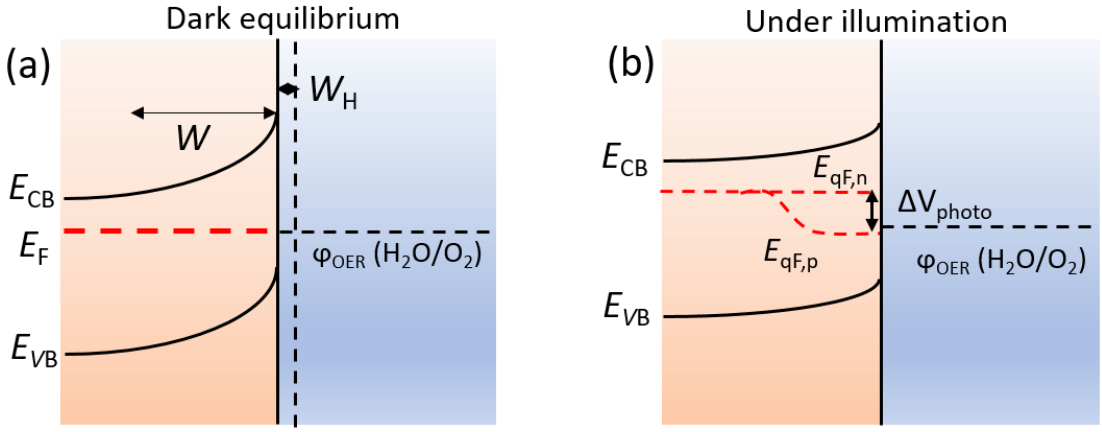

Figure 1.6. Schematic illustration of a semiconductor-liquid junction. (a) In this illustration it is assumed that under dark equilibrium conditions, the Fermi level E_F equilibrates with the redox potential φ_{OER} (H_2O/O_2). E_{CB} denotes the conduction band minimum and E_{VB} the valence band maximum. W denotes the width of the space charge layer and W_H the width of the Helmholtz layer. (b) Under illumination the Fermi level splits up into the quasi Fermi levels $E_{qF,n}$ of electrons and $E_{qF,p}$ of holes. The photovoltage ΔV_{photo} depends on the splitting of the quasi Fermi levels.

1.3. Material requirements for photoelectrochemical water splitting

For solar water splitting suitable materials need to be chosen. Several requirements have to be considered.[46, 50-52] In a suitable semiconductor a sufficient amount of charge carriers needs to be generated upon illumination with sunlight. Therefore, the semiconductor needs to be able to absorb photons from the solar spectrum, which is shown in Figure 1.7a. The energy of photons that can be absorbed is defined by the band gap energy of the semiconductor.[50] From a thermodynamic point of view, a band gap of at least 1.23 eV is required to drive the PEC

reaction. With the addition of overpotentials, the band gap needs to be at least 1.9 eV.[15] Overpotentials arise from thermodynamic losses and several kinetic losses.[53-54] Above ~390 nm the intensity in the solar spectrum significantly decreases and, therefore, the band gap is limited to a maximum of ~3.1 eV.[15] Although, in principle, a photocurrent may be generated with a material having such a band gap, a band gap close to ~3.1 eV is far from ideal. This becomes clear when using the AM1.5G photon flux to calculate the theoretical photocurrent density J_{max} in dependence on the band gap of the absorbing semiconductor. In this calculation, it is assumed that 100 % of the incident photons participate in the generation of charge carriers, i.e., the incident photon-to-current efficiency (IPCE) is 100 %. J_{max} is shown in Figure 1.7b as a function of the band gap, where J_{max} increases with decreasing band gap. Decreasing the band gap of the photoabsorber, however, will only result in an enhancement of efficiency up to a certain point, as there exists a tradeoff between photocurrent and photovoltage.[15] In Figure 1.8a the theoretical STH efficiency of a single photoabsorber is shown as a function of the band gap. The maximum efficiency of 11.2 % is calculated for a band gap of 2.26 eV. In this model an overall loss of ~0.49 eV is assumed. The application of Pt and RuO_2 catalysts is assumed and shunt losses are neglected.[45, 55]

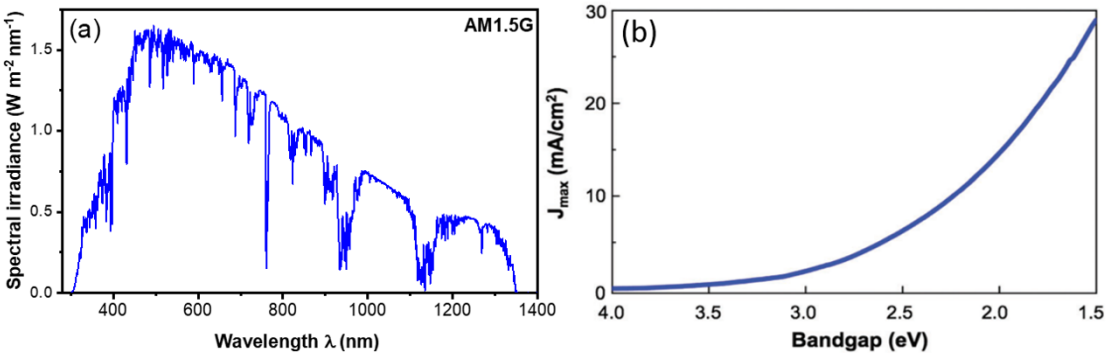

Figure 1.7. (a) AM1.5G solar spectrum (The American Society of Testing and Materials (ASTM) G173). The data were taken from reference [56]. (b) Dependence of theoretical maximum photocurrent density J_{max} on the band gap of the material. Here it is assumed that all photons of the solar spectrum contribute in the generation of the photocurrent (i.e., the incident photon-to-current efficiency is 100 %). Reprinted with permission from reference [50]. Copyright 2019, The Royal Society of Chemistry.

Not only the size of the band gap is important, but also the relative positions of the valence and conduction band edges (VBM and CBM) with respect to the oxidation and reduction potentials of water. This determines the thermodynamic driving force of electrons or holes during the PEC operation. For a sufficient thermodynamic driving force, the CBM should be more negative than the hydrogen evolution potential and the VBM should be more positive than the oxygen evolution potential. This is commonly expressed as the band edges straddling the water reduction and oxidation potentials.[15]

In contrast to the assumed 100 % IPCE for the calculation of J_{max}, in reality not all photons contribute to the photocurrent. Therefore, the number of photons that are actually absorbed by the semiconductor need to be considered. This material property is described by the absorption coefficient $\alpha(\lambda)$. Especially for the visible wavelength region a high $\alpha(\lambda)$ is required, which becomes clear when considering the high intensity of the solar spectrum in this region. By including the absorption properties of the material, the expected photocurrent density J_{abs} is defined. The absorbed photon-to-current efficiency (APCE) in this metric is 100 %. In practice, however, the APCE is lower than 100 %. For a more realistic description, the fraction of mobile charge carriers that are generated by absorption needs to be considered. A substantial fraction of the absorbed photons may result in localized charge carriers that do not contribute to the photocurrent. This property is described by the wavelength-dependent photogeneration yield $\xi(\lambda)$.[57] The measured photocurrent J_{PEC} can now be defined in dependence of J_{abs} and $\xi(\lambda)$:

$$J_{\mathrm{PEC}} = J_{\mathrm{abs}} \cdot \xi(\lambda) \cdot \eta_{sep} \cdot \eta_{\mathrm{in}} \tag{1.8}$$

The photogeneration yield factor $\xi(\lambda)$ was not considered in the earlier formulations of this equation in the literature,[50, 58-60] and is included here motivated by the recent study by Grave et al.[57] J_{PEC} further dependents on the separation efficiency η_{sep} and the injection efficiency η_{in}. In order to participate in the OER and HER, the mobile charge carriers need to be separated trough out the material and collected at the surface contacts. This is described by η_{sep} and strongly depends on the charge transport properties, i.e., the conductivity of the material. The conductivity depends on the carrier mobility and concentration. In addition to intrinsic factors that determine the mobility, such as the electronic structure, also extrinsic factors, such as the crystallinity or impurities, can influence the conductivity. To describe the overall transport properties, the diffusion length L_D of the minority charge carriers can be used. As defined in equation 1.9, this depends on the diffusivity D and the carrier lifetime τ. The diffusivity depends on the mobility μ and the temperature T.[15]

$$L_{\mathrm{D}} = \sqrt{D \cdot \tau} = \sqrt{\frac{\mu k_B T}{q} \cdot \tau} \tag{1.9}$$

In practice, not all charge carriers will reach the surface, which reduces η_{sep}. Consequently, good charge transport properties are desired for the semiconductor. In addition, the efficiency of the charge carrier injection into the electrolyte is implemented in the description by the injection efficiency. η_{in} depends on the reaction kinetics at the interface. Poor surface reaction kinetics can result in charge accumulation at the surface and charge recombination. η_{in} should ideally be high for a good photoabsorber material, but can also be improved significantly with the help

of catalysts. To test the potential of a material independent on η_{in}, a scavenger such as sulfite or H_2O_2 can be used.[61]

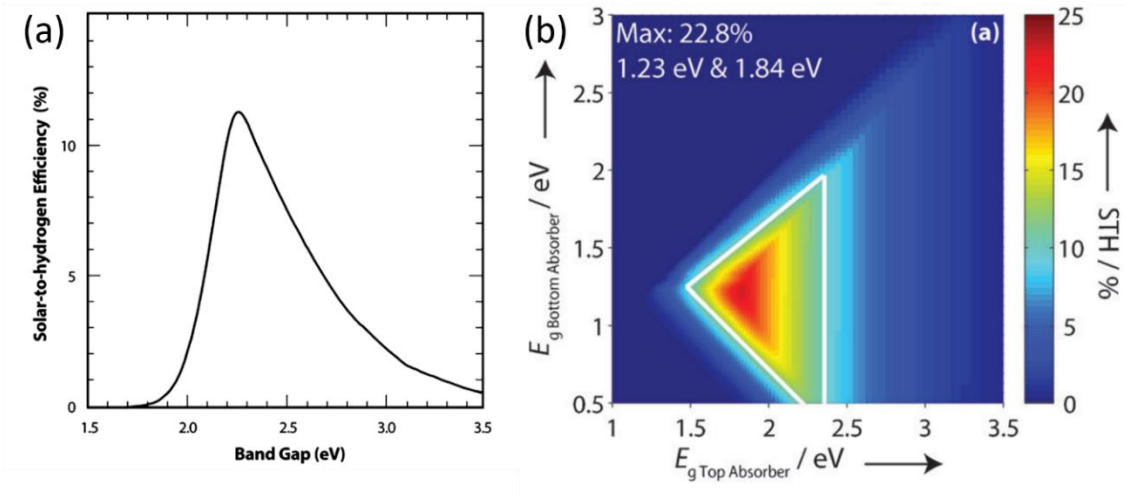

Figure 1.8. (a) STH efficiency of a single photoabsorber as a function of the band gap. Reprinted with permission from reference [45]. Copyright 2013, The Royal Society of Chemistry. (b) STH efficiency of a stacked D4 tandem configuration as a function of the band gap of the bottom and top absorber. The maximum efficiency is achieved for a bottom absorber with a band gap of 1.23 eV and a top absorber with a band gap of 1.84 eV. In the model an overall loss of ~0.49 eV is assumed. Highly active Pt and RuO_2 catalysts and no shunt losses are assumed. Reprinted with permission from reference [55]. Copyright 2014, John Wiley and Sons.

For an economically viable long-term operation, the semiconductor should be stable in dark and under illumination, as described in more detail in Chapter 1.6. Finally, the material should also be of low-cost and earth-abundant. A class of semiconductor materials, which can comply with these requirements, is discussed in the next section.

The overall STH efficiency does not only depend on the properties of the semiconductors, but also on the device configuration. Beyond the simple configuration in Figure 1.5, where a single photoabsorber is illustrated (S2 configuration, i.e., 2 photons are required to produce one H_2 molecule), significantly higher efficiencies can be achieved by combining two absorbers materials.[62] In Figure 1.8b the calculated STH efficiency is shown as a function of two absorber materials in a stacked D4 tandem configuration (dual absorber, four photons needed to produce one H_2 molecule). In this model calculation, a maximum STH efficiency of 22.8 % can be achieved with a band gap combination of 1.84 eV and 1.23 eV.[45, 55] Band gap combinations within the white triangle can provide efficiencies > 10 %. Although the shown STH efficiency is significantly lower than the thermodynamic limit of 41 %, the calculation is based on a rather ideal model with kinetic losses of ~0.49 eV. In addition, the application of highly active Pt and RuO_2 catalysts is assumed, and shunt losses are excluded in the calculation. Including further losses in the

model will reduce the maximum efficiency and change the ideal band gap combination.[45] Alternatively, a side-by-side configuration of two photoabsorbers is possible. A lower maximum efficiency of 15.5 % was calculated with two identical band gaps of 1.59 eV.[55] Depending on the available band gap combinations, however, this configuration may also be viable. Overall, these considerations show that in order to achieve efficiencies exceeding 10 %, tandem device configurations are necessary.[55]

1.4. Metal oxide photoelectrodes

Photoelectrochemical water splitting was observed for the first time with a metal oxide semiconductor. In the year 1972 Honda and Fujishima reported water oxidation on TiO_2.[63] Although a significant amount of studies has been performed on this material over the past decades,[64-66] a clear limitation of this material is the large band gap of 3.2 eV, and hence the low theoretical efficiency. Materials with smaller band gaps were required to achieve higher efficiencies. Over the years significant improvements have been achieved using Si[67-69] or III-V semiconductor compounds such as $GaInP_2$ and InP.[70-74] Although high efficiencies could be achieved in various reports,[34, 70] there are some aspects which limit the scalability of these materials. High demands on the fabrication process as well as in some cases involvement of rare elements result in high production costs.[75] Low-cost, earth-abundant, and scalable materials that are easy to process are, therefore, urgently needed. This brings us back to metal oxide semiconductors, which are a promising class of materials meeting these requirements. They are generally more stable in aqueous media and easier to manufacture.[46] Despite offering promising properties, they also have limitations, for instance the often too large band gaps as in the case of TiO_2, and often poor absorption properties related to indirect band gaps. Another limitation is the poor charge transport properties related to small polaron hopping mechanism,[76-77] which is mainly a consequence of the ionic character of the chemical bonds in metal oxides. Typical charge carrier mobilities of metal oxides are in the range of 0.001 – 1 $cm^2\ V^{-1}s^{-1}$ and are, therefore, significantly lower than in materials with covalent bonding character such as Si.[76-78]

Significant efforts have been devoted to the development of improvement strategies and exploration of new candidates.[46, 50-51] A timeline illustrating some of the important developments over the years is depicted in Figure 1.9. Initially binary oxides such as TiO_2, WO_3, and Fe_2O_3 have been studied extensively.[46] Although several strategies have been employed to improve the performance of binary oxides, the success has been limited. More opportunities to adjust the PEC properties by modifying the composition and electronic structure are provided when the number of metal cations is increased. Ternary metal oxides have attracted significant

attention and provide ~19,000 possibilities.[79] With the vast amount of possibilities, however, comes the difficulty to find suitable candidates. Screening approaches based on computational data and experimental combinatorial screening approaches are promising options, to accelerate the investigation of these compounds.[80-83]

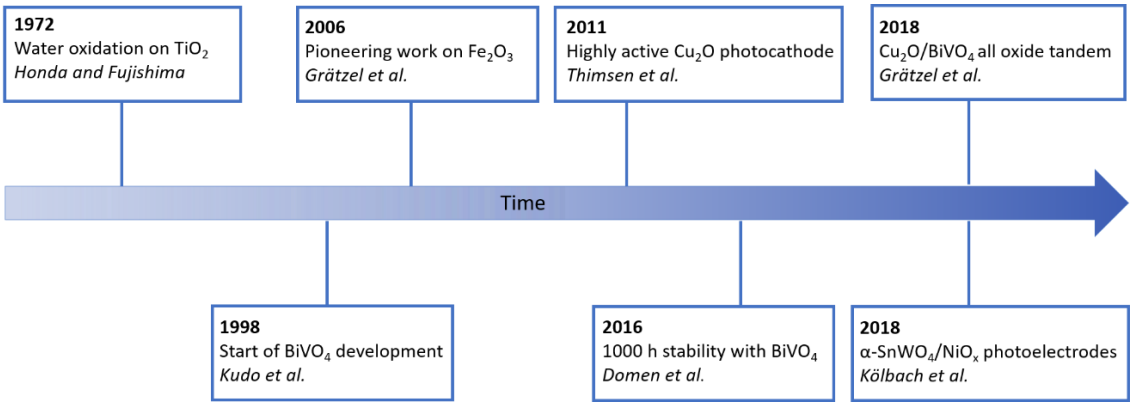

Figure 1.9. Timeline illustrating some of the important developments in the field of metal oxide photoelectrodes. The development started from the observation of photoelectrochemical water oxidation on TiO_2.[63] It continued over the development of $BiVO_4$, α-Fe_2O_3, Cu_2O photoelectrodes, and all-oxide tandem devices,[84-89] up to the investigation of novel photoelectrodes such as α-$SnWO_4$, to overcome the efficiency limitation of $BiVO_4$.[90-92] The figure is inspired by the review by Yang et al.[93]

Ternary metal oxides provided initially poor performance, but promising improvements could be demonstrated over the years.[50] The highest performing material thus far is $BiVO_4$, which has been studied since the late 1990s.[84, 94] In order to achieve this success, several strategies have been employed, not only for $BiVO_4$. This includes heteroatom doping,[95-97] crystallographic orientation control,[98] nanostructuring,[99-101] H_2 treatment,[102] deposition of protective, and catalytic overlayers.[89-90, 103-104]

The need for lower band gap materials has motivated the study of several emerging materials. Among them is α-$SnWO_4$, which is discussed in detail in the following section. Due to technological improvements, materials become interesting, which actually have too large intrinsic band gaps, but overall promising properties for water splitting. For instance, band gap reduction strategies can be used to achieve almost ideal band gaps with the perovskite material $BaSnO_3$, which intrinsically has a band gap larger than 3 eV.[105]

To achieve high STH efficiencies, tandem configurations are necessary as discussed in the previous section. Development of several devices has been reported with metal oxide materials.[86, 106-108] One example is shown in Figure 1.10. Here, a $BiVO_4$ top absorber is used, which is doped with W using a gradient in the doping concentration across the film thickness.

Cobalt phosphate (Co-Pi) is used as a catalyst. The bottom absorber is a double junction amorphous Si solar cell (2-jn-a-Si). An STH efficiency of 4.9 % was reported for this device.[109]

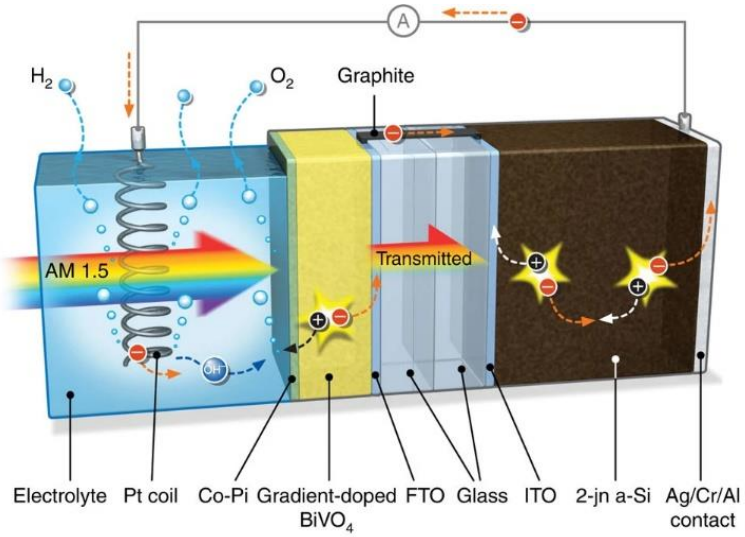

Figure 1.10. Tandem device for solar water splitting using a gradient-doped $BiVO_4$ top absorber with Co-Pi catalyst in combination with a double junction amorphous Si solar cell 2-jn-aSi solar cell as bottom absorber. Adapted by permission from reference [109], Copyright 2013, Nature Springer.

1.4.1. α-$SnWO_4$ thin film photoanodes

Another interesting material in the class of metal oxides is $SnWO_4$, which is an intrinsic n-type conductor, probably due to the presence of O-vacancies.[110] Among the two existing crystalline phases (α-phase and β-phase) only the α-phase shows photoelectrochemical activity. It crystalizes in an orthorhombic crystal structure (space group *Pnna*, a = 5.625 Å, b = 11.744 Å, c = 4.986 Å),[111] which is schematically illustrated in the a-b plane in Figure 1.11a. The cubic β-phase is stable above 670°C and has a band gap of ~4.1 eV and is, therefore, unsuitable for water splitting.[111-112] Thin film α-$SnWO_4$ photoelectrodes have been prepared by several deposition methods. Initially, films were prepared by hydrothermal conversion of WO_3 and SnO_2,[110, 113] and magnetron sputter deposition.[111, 114-115] Recently also pulsed laser deposition (PLD) has been used to deposit α-$SnWO_4$ films.[90-92] A band diagram of PLD-made α-$SnWO_4$ is shown in Figure 1.11b. In the figure the indirect band gap of 1.9 eV is indicated, which is reported for the PLD-made films.[90] In general, the reported band gap is in the range of 1.6 to 2.1 eV.[110, 113, 116] Under AM1.5 solar irradiation, the band gap of 1.9 eV corresponds to a theoretical maximum photocurrent of ~17 mA cm^{-2}. A theoretical STH efficiency of ~20 % is possible in a tandem configuration with a suitable bottom absorber such as Si. It should be noted, however, that the reported absorption coefficient is rather low in the visible wavelength regime above 450 nm. More than 10 µm film thickness would be required to achieve photocurrent densities close to the theoretical maximum.[90] Together with the limited charge

transport properties as described below in more detail, this may limit the achievable photocurrent density. A possible mitigation strategy could be based on nanostructuring.[90] In Figure 1.11b it can be seen that the conduction and valence band edges straddle the indicated oxidation potential $\varphi_{OER}(H_2O/O_2)$ and the reduction potential $\varphi_{HER}(H_2/H_2O)$ of water. This indicates the thermodynamic ability of electrons and holes to reduce and oxidize H_2O. Related to that, the flatband potential is located at ~0 V vs. RHE.[110, 113-114, 116] The density of states of pristine α-$SnWO_4$, calculated by density functional theory (DFT), is shown in Figure 1.11c. The valence band has mainly O 2p character hybridized with Sn 5s states and the conduction band is mainly formed by W 5d states.

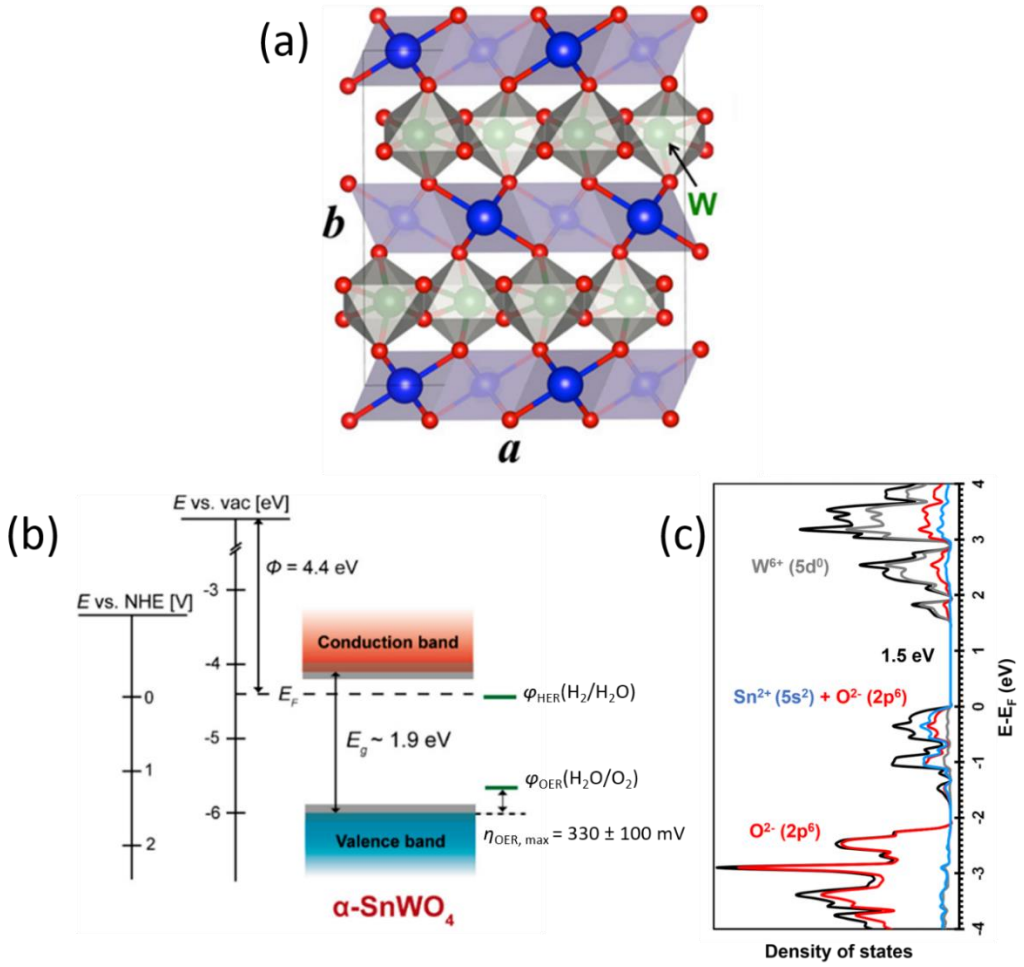

Figure 1.11. (a) Orthorhombic crystal structure of α-$SnWO_4$ shown in the a-b plane. In alternating layers Sn is tetrahedrally coordinated by O atoms, and W is octahedrally coordinated by O atoms. W atoms = green, Sn atoms = blue, O atoms = red. Reprinted with permission from reference [117]. Copyright 2020, American Chemical Society. (b) Band diagram of α-$SnWO_4$ including the relative positions of the thermodynamic oxidation potential $\varphi_{OER}(H_2O/O_2)$ and the reduction potential $\varphi_{HER}(H_2/H_2O)$ of H_2O. The reported work function ϕ of α-$SnWO_4$ is indicated as well. $\eta_{OER, max}$ is the maximum overpotential for the OER. Adapted from reference [118]. (c) Density of states for pristine α-$SnWO_4$ calculated by DFT. The valence band has mainly O 2p character hybridized with Sn 5s. The conduction band is mainly formed by W 5d states.

As often reported for metal oxide semiconductors, the charge transport properties can be a limitation for the PEC performance. For α-$SnWO_4$ the charge carrier dynamics were investigated in a recent study, where electron-hole mobilities up to 0.13 $cm^2 V^{-1} s^{-1}$ were reported.[91] This is a high value in comparison to other metal oxide photoelectrodes, but still clearly lower in comparison to Si.[78, 91] In addition, it was shown by a combination of time-resolved microwave conductivity (TRMC) and time-resolved terahertz spectroscopy (TRTS) that the (macroscopic) photoconductivity can be increased with an increase of the grain size.[91]

The photocurrent densities reported initially were very low, and were in the range of ~0.1 mA cm^{-2}.[113-114] This is typically correlated with fast surface oxidation of Sn^{2+} to Sn^{4+}. Significant improvement of the photocurrent could be achieved in 2018 by Kölbach et al.[90] Photocurrents of 0.75 mA cm^{-2} were reported for α-$SnWO_4$ films protected with a 20 nm NiO_x overlayer. It was suggested, however, that this also comes along with a limitation of the photovoltage.

Overall, α-$SnWO_4$ combines several promising properties for the development of water splitting devices. The band gap of 1.9 eV is very close to the calculated band gap of 1.84 eV for an ideal top absorber in a D4 tandem device.[55, 90] However, the challenges of α-$SnWO_4$ also need to be addressed. The main aspects reported in literature are the limited stability and the photovoltage limitation introduced by the NiO_x protection layer. Understanding and improvement of these aspects is crucial for the development of α-$SnWO_4$ films.

1.5. Surface states, interface states and Fermi level pinning

Fermi level pinning is a phenomenon observed for both semiconductor-metal (Schottky junction) and semiconductor-liquid junctions.[119-121] The origin can be found in the presence of surface or interface states, which can be classified into states with an intrinsic or extrinsic origin. Intrinsic states are, for instance, related to a broken translational symmetry at the surface of a material (i.e., dangling bonds). Extrinsic surface states can originate from surface defects or adsorbates. Depending on the mathematical description, surface states are often referred to Shockley or Tamm states.[122] Surface states in materials with covalent bonding character are typically described as Shockley states, and those in large band gap ionic materials as Tamm states.

When a semiconductor is contacted by a metal, band bending is introduced in the semiconductor. The magnitude depends on the difference of the work functions of both materials. This contact potential difference is compensated by the formation of a space charge region in the semiconductor (i.e., the band bending). At the interface a barrier $\varphi_{SB,n}$ is formed,

the height of which is given by equation 1.9 according to the Schottky-Mott theory, where ϕ_M is the work function of the metal and X_S the electron affinity of the semiconductor.[123-124]

$$\varphi_{SB,n} = \emptyset_M - X_S \quad (1.9)$$

In many practical cases, however, the barrier height does not depend linearly on the metal work function, as noted by Bardeen in a classical article in 1947.[121] The often observed independence of $\varphi_{SB,n}$ on ϕ_M can be explained by Fermi level pinning, although the formation of intermetallic phases may also play a role. Consequently, the amount of introduced band bending in the semiconductor may be limited by the presence of surface states. Depending on the density of surface states and the position of the Fermi level, the contact potential difference between metal and semiconductor is partially compensated by the filling or emptying of surface states, rather than the formation of a space charge region in the semiconductor.

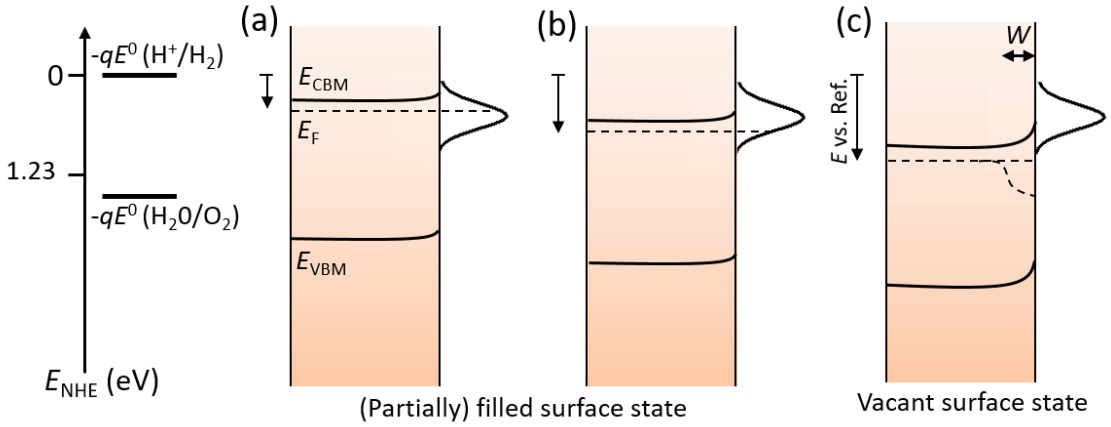

Figure 1.12. Schematic illustration of the effect of a high surface state density on the semiconductor-liquid interface. (a) Semiconductor-liquid junction with partially occupied surface states. (b) Increasing the applied potential reduces the amount of occupied surface states. Additional band bending is not introduced in the semiconductor, and the change in applied potential falls entirely across the Helmholtz layer. (c) A sufficiently large potential change can empty the surface states and shift the Fermi level below the density of surface states. Additional band bending is introduced in the semiconductor. From this point onwards, any change in applied potential falls across the space charge layer in the semiconductor, which has a width W.[125]

Similar effects can be observed for semiconductor-liquid junctions.[125] In Figure 1.12a an n-type semiconductor with a high density of surface states is part of a semiconductor liquid junction. The surface states are partially occupied. In (b) the magnitude of applied potential is increased, which only results in a change of the occupation of the surface states. The additional potential drops across the Helmholtz layer and in the semiconductor no additional band bending is introduced. When the magnitude of applied potential is sufficiently high, the Fermi level is shifted below the (now empty) surface states. Additional band bending is introduced in the

semiconductor as illustrated in Figure 1.12c. Since a higher bias potential needs to be applied to introduce a space charge layer, and thus generate a photocurrent, the effective photovoltage of the photoelectrode is reduced by the Fermi level pinning.[125]

1.6. (Photo)electrochemical stability of metal oxide photoelectrodes

As mentioned in Chapter 1.4, the stability of photoelectrodes is an important metric that needs to be understood and improved if necessary. The anodic or cathodic decomposition of an MX compound due to photoelectrochemical corrosion can be written as follows.[126]

$$MX + ne^- \rightarrow M + X^{n-} \tag{1.10}$$

$$MX + nh^+ \rightarrow M^{n+} + X \tag{1.11}$$

From a thermodynamic point of view, the stability can be defined via the relative positions of the self-oxidation (φ^{ox}) and reduction-potential (φ^{red}) of the material versus the VBM and CBM. The thermodynamic stability can then be defined by the Gerischer criteria as schematically depicted in Figure 1.13.[127-128] Based on this considerations, a photoanode can be expected to be stable when φ^{ox} is more positive than the VBM, and a photocathode can be expected to be stable when φ^{red} is more negative than the CBM. The thermodynamically stable phases are often shown in Pourbaix diagrams in dependence of potential and pH of the solution.[129-130]

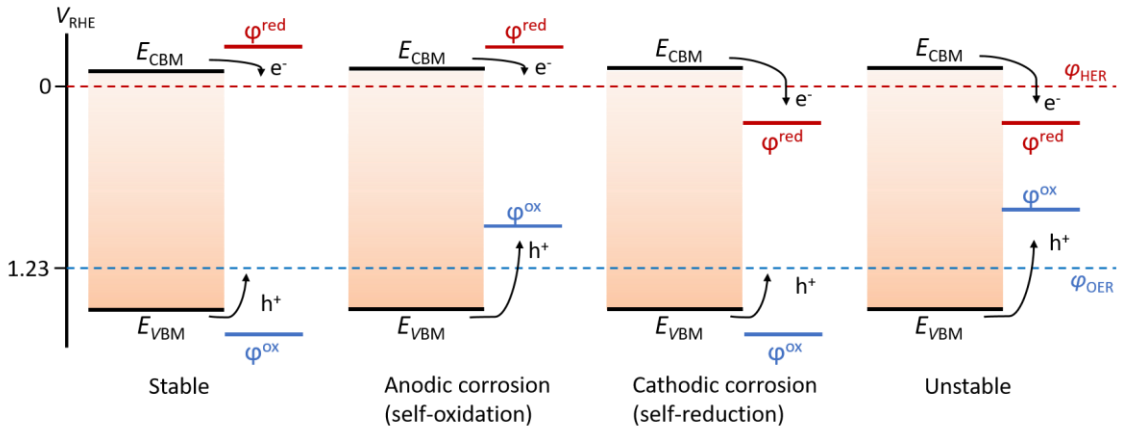

Figure 1.13. Schematic illustration of the evaluation of the stability of photoelectrodes based on a thermodynamic point of view. Stability depends on the relative positions of the thermodynamic self-oxidation (φ^{ox}) and self-reduction (φ^{red}) potentials of the material versus the VBM and CBM of the material.[126-128, 131]

In addition to thermodynamics, kinetic factors may impact the stability of a photoelectrode. Here, the rate constants of the reactions are important. They describe the ratios of charges consumed by the self-oxidation/reduction reaction and charges consumed by the OER or HER. The balance between these competing processes determines the overall stability. This suggests

also a possible mitigation strategy by enhancing the OER/HER reaction versus the self-oxidation/reduction reaction by application of catalysts. However, this will not help to reduce degradation in dark.[132]

1.7. This thesis

As outlined, there are several requirements and challenges in the search for suitable photoabsorber materials for solar water splitting. Several aspects of α-$SnWO_4$ photoanodes are addressed in this thesis, especially the impact of surface and interface modifications and the related challenges. The two main challenges are the limitation of the photovoltage in NiO_x-coated α-$SnWO_4$ films and the (photo)electrochemical stability.

The limitation of the photovoltage in α-$SnWO_4$/NiO_x samples is investigated in Chapter 3 and 4. First, synchrotron-based hard X-ray photoelectron spectroscopy (HAXPES) is combined with PEC analysis, and complemented with density function theory (DFT) calculations and Monte Carlo-based peak intensity simulations. Formation of a thin interfacial oxide layer at the interface of α-$SnWO_4$ and NiO_x is proposed. This oxide layer likely consists of SnO_2 and is correlated with the photovoltage limitation with the help of PEC control experiments.

The second part of the interface investigation is provided in Chapter 4. Modulated surface photovoltage (SPV) measurements suggested the modification of α-$SnWO_4$ upon deposition of NiO_x. Investigation of the interface of α-$SnWO_4$ and SnO_2 is performed as well, to clarify the nature of the interfacial layer structure. Valence band photoelectron spectroscopy complements the surface photovoltage analysis and confirms the presence of a state above the valence band maximum in the band gap. These observations are discussed with respect to the interfacial SnO_2 layer and photovoltage limitation found in the first part.

Finally, Chapter 5 is focused on the (photo)electrochemical stability of α-$SnWO_4$ films. Detailed investigation of the pH and potential dependence is performed. Inductively coupled plasma - optical emission spectroscopy (ICP-OES), X-ray photoelectron spectroscopy (XPS) and X-ray diffraction (XRD) are used for the analysis. A stability window can be defined in neutral to acidic conditions. In-situ spectro(photo)electrochemistry measurements provide further insight into the stability. Comparison of the experimental data with a theoretical Pourbaix diagram is performed. Finally, long-term stability investigation of α-$SnWO_4$ films reveals the self-passivation mechanism, which inhibits further film dissolution.

2. Experimental methods and procedure

2.1. Pulsed laser deposition

Pulsed laser deposition (PLD) is a physical vapor deposition technique, in which the target-to-substrate transfer of the material is achieved with a laser. The laser is operated in a pulsed fashion and with an arrangement of lenses and mirrors the laser beam (e.g. Nd:YAG or KrF excimer laser) is directed into the deposition chamber. In the chamber the laser it is focused on the target as illustrated in Figure 2.1. The deposition chamber is kept under vacuum conditions. Typically the laser has an energy density (i.e., fluence) in the range of 1 to 5 J cm^{-2}.[133] Particularly important is the formation of the so-called plume (i.e., the vaporized material). The underlying physical principles are complex.[134] Described in a simplified way according to the comprehensive overviews by Eason[135] as well as Lowndes et al.,[133] the plume formation occurs as follows: the laser beam impinges on the target and rapidly heats up the surface resulting in the instant (~0.1 µs) ablation or vaporization of the material in non-equilibrium conditions. The laser beam only heats up a small fraction of the material, while the energy input is well above the threshold for evaporation. As a result, a partially ionized plume is formed. The wavelength of the laser is typically in the UV range and the pulse width is in the range of 0.1 – 20 ns. The stoichiometry of the transferred material does not depend on the vapor pressure of the respective elements, which is a fundamental difference to evaporation-based techniques. Subsequently, the plasma plume traverses to the substrate and impinges on the surface and film growth occurs. The whole process from ablation to film growth occurs within ~4 µs. Substrates are typically placed within a distance of 5 – 10 cm away from the target.[133, 135]

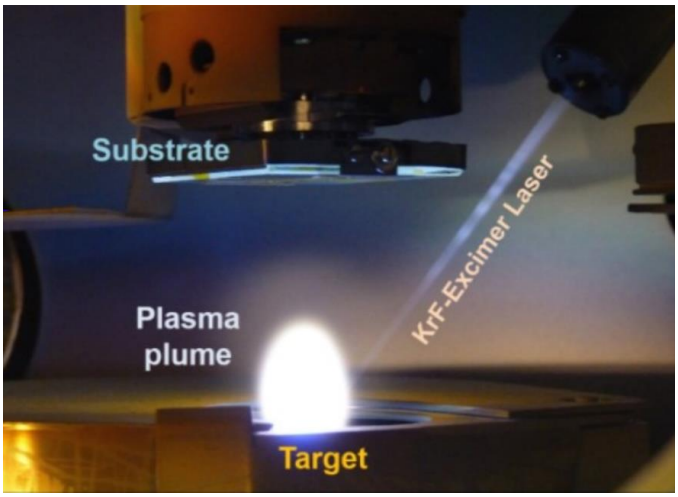

Figure 2.1. Illustration of the pulsed laser deposition (PLD) process. A UV laser (KrF-Excimer) is focused on the surface of a target in the vacuum deposition chamber, which is followed by the creation of the plasma plume. The vaporized material is transferred to the substrate where film growth occurs. Adapted from reference [118].

Several characteristics make the PLD process attractive for thin film deposition. The stoichiometric target-to-substrate transfer mentioned above is typically considered as one of the main advantages. In practice, however, this can be more complex and additional factors need to be considered.[136] Conceptual simplicity of the PLD experiment and applicability of a wide range of materials in the form of high purity targets are further advantages of PLD. During deposition background gases can be used for reactive processes, which broadens the flexibility for tuning the film properties. A kinetic energy excess of the species arriving at the substrate can be beneficial for the growth process, and for achieving high density films. The highly directed nature of the plasma plume can be partially considered as a demerit. However, homogeneous film thicknesses can still be achieved by a combination of target rotation and target raster scanning with the laser. The line-of-sight nature of the deposition process, however, makes PLD unsuitable for coating of nanostructured substrates. Finally, the alternating deposition from several targets is possible as well, when the PLD system is equipped with a target carousel. Such an approach can provide further flexibility in tuning the film composition and properties.[137-139]

A significant amount of studies has been performed with the PLD technique over the last decades. Earlier works reach back to the year 1965,[140] but the interest and number of reports was limited in the initial phase of PLD development.[141] Commonly the report by Dijkamp and co-workers, in which the first successful stoichiometric deposition of the superconductor $YBa_2Cu_3O_{7-x}$ (YBCO) was demonstrated, is considered as an important milestone in the development of PLD processes.[142-143] The accelerated interest in PLD processes in the years afterward, resulted in a significant increase in the number of publications.[141]

PLD has been used to deposit a variety of metal oxide semiconductors for water splitting, among which are TiO_2,[144] α-Fe_2O_3,[145-146] $BiVO_4$,[57, 137, 147] and several other photoelectrode materials.[90, 148-149] Beyond the preparation of polycrystalline films, PLD has been applied successfully for epitaxial layer deposition.[98, 150-151] Epitaxial films are useful, for instance, to study orientation dependent film properties such as the photoelectrochemical performance.[152]

2.1.1. Deposition of α-$SnWO_4$ thin films

α-$SnWO_4$ thin film photoelectrodes were deposited by PLD based on the process reported by Kölbach et al.[90] Glass substrates coated with fluorine-doped SnO_2 as transparent conducting layer (FTO) were used. These substrates were cut to a size of ~24 x 24 mm^2 and subjected to a cleaning procedure before film deposition. In an ultrasonic bath they were successively cleaned

in acetone, isopropanol, ethanol, and deionized water (Milli-Q) for 15 min each. An N_2 gas stream was used to dry the substrates afterwards.

A custom-built PLD setup from PREVAC (Poland) was used, which was equipped with a KrF excimer laser (LPXpro 210, Coherent) with a wavelength λ = 248 nm. The base pressure in the deposition chamber was ~10^{-7}mbar. Films were deposited at room temperature from a ceramic α-$SnWO_4$ target with a laser repetition rate of 10 Hz. The substrate-to-target distance was set to d = 60 mm and the laser fluence was adjusted to F = 2 J cm^{-2}. Deposition was performed with an O_2 background pressure of ~1 x 10^{-4} mbar. By adjusting the number of laser shots, the desired film thickness was achieved. Film crystallization in the orthorhombic α-phase was achieved by post-deposition annealing in a tube-furnace in Ar atmosphere at 520°C. Before annealing the tube was evacuated and flushed two times to keep the O_2 content during annealing as low as possible.

The target was prepared by mixing stoichiometric amounts of WO_3 (99.998 % purity, Alfa Aesar) and SnO powder (99.99 % purity, Sigma-Aldrich). Powders were mixed with a ball mill and subsequently pressed in the form of a pellet. Annealing at 740°C in Ar atmosphere was used to achieve the solid-state reaction. Presence of the α-phase of the target was confirmed by X-ray diffraction.

2.1.2. Deposition of NiO_x overlayers

NiO_x overlayers were deposited by a reactive PLD process as reported in the literature.[90] The same system described in the previous section was used for deposition. A metallic Ni target (99.99 %, Alfa Aesar) was ablated with F = 2 J cm^{-2} and a laser repetition rate of 10 Hz. During deposition the substrate was kept at room temperature and the O_2 background pressure during deposition was 5 x 10^{-2} mbar. Between substrate and target a distance of d = 60 mm was set. The number of laser shots was adjusted to achieve the desired layer thickness.

2.2. X-ray diffraction

In Chapter 3 and 4 characterization of the crystalline phase was performed with a Bruker D8 Advance diffractometer, in which a grazing incidence configuration was used. The X-ray beam strikes the sample surface with a grazing angle of 0.5°, thereby enhancing the signal contribution from the film compared to that of the substrate. The system is equipped with an X-ray tube emitting Cu Kα radiation with a wavelength λ = 1.5406 Å. The tube was operated with an acceleration voltage of 40 kV and a current of 40 mA. X-ray diffractograms were recorded with a step size of 0.02°, while each step was measured for 6 s.

XRD characterization in Chapter 5 was performed with a PANalytical X'Pert Pro multipurpose diffractometer operated with an acceleration voltage of 40 kV and a current of 40 mA. The setup provides the ability to adjust the spot size of the X-ray beam on the sample. In the present study, this was adjusted to 6 × 6 mm^2 to probe only the area that was exposed to the photoelectrochemical treatment. The step size was 0.04° and during each step the signal was counted for 8 s.

2.3. Photoelectron Spectroscopy

Photoelectron or photoemission spectroscopy (PES) was extensively used in this study and, therefore, a few important features are briefly summarized here. PES is a widely used technique to study the chemical and electronic surface properties. The surface sensitivity, being to some degree tunable, is thereby an important feature of this technique. This feature originates from the underlying physical principle. When photons with an kinetic energy exceeding the ionization potential strike the surface of the material to be analyzed, photoelectrons are emitted according the external photoelectric effect.[153] In Figure 2.2 the principle is schematically illustrated. Electrical contact between sample and analyzer results in alignment of the Fermi levels and, consequently, the work function of the sample is not relevant. After being emitted from the sample a photoelectron has the kinetic energy E_{kin} as described in the following equation:

$$E_{\mathrm{kin}} = \mathrm{h}\nu - E_{\mathrm{bind}} - \varphi_{\mathrm{spec}} \tag{2.1}$$

E_{kin} depends on the photon energy hν, the binding energy E_{bind} of the energetic level from which the photoelectron is excited, and the work function of the spectrometer φ_{spec}.[154-155]

The surface spectroscopic information of the photoelectrons is revealed during analysis of the photoelectron energies, which are measured in a hemispherical analyzer. The analyzer consists of an outer and inner hemisphere at which negative and positive electric potentials are applied. In the fixed analyzer transmission mode, the pass energy which defines the mean radius is kept constant. In every photoemission spectroscopy experiment, the pass energy is an important metric, which influences the energy resolution of the measurement. The above-mentioned surface sensitivity is a consequence of the dependence of the inelastic mean free path (IMFP) λ_{IMPF} of the photoelectron on its energy. A reduction of the surface sensitivity, to study for instance buried interfaces, can be achieved by an increase of the photon energy; this will increase the energy of the excited photoelectron and, therefore, its IMFP. According to the energy range of the photon source, photoemission spectroscopy can be classified as ultraviolet photoelectron spectroscopy (UPS), X-ray photoelectron spectroscopy (XPS) and hard X-ray

photoelectron spectroscopy (HAXPES), where UPS has the highest surface sensitivity and HAXPES has the lowest surface sensitivity.

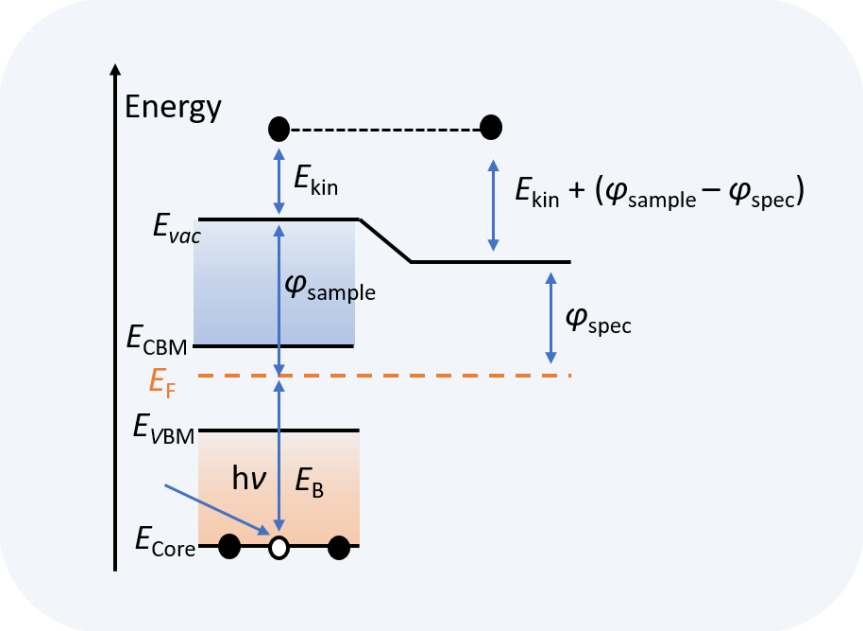

Figure 2.2. Principle of photoelectron spectroscopy illustrated on a simplified band diagram. A photon with kinetic energy hν strikes the surface of a sample, and excites a photoelectron above the vacuum level energy E_{vac} according to the external photoelectric effect. The energy dependent analysis of the photoelectrons provides chemical and electronic information of the sample. E_{core} denotes the energy level of a core level, E_B the binding energy, φ_{sample} the work function of the sample, φ_{spec} the work function of the spectrometer, E_{kin} the kinetic energy of the photoelectron, E_{VBM} the valence band maximum energy and E_{CBM} the energy level of the conduction band minimum.

2.3.1. Lab-based X-ray photoelectron spectroscopy

Lab-based X-ray photoelectron spectroscopy was performed with a Al Kα X-ray source, which provides an excitation energy of λ = 1486.74 eV. The setup is equipped with a SPECS Focus 500 monochromator and a SPECS Phoibos 100 hemispherical analyzer. The beam spot size on the sample was 1 mm x 3.5 mm. In the analysis chamber the base pressure was ~10^{-9} mbar. Core level spectra were recorded with a step size 0.05 eV and a pass energy of 10 eV. Quantitative analysis was performed by a peak fitting procedure. Prior to analysis of the core level spectra, a Shirley baseline subtraction was performed. Pseudo Voigt functions were used to model the peak shape. These functions are defined by a convolution of gaussian and Lorentzian functions. Further parameters included in the fitting model are the FWHM of the peaks, peak intensity ratios, and binding energy differences between different oxidation states. Beginning with the starting parameters of the fitting model, chi-square optimization was performed to optimize the fitting results. In order to estimate the relative contribution C_A of an oxidation state A, de-convoluted from a peak with oxidation states A and B, the following formula 2.2 was used.

$$C_A = \frac{X_A}{X_B + X_A} \quad (2.2)$$

Here, X_A and X_B are the integrated areas of the peaks corresponding to the states A and B (for instance, Sn^{2+} and Sn^{4+} in the present study).

2.3.2. Hard X-ray photoelectron spectroscopy at BESSY II

PES using higher Photon energies was applied in the present study in Chapter 3 and 4. HAXPES measurements were performed at the BESSY II synchrotron facility at Helmholtz-Zentrum Berlin, Germany. Here, the tunable X-ray source was the high kinetic energy photoemission end station (HIKE)[156] at the KMC-1 beamline.[157] Photon energies in the range of 2 to 12 keV are available. In the present study photon energies of 2003 eV, 4000 eV and 6009 eV were used, which are abbreviated as 2, 4 and 6 keV in the remaining part of this thesis. The energies were selected with the help of a Si (111) and Si (311) double crystal monochromator. Emitted photoelectrons were detected with a Scienta R4000 analyzer. The analysis chamber had a base pressure of ~10^{-8} mbar. Core level and valence band spectra were recorded with a step size of 0.05 eV in Chapter 3 and 0.1 eV in Chapter 4. The pass energy was set to 200 eV. The number of scans (i.e., the measurement duration) measured in the different core level regions was adjusted flexibly according to the respective signal intensity, to obtain a reasonably good signal-to-noise-ratio, while excluding unreasonably long measurement times. The binding energies were referenced to the Au 4f core level at 84.0 eV. This was measured before and after the sample measurement on a piece of Au foil mounted in the analysis chamber, where the sample and Au foil shared a common ground. Quantitative analysis was performed as described in the previous section.

2.3.3. Resonant photoelectron spectroscopy at BESSY II

In Chapter 4 resonant photoemission spectroscopy (ResPES) was performed at the HIKE[156] end station at the KMC-1 beamline[157] at BESSY II. First, the absorption edges of W and Sn were measured using X-ray absorption spectroscopy (XAS). A Bruker XFlash 4010 fluorescence detector was used to detect the signal. The minimum accessible photon energy is 2000 eV and, therefore, the W M-edge was recorded with the Si (111) double crystal monochromator. The Sn L-edge was recorded with the Si (111) and Si (311) double crystal monochromators. Subsequently, HAXPES was used to measure valence band spectra with excitation energies corresponding to features in the absorption spectra, i.e., the measurement was performed under resonant conditions. The valence band spectra were recorded with a step size of 0.1 eV and a pass energy of 200 eV. As described in the previous section, the binding energies were

referenced to the Au 4f core level at 84.0 eV, measured on a piece of Au foil for all different excitation energies.

2.4. Photoelectrochemical measurements

A three-electrode configuration was used as the standard setup for photoelectrochemical (PEC) measurements. The used custom-made Teflon cell is schematically depicted in Figure 2.3. The cell has a transparent quartz window for sample illumination. As reference electrode an Ag/AgCl electrode (XR300, KCl saturated, Radiometer Analytics) was used and a platinum wire was used as the counter electrode of the measurement. Electrical contacting of the sample (i.e., the working electrode) was achieved by gluing a wire to the underlying transparent conducting oxide. The illuminated area of the sample is given by a circular area with a diameter of d_{WE}. AM1.5 solar radiation was simulated with a WACOM super solar simulator (Model WXS-505-5h, AM1.5, Class AAA). An EG&G Princeton Applied Research (Model 273A) potentiostat was used for the measurements. Potentials were converted to the reversible hydrogen electrode (RHE) scale by applying the Nernst equation (equation 2.3). V_{app} is the applied potential, $V_{Ag/AgCl}$ is the potential measured at the reference electrode and standard potential $E°_{Ag/AgCl}$ = 0.199 V.[126]

$$V_{\mathrm{app}} = V_{\mathrm{Ag/AgCl}} + 0.059\mathrm{pH} + E^{\circ}_{\mathrm{Ag/AgCl}} \tag{2.3}$$

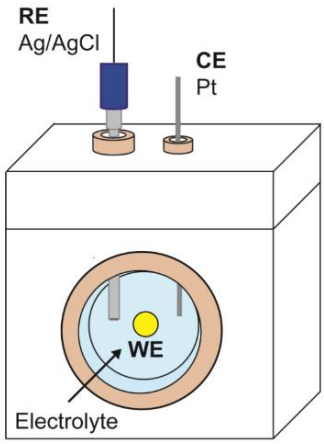

Figure 2.3. Schematic illustration of the three-electrode setup for photoelectrochemical measurements, including the working electrode (WE), the reference electrode (RE) and the counter electrode (CE). Adapted from reference [158].

α-$SnWO_4$ films were typically measured in a 0.5 M potassium phosphate buffer (KP_i) at pH ~7, which changes to ~7.2 after addition of 0.5 M Na_2SO_3 as a hole scavenger. The buffer was made from KH_2PO_4 (≥ 99.0 %, Sigma-Aldrich) and $K_2HPO_4 \times 3\ H_2O$ (≥ 99.0 %, Sigma-Aldrich). Unless otherwise stated, the diameter of the illuminated area was d_{WE} = 6 mm, resulting in an illumination area of 0.28 cm^2. Open circuit potential (OCP) measurements in Chapter 3 were performed in 0.5 M KP_i with 0.5 M Na_2SO_3 at pH ~7.2.

In Chapter 4 the SnO_2 layer on the surface of α-$SnWO_4$ was introduced by photoelectrochemical oxidation. The illuminated area had a diameter of d_{WE} = 10 mm. A potential of 1.23 V vs. RHE was applied for different durations to achieve different thicknesses of the oxidized layer. The electrolyte was 0.5 M KP_i with 0.5 M Na_2SO_3 at pH ~7.2.

In Chapter 5 PEC measurements for the stability investigation of α-$SnWO_4$ films were performed in various electrolytes with different pH values. For pH 2 a 0.1 M HCl/KCl buffer was used, which was made from 1 M HCl (PanReac AppliChem ITW Reagents) and KCl (Bernd Kraft). Measurements in pH 5, 7, and 9 were performed in KP_i. For pH 13, 0.1 M KOH (Karl Roth GmbH) was used.

2.5. Spectro(photo)electrochemistry

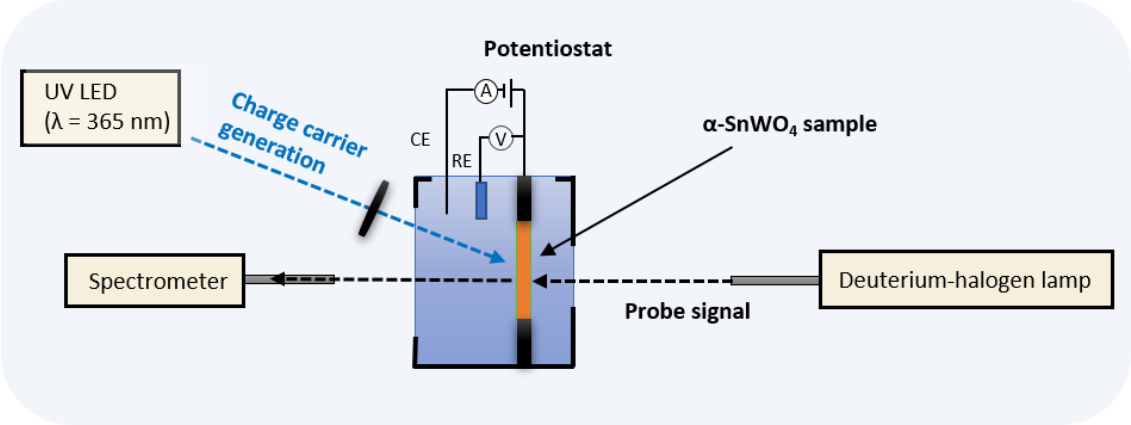

Figure 2.4. Schematic illustration of the spectro(photo)electrochemistry setup used for the stability study of α-$SnWO_4$ in Chapter 5. The sample is mounted in a PEC cell that is filled with the respective electrolyte. Charge carriers are generated with a UV-LED. A deuterium-halogen light source and a USB spectrometer are used to probe the change in transmission to investigate the stability. The light is guided through solarization-resistant optical fiber/collimator assemblies.

In Chapter 5 the stability of α-$SnWO_4$ films was also investigated by spectro(photo)-electrochemistry. Here, a PEC measurement is combined with the in-situ measurement of the optical transmission. From the change in the transmission of the α-$SnWO_4$ films, information about their stability can be obtained. A schematic illustration of the setup is shown in Figure 2.4. The sample is placed in a PEC cell, and the potential was applied in a three-electrode configuration with an EG&G Princeton Applied Research (Model 273A) potentiostat. A platinum wire and an Ag/AgCl electrode (XR300, KCl saturated, Radiometer Analytics) were used as counter and reference electrodes, respectively. Charge carriers were generated by irradiation with a UV-LED (λ = 365 nm, Thorlabs). The change in transmission was measured with a white light source (Deuterium-Halogen lamp, DH-2000-BAL, Ocean Optics) combined with a USB spectrometer (2000-Pro, Ocean Optics). Solarization-resistant optical fiber/collimator

assemblies were used to guide the signal from the white lamp to the sample and from the sample to the spectrometer.

The spectrometer input signal can be switched between the light transmitted through the sample and white light source itself. To confirm that the recorded change in transmission was not significantly influenced by slow fluctuations of the white light source, the input signal was switched several times to the lamp intensity during each measurement. A MATLAB script was finally used for data processing, in which the control datapoints for the recorded source intensity measurements were removed. The change in optical density ΔOD was plotted and calculated by the following equation:

$$\Delta \mathrm{OD} = -\log\left(\frac{T}{T_{\mathrm{ref}}}\right) \tag{2.4}$$

Here, T_l is the transmitted signal intensity and T_{ref} the reference signal, which is the transmitted signal intensity before the start of the PEC measurement.

2.6. Inductively coupled plasma - optical emission spectroscopy

Inductively coupled plasma - optical emission spectroscopy (ICP - OES) is a widely used analytical tool to quantify the presence of elemental traces in a sample. In brief, the technique works as follows: liquid samples are typically introduced into the system and vaporized by a plasma with temperatures up to 10,000°C.[159] The atomic excitation and subsequent emission of photons with characteristic wavelength during decay processes can be used to detect the elemental concentrations. This is achieved in combination with a spectrometer and detector.[159]

In order to study the stability of α-$SnWO_4$ films, ICP-OES was used in Chapter 5. The used experimental setup was a Thermo iCAP 7400 system (Thermo Fischer Scientific), which was operated in the axial mode. An auxiliary Ar gas flow of 0.5 l/min was used and the exposure time during the measurement was set to 10 s. After PEC measurements on the α-$SnWO_4$ films under various conditions, the electrolyte was measured by ICP-OES to detect the presence of corrosion products (i.e., Sn, W, Ni). In each measurement sequence a reference sample of the respective electrolyte was measured, i.e., the fresh electrolyte without corrosion products. For calibration, standard solutions were prepared with four to five different concentrations covering the measurement range. The initial concentration of the commercial ICP-OES standards was 1000 g/l and had to be diluted in the respective matrix of the standard solution. A 10 % HCl matrix (Roti Star, Carl Roth GmbH; 99.99 % purity) was used for the Sn standard and a 4 % NH_3 matrix (Roti Star, Carl Roth GmbH; 99.99 % purity) for the W standard. For Ni a commercial multi-element standard was used, which had a 6.5 % HNO_3 matrix.

2.7. Modulated surface photovoltage analysis

Several electronic properties such as transport mechanisms, charge carrier trapping, or electronic states can be investigated by surface photovoltage (SPV) measurements. SPV analysis has been used in several studies related to metal oxide semiconductors for PEC.[160-161] First reports on SPV reach back to Brattain in the year 1947.[162-163]

As the name suggests, an SPV signal originates from the change of surface potential due to the generation of charge carriers upon illumination.[164-165] An essential feature for the occurrence of a SPV signal is, therefore, the spatial redistribution of charge carriers after their generation. The charge carrier generation results in a change of the contact potential (difference in work function) between the sample and a reference electrode, *ΔCPD*. A SPV signal is then defined as follows:

$$\mathrm{SPV} = -\Delta CPD \tag{2.5}$$

Typical setups are based on a Kelvin probe or a fixed capacitor configuration. The fixed capacitor arrangement provides higher sensitivity and is schematically illustrated in Figure 2.5.[166] Between the sample electrode and the reference electrode (e.g. FTO layer deposited on SiO_2 cylinder) a fixed distance *d* is set, which explains the name of this configuration. In between an insulator (mica sheet) is placed such that a measurement capacitor C_m is formed. The voltage across this capacitor is measured with a high impedance buffer as illustrated on the right side in Figure 2.5.

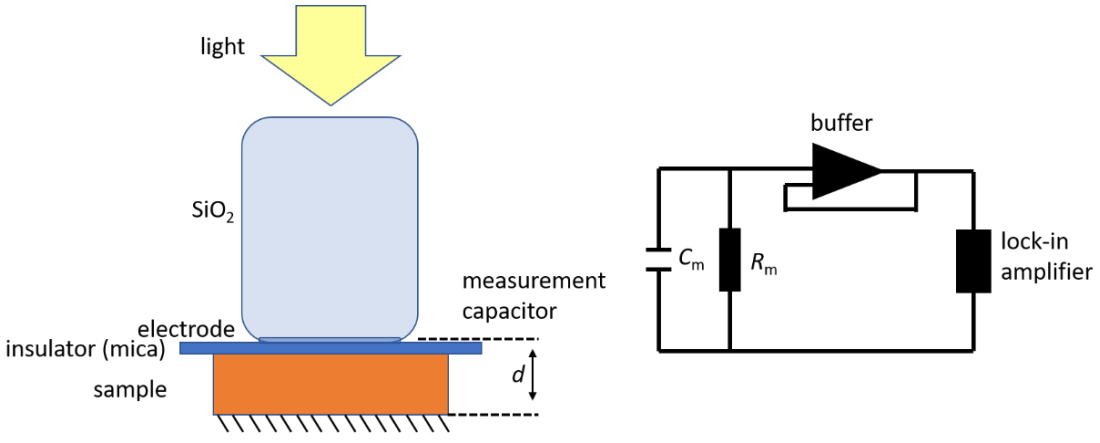

Figure 2.5. (left) Illustration of a typical SPV measurement setup with a fixed capacitor configuration. The distance *d* between the reference electrode and the sample electrode is fixed, and thereby a measurement capacitor is formed. (right) Equivalent circuit of the setup including the measurement capacitor C_m, measurement resistance R_m, high impedance buffer, and dual phase lock in amplifier for signal recording. The illustrations are based on the review by Chen et al.[165]

Using a double phase lock-in amplifier, the in-phase signal *X* and the *Y* signal shifted by 90° can then be recorded, which are defined as follows.[166]

$$X = \int SPV(t) \cdot \sin(2\pi \cdot f_{\mathrm{mod}} \cdot t)dt \tag{2.6}$$

$$Y = \int SPV(t) \cdot \cos(2\pi \cdot f_{\mathrm{mod}} \cdot t)dt \tag{2.7}$$

The purpose of this technique is to obtain information about fast and slow processes that contribute to the SPV signal. Therefore, *X* and *Y* are also called the fast and slow response of the signal, respectively. Important to note is that these signals are related to the modulation frequency of the light source f_{mod} as seen equations 2.6 and 2.7. The 90° phase shift corresponds to $T_{mod}/4$, where T_{mod} is the modulation period and $T_{mod} = 1/f_{mod}$.[166] In the fast response signal, the dominating contribution is typically given by free charge carriers, and the slow response is often dominated by trapped charge carriers. The sign of the fast and slow responses can also give information about the preferential direction of the redistributed charge carriers. A positive *X* and a negative *Y* signal are related to preferential movement of electrons to the back electrode of sample (e.g. the FTO substrate). Other scenarios are in general possible as well. The *X* and *Y* signals, for instance, can also both be positive, indicating an opposite direction of charge carriers that contribute to the fast and slow response.[166]

Another representation of the *X* and *Y* signals can be defined via the photovoltage amplitude R and the phase angle φ, as defined in equation 2.8 and 2.9.[166] In this representation, it is the phase angle that provides information about the preferential direction of the redistributed charge carriers. Finally it is noted that an SPV signal can not only originate from band transitions dominating above the band gap energy, but also from transitions from surface or bulk defect states to conduction band states.[164]

$$R = \sqrt{X^2 + Y^2} \tag{2.8}$$

$$\varphi = \frac{180^\circ}{\pi} arctan \frac{Y}{X} \tag{2.9}$$

In Chapter 4 SPV analysis was used to study α-$SnWO_4$ and α-$SnWO_4$/NiO_x samples. A halogen lamp was used as the light source and modulated with a frequency of f_{mod} = 8 Hz. The measurements were performed on a sample area of 0.5 mm^2.

2.8. Transmission electron microscopy

In Chapter 3 transmission electron microscopy (TEM) was performed with a Philips CM12/STEM. In the setup a LaB_6 cathode is used, and high resolution can be obtained with a super twin lens. The acceleration voltage, used to record the transmission electron micrographs, was 120 keV. Sample preparation was performed with several polishing steps. When a thickness of 4 - 6 µm was achieved, a Mo ring was attached to the sample. Finally, the thickness of the sample was further reduced, using an Ar ion mill, to obtain electron transparency.

3. Interfacial oxide formation limits the photovoltage in α-$SnWO_4$/NiO_x photoanodes prepared by pulsed laser deposition

Parts of this chapter are included in the following publication:

Patrick Schnell, Moritz Kölbach, Markus Schleuning, Keisuke Obata, Rowshanak Irani, Ibbi Y. Ahmet, Moussab Harb, David E. Starr, Roel van de Krol and Fatwa F. Abdi

Advanced Energy Materials 11, **2021,** 2003183 (DOI: 10.1002/aenm.202003183)

3.1. Introduction

α-$SnWO_4$ is an n-type semiconductor with promising properties for photoelectrochemical water splitting. Among these properties is the band gap of 1.9 eV[90] as well as the flat band potential of ~0 V vs. RHE.[113-114, 116] Using AM1.5 solar radiation, a theoretical maximum photocurrent of ~17 mA cm^{-2} is predicted, which is significantly higher than that of the well-known $BiVO_4$ (theoretical maximum photocurrent of ~7.5 mA cm^2).[50-51, 167] Until recently, however, the reported photocurrents for α-$SnWO_4$ films were very low (< 0.1 mA cm^{-2}),[110, 113-114, 116] which is often correlated with fast oxidation of Sn^{2+} to Sn^{4+} at the surface of α-$SnWO_4$. In 2018 Kölbach et al. reported significant improvement in the PEC performance of PLD-made α-$SnWO_4$ films by deposition of a 20 nm NiO_x overlayer by PLD.[90] A photocurrent density of 0.75 mA cm^2 measured in pH 7 electrolyte (0.5 M KP_i + 0.5 M Na_2SO_3 added as a hole scavenger) was reported, which is the highest demonstrated photocurrent density for α-$SnWO_4$ photoanodes up to now. Despite this improvement in photocurrent, the photovoltage in α-$SnWO_4$/NiO_x films was found to be limited, as observed by a relatively high onset potential in cyclic voltammetry. Fermi level pinning at the interface of α-$SnWO_4$ and NiO_x was suggested to be the origin of this limitation. A detailed investigation of this hypothesis, however, has not been reported thus far. Gaining knowledge about this limitation is, therefore, of great importance for the further development of α-$SnWO_4$ photoanodes. Then suitable concepts for improvement can be developed, with the ultimate goal of achieving significantly higher photocurrent densities along with a low photocurrent onset potential. A more detailed review of the properties and progress of α-$SnWO_4$ films is provided in Chapter 1.4.1.

In the present chapter, a detailed investigation of the α-$SnWO_4$/NiO_x is presented to understand the interface issue described above. The photovoltage limitation is verified using open circuit potential analysis and correlated with the NiO_x layer thickness. Hard X-ray photoelectron spectroscopy (HAXPES) was performed at the BESSY II synchrotron facility at Helmholtz-Zentrum Berlin. The obtained data are interpreted with respect to the change of surface

oxidation states and band bending upon deposition of NiO_x overlayers with varying thickness. The discussion of the data with respect to the photovoltage limitation is supported by Density functional theory (DFT) calculations, Monte Carlo-based photoemission spectra simulation, and PEC control experiments. Based on this thorough discussion, an explanation for the origin of the photovoltage limitation in α-$SnWO_4$/NiO_x photoanodes is proposed.

3.2. Verification of the photovoltage limitation in α-$SnWO_4$/NiO_x photoanodes

First, the α-$SnWO_4$/NiO_x interface limitation is investigated using a PEC method. Here, measurement of the ΔOCP, i.e., the difference in open circuit potential between illumination and dark, is used as an (approximate) measure to determine the photovoltage. For these measurements, α-$SnWO_4$ films with a thickness of ~100 nm were deposited by PLD. XRD was used to verify the phase purity of the films after crystallization. A representative X-ray diffractogram is shown in Figure A1. Samples were then coated with varying thickness of PLD-deposited NiO_x (see Chapter 2.1. for procedure). On all samples the ΔOCP was measured in a pH 7.2 electrolyte with 0.5 M KP_i + 0.5 M Na_2SO_3 added as a hole scavenger. In Figure 3.1 the obtained data are depicted, where a clear decrease of the ΔOCP can be observed starting from the pristine α-$SnWO_4$ film, which saturates for NiO_x layer thicknesses larger than 10 nm. The observation of a reduced ΔOCP with NiO_x deposition agrees well with the observations made by Kölbach et al.[90]

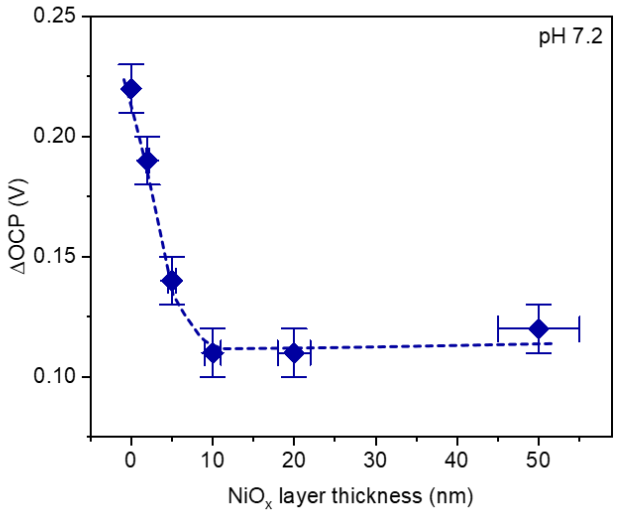

Figure 3.1. Open circuit potential analysis (ΔOCP; difference between light and AM1.5 illumination) of α-$SnWO_4$ films coated with different thicknesses of PLD NiO_x in comparison to the pristine film (0 nm NiO_x) The electrolyte was 0.5 M KP_i with 0.5 M Na_2SO_3 added as a hole scavenger at pH ~7.2. The ΔOCP decreases with an increasing NiO_x layer thickness and saturates at a value of ~0.1 V for NiO_x thicknesses larger than 10 nm, indicating that the deposition of NiO_x introduces a limitation of the photovoltage. The error of the NiO_x layer thickness is based on the deposition rate calibration and was estimated to be 10 %.

The extended analysis in the present study gives additional insight and reveals that the magnitude of photovoltage reduction depends on the NiO_x layer thickness (in the previous analysis the NiO_x thickness was limited to 20 nm). In general, a limited photovoltage can be related to the presence of intra-band states as reported for other metal oxide semiconductors.[168-169] A possible origin for such states may be found in the preparation procedure of the α-$SnWO_4$/NiO_x samples in the present study. After deposition in the PLD chamber, the $SnWO_4$ films are transferred to a tube furnace, while the samples are exposed to air, and afterwards transferred back to the PLD chamber for NiO_x deposition. The air exposure may lead to the formation of hydroxide or oxyhydroxide species at the surface. Consequently, intra-band states may be introduced.[168-169] This could be ruled out, however, by the development of an alternative preparation procedure, where air exposure is prevented by performing all preparation steps in the PLD chamber. In Figure 3.2a the LSV (linear sweep voltammetry) scans of samples prepared with both procedures are compared, and despite the variation of the dark current, a clear difference in the high onset potential cannot be observed. The photocurrent densities presented in (b) also do not show a clear difference, and the values are in general agreement with the earlier report in literature.[90]

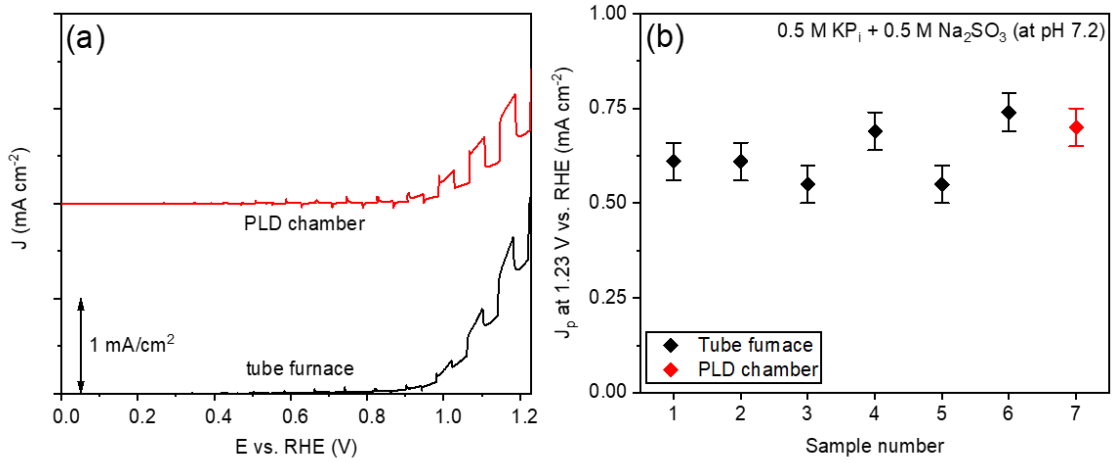

Figure 3.2. Comparison of the two preparation procedures for α-$SnWO_4$ films coated with 20 nm NiO_x. After room temperature deposition in the PLD chamber samples are either transferred to a tube furnace for crystallization (while breaking the vacuum during transfer) or annealing is performed in the PLD chamber (without breaking vacuum). Afterwards NiO_x deposition was performed. In (a) LSV (linear sweep voltammetry) curves are shown for two representative samples, where a clear difference cannot be observed, despite variation in the dark current. The photocurrent densities for both types of samples are similar as shown in (b).

3.3. Investigation of the α-$SnWO_4$/NiO_x interface by hard X-ray photoelectron spectroscopy

In order to obtain detailed understanding of the α-$SnWO_4$/NiO_x interface, and to interpret the ΔOCP analysis in the previous section, HAXPES measurements were performed at the BESSY II synchrotron facility. As in the case of the ΔOCP measurements, α-$SnWO_4$ films were coated with NiO_x films of varying thickness, as schematically described in Figure 3.3. In addition to the variation of the NiO_x thickness, the information depth is varied by changing the kinetic photon energy (between 2 - 6 keV). This is an eminent capability of synchrotron-based photoemission experiments. The mean free path λ_{IMPF} of the emitted photoelectrons and, therefore, the probing depth σ in the material ($\sigma = 3\,\lambda_{IMPF}$) depends on the kinetic energy of incident photons, as defined in Chapter 2.3 in equation 2.1.

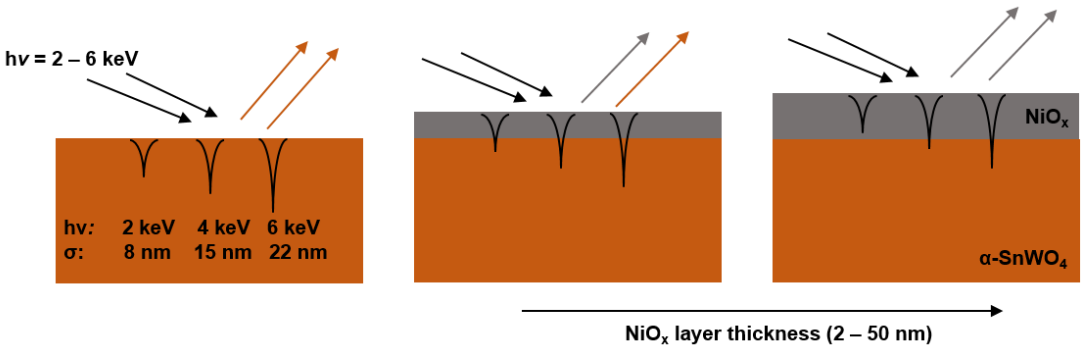

Figure 3.3. Hard X-ray photoelectron spectroscopy study of the α-$SnWO_4$/NiO_x interface performed at the BESSY II synchrotron facility at HZB. The experimental procedure of the interface experiment is schematically depicted. α-$SnWO_4$ films with a thickness of 100 nm are coated with PLD-deposited NiO_x with varying thickness in the range of 2 to 50 nm, and are compared with a pristine α-$SnWO_4$ film. Signal arising from α-$SnWO_4$ is attenuated with an increasing NiO_x thickness, as indicated by the orange (α-$SnWO_4$) and grey (NiO_x) arrows. As indicated in the figure, the probing depth σ (equivalent to three times the mean free path λ_{IMPF}) increases with an increasing photon energy hν, which can be used to resolve interfacial features.

In principle, interfacial features can thereby be de-convoluted from features related to the surface or bulk of the probed material stack. First of all, pristine α-$SnWO_4$ films were investigated by HAXPES to set the baseline for the evaluation of the chemical sates at the interface. In Figure 3.4 the W 4f and Sn 3d core levels are depicted, which were measured with hν = 2 keV. Using a peak fitting procedure (see Chapter 2.3. for details), the W 4f core level can be de-convoluted in a W^{6+} contribution and a W^{5+} contribution. W^{6+} is the nominal oxidation state in α-$SnWO_4$ and, therefore, the high contribution is expected. The small contribution of W^{5+} is not related to beam damage, which was confirmed by a beam damage study using several beam filters, while measuring at different spots on the sample. An impact of the beam intensity

and measurement spot on the relative contribution of W^{5+} was not observed (see Figure S2 for the spectra and analysis). A contribution of W^{5+} could also be observed by lab-based X-ray photoelectron spectroscopy (XPS), which was not the case in a previous report.[90] However, in both studies the ΔOCP and photocurrent onset potential are very similar, which are the parameters of interest in this study. This confirms that the W^{5+} contribution has no impact on the junction properties in the present study. At this point, it has to be mentioned that the origin of the W^{5+} contribution cannot be fully clarified in the present study, although it may be interesting to study the impact of the W^{5+} contribution on the charge transport properties. Further studies may be conducted in the future to reveal the impact on the bulk properties. In the Sn 3d core level spectrum mainly a Sn^{2+} contribution is present, as expected in α-$SnWO_4$. The peak asymmetry towards higher binding energy indicates the presence of oxidized Sn^{4+}, which has an estimated relative contribution of 18 ± 3 %. Presence of a small Sn^{4+} contribution was expected, and lab-based XPS ($h\nu$ = 1486.74 eV) in a previous study showed a Sn^{4+} contribution of comparable magnitude.[90]

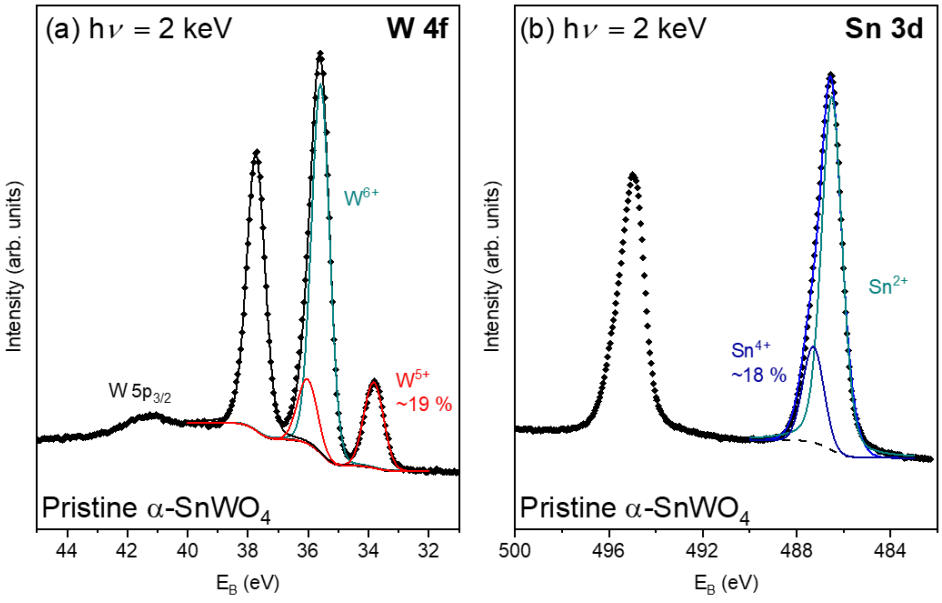

Figure 3.4. Analysis of W 4f (a) and Sn 3d (b) core level spectra measured by HAXPES on a pristine α-$SnWO_4$ film with a photon energy of $h\nu$ = 2 keV. The fitted spectra are included. In addition to the nominal oxidation states in α-$SnWO_4$ (W^{6+} and Sn^{2+}), also contributions of W^{5+} and Sn^{4+} are present. The presence of Sn^{4+} is also seen in the peak asymmetry towards higher binding energy E_B in the Sn 3d core level. The relative contributions of the Sn^{4+} and W^{5+} species are indicated in the figure.

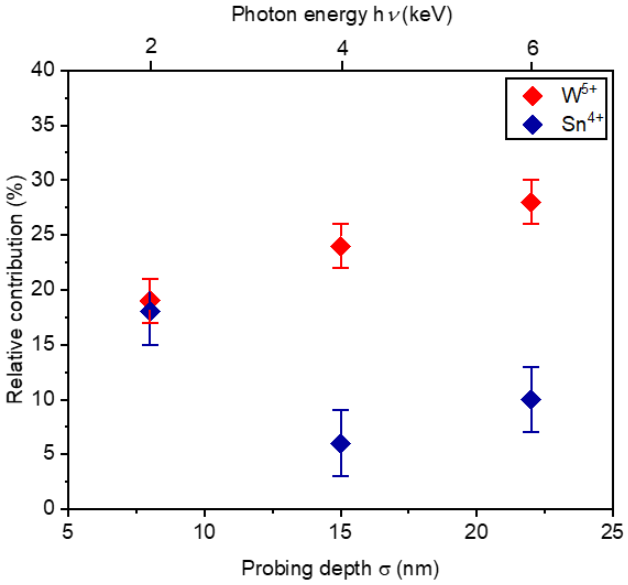

Figure 3.5. Dependence of the relative W^{5+} and Sn^{4+} contributions on the probing depth σ (i.e., photon energy, shown on the top x-axis). The measurements were performed on a pristine α-$SnWO_4$ film, and the contributions were estimated by a peak fitting procedure. The relative W^{5+} contribution increase towards the bulk of the material, whereas the presence of Sn^{4+} is higher at the surface in comparison to the bulk.

Varying the photon energy of the core level measurements of the pristine film reveals an increase of the relative W^{5+} contribution with increasing photon energy hν, as shown in Figure 3.5 (see Figure A3a for the spectra). This observation suggests a higher contribution of W^{5+} in the bulk of the material compared to the surface. The relative Sn^{4+} contribution shows an opposite behavior and tends to decrease with increasing probing depth σ (see Figure A3b for the spectra). This suggests a higher contribution of Sn^{4+} at the surface in comparison to the bulk, and indicates the relevance of the Sn^{4+} contribution for the present study of the α-$SnWO_4$ surface/interface. Under the conditions of the HAXPES experiment, significant band bending at the surface of pristine α-$SnWO_4$ cannot be found, as evidenced by the absence of a binding energy shift with varying photon energies hν as seen in Figure A3. Measurements of the O 1s and valence band spectra of the pristine film can be found in Figure A3c and (d).

In the next step, the influence of the NiO_x layer on the chemical states at the α-$SnWO_4$/NiO_x interface is evaluated. In Figure 3.6a the W 4f core level spectrum of the pristine α-$SnWO_4$ film is compared with the spectra of films coated with NiO_x thicknesses between 2 nm and 50 nm. Here, the measurement was performed with hν = 2 keV. The fitted spectra as well as the spectra measured at different photon energies can be found in Figure A4 - 6. A clear shift of the binding energies to lower values is observed for the W^{6+} peak with increasing NiO_x layer thickness. For illustration of the peak shift a vertical dashed line (cyan color) is added in the graph at the

position corresponding to the W^{6+} peak of the pristine film. In contrast, the binding energy of W^{5+} remains relatively constant as indicated by the dashed vertical line (red color) located at 33.8 eV. For higher photon energies, the W^{5+} peak also position remains relatively constant (see Figure A6). The relative contribution of W^{5+} seems to decrease for larger NiO_x thickness (> 10 nm) more than expected by the attenuation of the NiO_x layer (see Figure 3.6c). It is noted, however, that quantitative evaluation is precluded due to the poor signal-to-noise ratio. Especially for higher photon energies the tendency for a decreasing W^{5+} contribution with increasing NiO_x thickness can be observed, which can be seen more clearly in the inset of Figure 3.6c. For the higher photon energies, the W^{5+} contributions are high enough to be evaluated quantitatively, whereas for 2 keV measurements, this is not possible for the larger NiO_x thicknesses. This finding agrees well with the suggestion above in Figure 3.5 that W^{5+} has a higher contribution in the bulk in comparison to the surface/interface of α-$SnWO_4$.

The Sn 3d core level spectra of the pristine α-$SnWO_4$ film and the NiO_x-coated films are shown in Figure 3.6b. De-convolution into a Sn^{2+} and Sn^{4+} contribution can be achieved by a peak fitting procedure. The peak maxima shift to higher binding energies, which is related to a significant increase of the relative Sn^{4+} contribution (see Figure 3.6d). For NiO_x thicknesses larger than 10 nm, Sn^{4+} becomes the dominant contribution to the total signal for measurements performed with hν = 2 keV. Further increase of the Sn^{4+} contribution is less pronounced and seems to correlate with the saturation of the ΔOCP at thicknesses beyond 10 nm (see Figure 3.1). Measurements performed with higher photon energies (i.e., larger probing depths σ) show the same trend. As observed for the 2 keV measurements, in the measurements with higher photon energies, the strongest increase of the Sn^{4+} contribution is observed up to 10 nm NiO_x. Overall the increase of the Sn^{4+} contribution is smaller for larger probing depths, indicating that the observed oxidation of Sn^{2+} to Sn^{4+} is a phenomenon that mainly occurs at the α-$SnWO_4$/NiO_x interface and, therefore, not in the bulk of the material. A detailed discussion of the Sn^{4+} contribution with respect the interface properties and photovoltage is presented in Chapter 3.4.

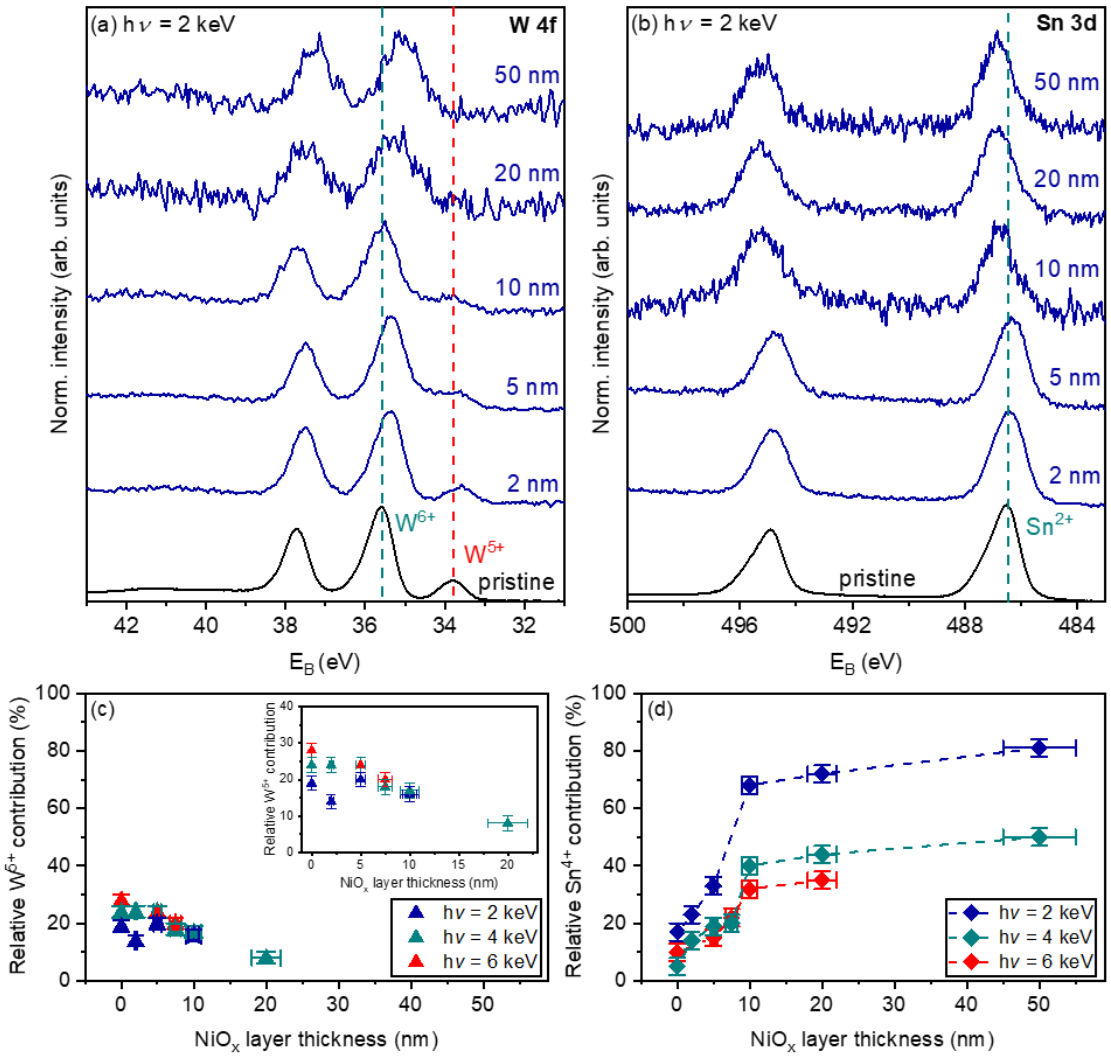

Figure 3.6. (a) and (b) show W 4f and Sn 3d core level spectra of a pristine α-$SnWO_4$ film and spectra of films coated with varying NiO_x thickness. The measurements were performed with a photon energy of 2 keV. The binding energies of W^{5+}, W^{6+} and Sn^{4+} of the pristine film are indicated by the dashed vertical line. (c) Relative W^{5+} contribution as a function of the NiO_x layer thickness measured with different photon energies. A tendency for a decrease in the W^{5+} contribution with increasing NiO_x thickness can be observed, mainly for higher kinetic energies, which can be seen in more detail in the inset. (d) The relative Sn^{4+} contribution increases with increasing NiO_x thickness. This oxidation phenomenon of Sn^{2+} to Sn^{4+} is occurring predominantly at the interface, indicated by the larger increase in the contributions extracted from measurements with lower photon energy (i.e., shorter probing depth). For some of the measured W 4f and Sn 3d spectra, the relative contributions could not be extracted by peak fitting due to the poor signal-to-noise ratio.

The observations in the remaining spectra (Ni 2p, O 1s, and valence band) are less significant for the discussion of the interfacial properties, and are only briefly summarized at this point. The Ni 2p core level spectra were measured for all samples with varying photon energy and are shown in Figure A7. A change in the chemical nature of the NiO_x layer with increasing thickness is not observed due to the absence of significant changes in the Ni 2p core level, as described in more detail in Figure A8. In Figure A7 the O 1s core level spectra are depicted, which were also recorded with different photon energies. As expected, the ratio between peaks arising from oxygen in α-$SnWO_4$ (at higher binding energy) and NiO_x (at lower binding energy) changes with an increasing NiO_x thickness. This is also true for variation of the photon energy, where a change in the oxygen peak ratio is also expected by the variation of the probing depth σ (see Figure A7). For all samples valence band spectra were recorded, which can be found in Figure A9. A convolution of states related to α-$SnWO_4$ and NiO_x can be observed. With increasing NiO_x thickness features corresponding to NiO_x become larger and features of the α-$SnWO_4$ valence band become smaller. A more detailed discussion of valence band spectra of α-$SnWO_4$ is given in Chapter 4.

Finally, it should be noted that there seems to be an inconsistency between the expected probing depths σ and the experimental ability to detect the W 4f and Sn 3d core levels also for larger NiO_x layer thicknesses (see Figure 3.6a and (b) and Figure A6 for higher photon energies). That is, it would be expected for larger NiO_x thickness that the W 4f and Sn 3d core levels are not visible. This notion can be explained by the morphology of the NiO_x layer. As shown previously by scanning electron microscopy, the morphology of the NiO_x layer exhibits an island growth, rather than being flat and dense.[90]

When de-convoluting the core level spectra in their respective contributions, the binding energies can be analyzed as well. In Figure 3.7 the binding energies of W $4f_{7/2}$ (a) and Sn $3d_{5/2}$ (b) are shown as a function of the NiO_x layer thickness. The fitted core level spectra can be found in Figure A4 and A5. All different oxidation states (W^{6+}, W^{5+}, Sn^{2+}, and Sn^{4+}) are shown separately. For W^{6+} a shift towards lower binding energies of up to ~0.4 eV can be found. A significant shift of the W^{5+} peak position, in contrast, is not observed. The NiO_x deposition seems to have no impact on the W^{5+} binding energy; see next paragraph for discussion of this observation. The Sn $3d_{5/2}$ peaks (i.e., Sn^{2+} and Sn^{4+}) also exhibit a shift towards lower binding energy of up to ~0.4 eV, which saturates after deposition of 10 nm NiO_x. This is the same magnitude of binding energy shift as seen for the W^{6+} peak. The correlated shift in the binding energy of W^{6+}, Sn^{2+}, and Sn^{4+} indicates a change in band bending at the surface of α-$SnWO_4$,

induced by the deposition of NiO_x. In general, a shift to lower binding energies translates to an upward bending of the energy bands at the surface/interface of the film.

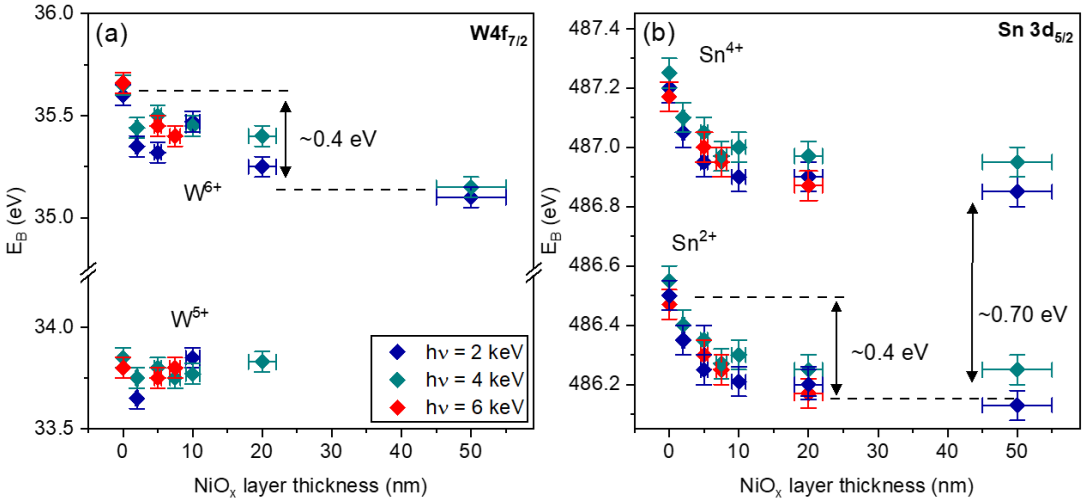

Figure 3.7. (a) Binding energies of W $4f_{7/2}$ core levels extracted from peak fitting procedure. For all photon energies of the W^{6+} contribution, a decrease of the binding energy is found with an increasing NiO_x thickness, whereas the peak position of the W^{5+} contribution remains relatively constant. (b) The peak positions of the Sn^{2+} and Sn^{4+} contributions shift to lower binding energies with an increasing NiO_x thickness. The binding energy shift of W^{6+}, Sn^{2+}, and Sn^{4+} occurs in a similar magnitude of ~0.4 eV and is attributed to an electronic shift to lower energies. This corresponds to upwards band bending at the surface/interface.

A shift of the binding energies and, therefore, the presence of band bending cannot be observed in the Ni 2p core level spectra (see Figure A7 for the spectra). Consequently, additional band bending at the interface is only located in α-$SnWO_4$. The presence of additional band bending introduced by overlayer deposition is also reported in literature, for example for $BiVO_4$ with various overlayers,[170-171] and metal oxide/Si buried junction photoabsorbers.[132, 172] In these studies, an improvement of the performance was explained by the additional band bending. In the present study, the band bending introduced by the deposition of NiO_x is accompanied by a decrease of the ΔOCP (~the photovoltage), as shown Figure 3.1. Consequently, a phenomenon seems to be present that negates the favorable effect of band bending. Here, this is attributed to the significant oxidation of Sn^{2+} to Sn^{4+} as the origin for the limitation of the photovoltage. Details of the underlying mechanism are discussed in the following Chapter 3.4.

As observed in Figure 3.7a, the peak of the W^{5+} contribution does not follow the peak shift to lower binding energies as the other oxidation states (W^{6+}, Sn^{2+} and Sn^{4+}), which is inconsistent with the assignment to band bending described above. The origin of this inconsistency cannot be fully clarified here, although there are two possible reasons for this. First, this may indicate

that W^{5+} is part of a separate phase that does not exhibit the same band bending as the α-$SnWO_4$ phase. The structure of the W^{5+} containing phase may be amorphous and would, therefore, not be visible in XRD. And the second possible reason is the distribution of W^{5+} within the sample. W^{5+} has a higher contribution in the bulk of the material and may, therefore, be less sensitive to the interface phenomenon of band bending in comparison to the other oxidation states, which have a higher relative contribution at the interface.

3.4. Correlation between the α-$SnWO_4$/NiO_x interface investigation and the limited photovoltage

In the following, the correlation between the observed Sn^{2+} to Sn^{4+} oxidation and the reduced photovoltage upon NiO_x deposition is discussed. First, the impact of Sn^{4+} defects on the electronic structure of α-$SnWO_4$ is considered with the help of electronic structure calculations performed with a DFT/HSE06 method.[1] Similar approaches have been reported in the literature for pristine α-$SnWO_4$.[111, 114] A 2 x 2 x 16 supercell model was used, which contains 16 functional units of $Sn_{16}W_{16}O_{64}$ (i.e., 96 atoms of the orthorhombic α-$SnWO_4$ crystal lattice). Using a compensation approach to investigate the presence of Sn^{4+}, several self-defective structures were analyzed by introducing either W-, Sn-, O- vacancies, or anti-site defects (Sn-antisite on W and W-antisite on Sn) in the crystal lattice of α-$SnWO_4$. Different spin multiplicities were considered to obtain the most stable spin configuration. More details on the DFT methodology can be found in the publication based on this chapter.[92] Among the above mentioned defect models, only the case of W-vacancies being present in the lattice could represent the possible presence of Sn^{4+} defects. More details about the other structures can be found in Figure A10 and A11. In the DFT calculation, the orthorhombic crystal structure of pristine α-$SnWO_4$ and α-$SnWO_4$ containing Sn^{4+} defects (compensated by W-vacancies) were used, which are depicted in Figure 3.8a and (b). In (c) and (d) the density of states (DOS) is shown for both cases as a function of the band energy. Indirect transitions between the occupied Sn $5s^2$ + O $2p^6$ and the unoccupied W $5d^0$ states define the band gap, which is 1.5 eV in the DFT model. This agrees with the experimental band gap of 1.9 eV,[90] as the used DFT approach generally tends to underestimate the band gap.

An impact on the size of the band gap by the introduction of W-vacancies cannot be observed in (d). A narrow state, however, can be found approximately in the middle of the band gap when Sn^{4+} defects are present. Note that in this model the triplet state is the most stable configuration and, therefore, the spin up (dashed line) and spin down (solid line) component are shown. The

[1] DFT calculations were performed by collaboration partner Dr. Moussab Harb.

partial charge density map (see Figure A12) suggests a highly localized character of the gap state. Fermi level pinning and, consequently, a restriction of the photovoltage may originate from the presence of such mid-gap states.[119, 173]

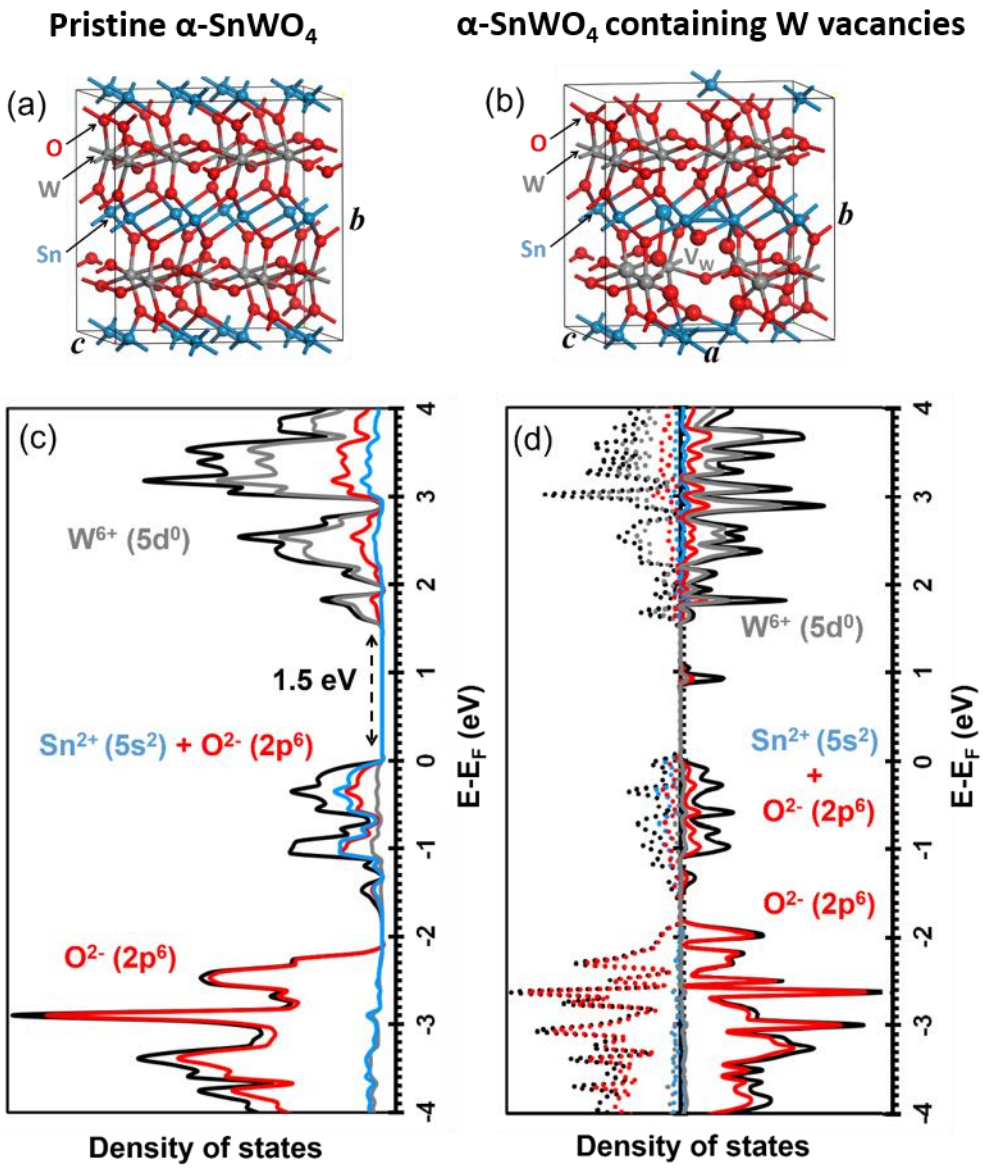

Figure 3.8. (a) Orthorhombic crystal lattice of pristine α-$SnWO_4$ (*Pnna* space group) used in the DFT calculation. (b) α-$SnWO_4$ crystal lattice containing W-vacancies introduced as compensating defects for Sn^{4+}. (c) Density of states (DOS) of pristine α-$SnWO_4$ calculated by the DFT/HSE06 method based on the crystal lattice shown in (a). In (d) the DOS is shown for the α-$SnWO_4$ crystal lattice containing W-vacancies. In this model, the triplet spin state is the most stable configuration. The dashed lines represent the spin-up component and the solid line represents the spin-down component.[92]

At first glance, the presence of the mid-gap state in the W-vacancy containing structure may explain the observed restriction of the photovoltage. However, a critical assessment of the proposed defect model in the DFT calculation is required, before a definite statement can be made. Here it is important to assess the probability for the presence of W-vacancies in the α-$SnWO_4$ films in the present study. Three aspects about the samples and experimental observations are considered as arguments against the presence of W-vacancies. First, Rutherford backscattering spectrometry (RBS)[2] showed earlier that α-$SnWO_4$ films prepared in the same way as in the present study are generally slightly W-rich, which makes the presence of W-vacancies unlikely.[90] The second argument is based on the HAXPES data. If W-vacancies would be introduced to compensate the increase of the Sn^{4+} contribution with increasing NiO_x layer thickness, it would be expected that the Sn/W ratio also increases with increasing NiO_x thickness. The HAXPES data shown in Figure A13, however, show a *decrease* in the Sn/W ratio. Finally, the expected defect formation enthalpy needs to be considered. Due to electrostatic reasons, this would probably be very high due to the high formal oxidation state of W (6 +). Consequently, based on these three arguments, it is unlikely that a significant amount of W-vacancies that would be required to compensate the high contribution of Sn^{4+} seen in Figure 3.6d, is present in the investigated α-$SnWO_4$ films.

An alternative explanation for the observed increase in Sn^{4+} is the formation of a secondary phase at the α-$SnWO_4$/NiO_x interface. Although the deposition of NiO_x by PLD was performed at room temperature, the formation of the secondary phase could originate from the presence of the O_2 plasma during the PLD process. This suggestion is supported by preliminary experiments, where α-$SnWO_4$ was intentionally exposed to an O_2 plasma. A similar increase of the relative Sn^{4+} contribution could be observed (not shown). Secondary phase formation at the interface of film-overlayer systems is known in the literature. For instance, this is reported for Cu_2O/ZTO (zinc-tin-oxide) and Si/HfO_2 material systems.[174-176] The question in the present study is now, what composition the proposed interfacial layer has. One possibility for this secondary phase is found in the literature, where the presence of the $Sn_{0.23}WO_3$ impurity phase in α-$SnWO_4$ films has been reported.[91, 177] However, this impurity phase does not contain the Sn^{4+} oxidation state. Instead, the presence of Sn^{2+} and Sn^0 is reported[178] and, therefore, the increase of the Sn^{4+} contribution in the present study cannot be explained by the formation of this phase. Theoretical calculations in the Materials Project suggest $Sn(WO_4)_2$ as another possible phase. [179]

[2] Rutherford backscattering spectrometry (RBS) is a powerful non-destructive technique that allows to determine the film stoichiometry without the need for a standard with known stoichiometry.

Experimental evidence for this phase, however, has not been reported to be best of the authors knowledge.

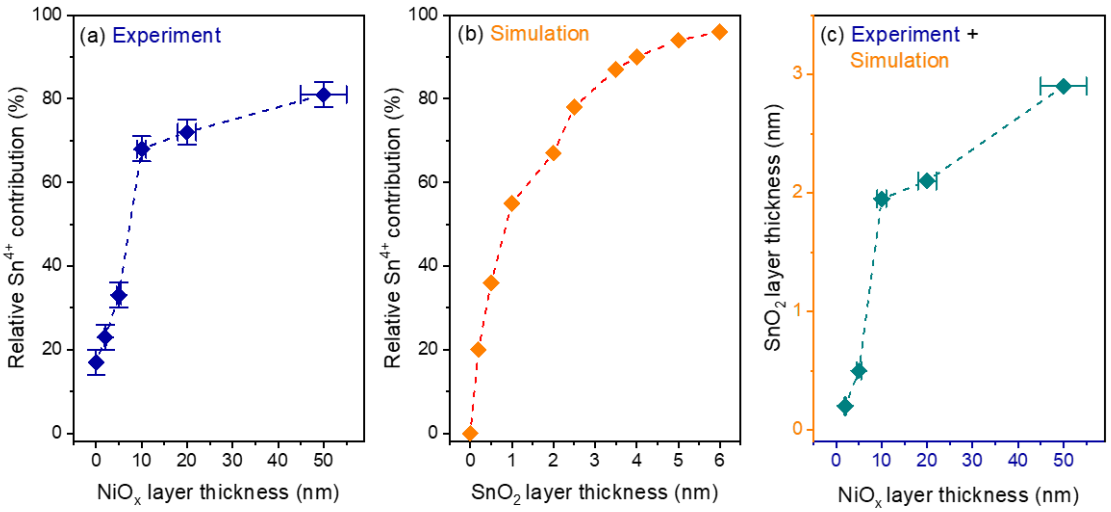

Figure 3.9. (a) Experimental Sn^{4+} contribution measured on α-$SnWO_4$/NiO_x samples with a photon energy of 2 keV. The measured data are also shown in Figure 3.6b and (d). (b) Sn^{4+} contribution extracted from simulated photoemission data using the SESSA (Simulation of Electron Spectra for Surface Analysis) software package. Simulation of the peak intensities is based on a Monte-Carlo algorithm and was performed for hν = 2 keV. In the model α-$SnWO_4$ is coated with an increasing thickness of SnO_2 and from each Sn 3d spectrum the Sn^{4+} contribution is extracted. (d) Combination of experiment and simulation to estimate the expected SnO_2 layer thickness. For different SnO_2 layer thicknesses in (b) the NiO_x layer thickness is taken from (a), at which the Sn^{4+} contribution is the same. In this model the 20 nm NiO_x sample has an interfacial SnO_2 layer thickness of 20 nm.

It is speculated that the secondary phase formed, at the interface of α-$SnWO_4$ and NiO_x, is SnO_2. Whether this interfacial oxide layer can be correlated with the experimental observations is qualitatively assessed with the help of a Monte Carlo-based photoemission peak intensity simulation using the SESSA[3] software package.[180] In the model of the simulation, pristine α-$SnWO_4$ is coated with an increasing thickness of SnO_2. For each SnO_2 thickness core level spectra are simulated, and the Sn^{4+} contribution is extracted from the Sn 3d core level. To reduce the complexity of the simulation, the NiO_x overlayer is not included. The presence of NiO_x would only attenuate the Sn 3d core levels, which are the spectra of main interest in the simulation, and would not influence the relative ratio of Sn^{2+} and Sn^{4+}. This ratio is also independent on the location of the species within the sample (i.e., surface/interface or bulk). More details of the simulation are given in Figure A14. In Figure 3.9 the correlation of the experimental data with the simulation is presented. Panel (a) shows the experimental Sn^{4+}

[3] Simulation of electron spectra for surface analysis

contribution measured with hν = 2 keV as a function of the NiO_x layer thickness. The simulated Sn^{4+} contributions for the α-$SnWO_4$/SnO_2 system are shown in (b) as function of the SnO_2 layer thickness. The expected thickness of the SnO_2 layer shown in (c) can be estimated by comparing the NiO_x layer thickness in (a) with the SnO_2 thickness in (b) for specific Sn^{4+} contributions. That is, the Sn^{4+} contribution is determined by reading off the SnO_2 thickness for which the Sn^{4+} contribution is the same as for a particular NiO_x layer thickness. An increase of the NiO_x thickness corresponds to an increase of the interfacial layer thickness and can, therefore, explain the observed increase of the Sn^{4+} contribution in Figure 3.6d. For the most relevant NiO_x thickness of 20 nm, which corresponds to the sample that shows the highest reported photocurrent density,[90] the interfacial layer is estimated to be ~2 nm. This is considered to be thin enough for charge transfer across the interface (i.e., tunneling). However, this insulating layer may have a negative impact on the properties of the α-$SnWO_4$/NiO_x interface, and may be the origin of the limited photovoltage. The presence of this layer is also visually suggested by transmission electron microscopy (TEM). An image of a α-$SnWO_4$ film coated with 20 nm NiO_x is shown in Figure 3.10, where the location of the interfacial layer is shaded in yellow on the right side of the image.

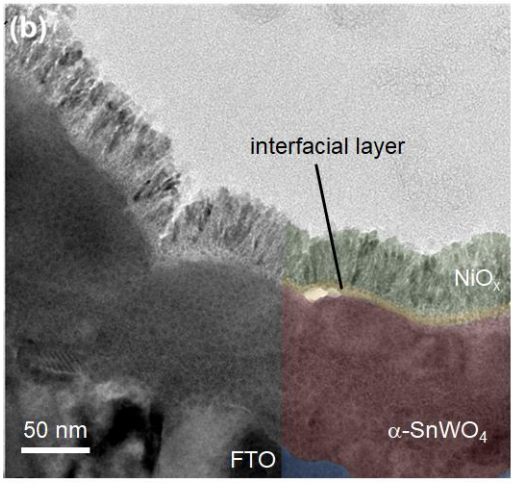

Figure 3.10. Transmission electron micrograph of a α-$SnWO_4$ film coated with 20 nm NiO_x. Indication for the proposed oxide layer formation can be observed, visualized by the yellow shade on the right side of the image.

At this point, it is important to assess whether this interfacial layer can be responsible for the limitation of the photovoltage shown in Figure 3.1. Also here ΔOCP measurements provide a useful tool to address this issue. Pristine α-$SnWO_4$ films were intentionally oxidized by a performing photoelectrochemical measurements, which earlier has been shown to induce a SnO_2 layer at the surface of α-$SnWO_4$.[90] Chronoamperometry measurements, with an applied potential of 1.23 V vs. RHE, were performed under AM1.5 illumination. After several steps the

ΔOCP was determined, which is presented in Figure 3.11. The x-axis represents the amount of transferred charge *Q* across the interface, which was calculated by integrating the current-time data. Using the density of SnO_2 (7.02 g cm^{-3} taken from JCPDS 00-041-1445), the thickness of this surface layer can be estimated, as shown at the top-axis of the graph. Qualitative agreement is found between the reduction in ΔOCP with an increasing SnO_2 layer thickness and the reduction in ΔOCP after deposition of NiO_x (see Figure 3.1). SnO_2 layer formation on α-$SnWO_4$ can indeed be the origin of a reduced photovoltage. Therefore, we conclude here that the interfacial oxide layer formed at the interface of α-$SnWO_4$ and NiO_x is likely to be responsible for the observed behavior of the ΔOCP.

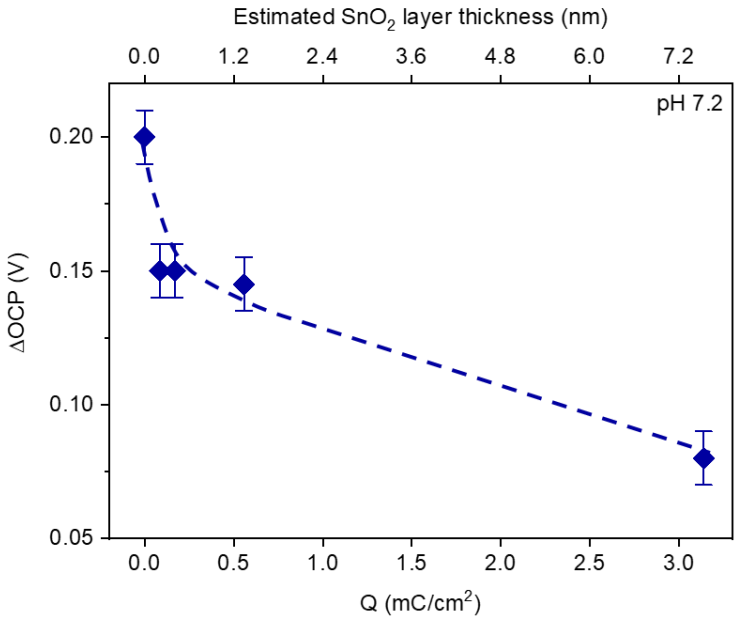

Figure 3.11. Control experiment to correlate the photovoltage with the formation of a thin SnO_2 layer on top of α-$SnWO_4$. A pristine α-$SnWO_4$ film was subjected to photoelectrochemical treatment at 1.23 V vs. RHE in pH 7.2 electrolyte (KP_i + Na_2SO_3 as hole scavenger). The transferred charge *Q* was obtained from integrating the current-time data and is correlated with the ΔOCP, which was determined at several points. From the charge *Q* (and the SnO_2 density of 7.02 g cm^{-3} taken from JCPDS 00-041-1445) the SnO_2 layer thickness can be estimated, and is shown on the top x-axis. Oxidation of Sn^{2+} to Sn^{4+} and, therefore, an increase of the SnO_2 layer can be correlated with a decrease in ΔOCP. This qualitatively agrees with the decrease in ΔOCP for NiO_x-coated samples observed in Figure 3.1. As a guide for the eye a dashed blue line is shown.

Finally, it should be noted that the study presented in this chapter complements the previously reported work.[90] In this work, it was suggested that NiO_x overlayer deposition prevents electrochemical oxidation of Sn^{2+} to Sn^{4+}, based on the observation that a stable photocurrent for at least 30 min could be achieved. Additional understanding of the underlying mechanism can be deduced from the present study. Partial oxidation of the α-$SnWO_4$ is already induced by

the NiO_x deposition. The thickness of the formed interfacial layer is, however, limited and allows for higher charge transfer rates in comparison to a thick surface layer formed by (photo)electrochemical oxidation (> 7 nm). Thus, the NiO_x overlayer prevents further oxidation, but limits the photocurrent by a hole-blocking SnO_2 layer.

3.5. Summary and conclusion

In this chapter, a detailed analysis of the α-$SnWO_4$/NiO_x interface was presented, with the goal to unravel the origin of the limitation of the photovoltage by the presence of the NiO_x layer. The photovoltage limitation was confirmed by OCP analysis, and correlated with the NiO_x layer thickness. A synchrotron-based HAXPES investigation revealed upwards band bending at the surface of α-$SnWO_4$, introduced by the deposition of PLD NiO_x. However, significant oxidation of Sn^{2+} to Sn^{4+} with increasing NiO_x layer thickness was also observed, which follows the trend of the decreasing photovoltage determined by the OCP analysis. The spectroscopic investigation was complemented with DFT calculations and Monte Carlo-based photoemission peak intensity simulation. Formation of a thin interfacial SnO_2 layer was proposed, which correlates with the increase of the Sn^{4+} contribution at the interface. In Figure 3.11 this correlation is illustrated. An interfacial oxide layer thickness of ~2 nm was estimated for the α-$SnWO_4$ film coated with 20 nm NiO_x, which is the NiO_x thickness that gives the highest photocurrent density. In principle charge carrier transport by tunneling through this layer can still be possible. A control experiment in which OCP analysis of photoelectrochemically oxidized α-$SnWO_4$ was performed, showed that such an oxide layer can indeed be responsible for the reduction of the photovoltage. Consequently, it was suggested that the limitation of the photovoltage is related to the presence of the interfacial oxide layer, and does not originate from the direct contact of α-$SnWO_4$ and NiO_x. The nature of the underlying mechanism, resulting in the interface limitation due to the presence of the thin oxide layer, is explored in more detail in the following chapter. In future research efforts alternative deposition methods for the overlayer deposition should be developed, which prevent the oxidation of the α-$SnWO_4$ surface. Another option is the introduction of passivation layers, for instance, in the form of self-assembling monolayers as reported for perovskite solar cells.[181-182]

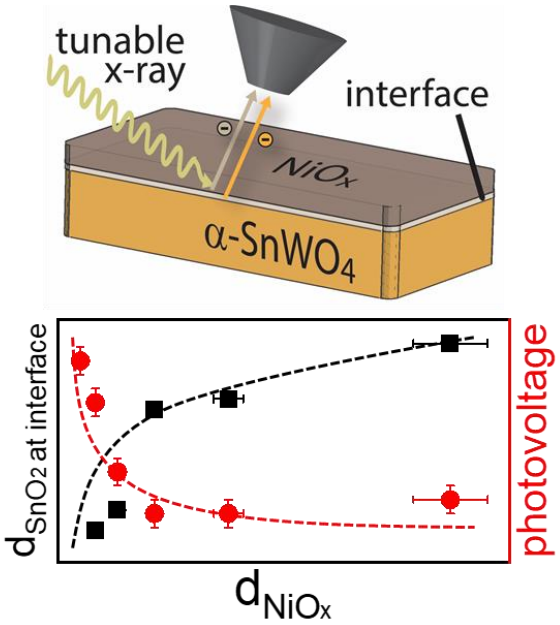

Figure 3.12. Summary of the results of the α-$SnWO_4$/NiO_x interface investigation with respect to the photovoltage. The combination of the HAXPES data and the photoemission spectra simulation revealed the formation of a thin interfacial oxide layer at the interface of α-$SnWO_4$ and NiO_x. The increasing thickness of the interfacial layer, with increasing NiO_x layer thickness, can be correlated with the decrease of the photovoltage (approximately determined by ΔOCP).

4. Intra-band gap states in α-$SnWO_4$ photoanodes introduced by surface modification

Parts of this chapter are included in the following publication:

Patrick Schnell, Erwin Fernandez, Keisuke Obata, Jennifer Velázquez Rojas, Thomas Dittrich, Roel van de Krol and Fatwa F. Abdi

In preparation

4.1. Introduction

Thin film α-$SnWO_4$ photoabsorbers possess promising properties for photoelectrochemical water splitting. However, as discussed in detail in the previous Chapter 3, the photocurrent improvement achieved by NiO_x overlayer deposition on α-$SnWO_4$ films is accompanied by a limitation of the photovoltage. This was confirmed by OCP analysis and has been attributed to the interfacial oxide layer formation originating from the oxidation of Sn^{2+} to Sn^{4+}. Although a clear correlation with the photovoltage limitation could already be shown by our control experiments, the details of the underlying mechanism of this observation are not fully clear at this point. Detailed understanding of the nature of the limitation can help to find tailor-made solutions to overcome the limitation, and to generate further progress in the development of α-$SnWO_4$ photoelectrodes.

One possibility is that the underlying mechanism is related to the presence of intra-band states. Gap states or surface states are often discussed for other materials in the literature.[169, 172, 183] In the previous chapter, it could be ruled out that surface states are introduced by the exposure to air during the handling of α-$SnWO_4$ films. The formation of the interfacial oxide layer, however, may introduce gap states at the interface. Such states could not be observed in the HAXPES study in Chapter 3. However, the signal from the valence band of p-type NiO_x, which overlaps with the valence band maximum of α-$SnWO_4$, may have concealed the presence of intra-band states. In addition, the density of states of such features may be very low and difficult to detect in the HAXPES measurement. In the present chapter, therefore, surface photovoltage (SPV) measurements and photoemission spectroscopy with the aim for resonant enhancement of element-specific features (ResPES) complement the spectroscopic tools in this study to investigate this issue in more detail. SPV measurements can provide valuable information on electronic properties and charge carrier recombination, and have been used on a wide range of

materials in previous reports.[161, 184-187] Reports on SPV analysis of α-$SnWO_4$ are, however, absent from the literature. Although valuable information can be obtained from the modulated SPV measurements, detailed analysis can be difficult due to superposition of several effects. Complementary methods may be necessary to obtain more detailed understanding. ResPES was performed at BESSY II at HZB by a combination of X-ray absorption spectroscopy (XAS) and HAXPES. This technique has been proven to be powerful in the investigation of gap states, for example, in Mo- or W-doped $BiVO_4$.[188-190] Under resonant conditions, the signal related to states with a low density of states within the band gap may be enhanced. In the present chapter, we put special focus on the α-$SnWO_4$/SnO_2 interface, which represents the nature of the interfacial layer proposed in the previous chapter. Detailed analysis of the interfacial features was performed by HAXPES as well.

4.2. Surface photovoltage analysis

Surface photovoltage analyses were first performed on pristine α-$SnWO_4$ and α-$SnWO_4$/NiO_x films, to investigate the impact of the NiO_x layer. The photovoltage amplitude *R* is presented in Figure 4.1 as a function of the photon energy. For the definition of *R* see equation 2.7. Above the band gap energy of α-$SnWO_4$, the amplitude increases with increasing NiO_x layer thickness. This correlates with the band bending trend observed in Figure 3.7, where an increasing band bending was observed for an increasing NiO_x layer thickness. Although the enhanced SPV signal of NiO_x coated films suggests improved separation of charge carriers, a substantial proportion of the charge carriers may recombine via defect-mediated processes. The SPV signal can in general have contributions of free charge carriers and trapped charge carriers, as described in more detail in Chapter 1.7. The signal between 0.5 – 1.5 eV in Figure 4.1 is probably related to transitions from surface states or bulk defect states. This will be discussed in more detail below.

To further elucidate the process in more detail, especially regarding trapping of charge carriers during recombination, the in-phase signal *X* and out-of-phase signal *Y* (phase shifted by 90°) are now individually resolved. In Figure 4.2 the fast (i.e., *X* signal) and slow response (i.e., *Y* signal) of the three samples are shown, which were measured with a modulation frequency of f_{mod} = 8 Hz. First, we turn our attention on the energy region above the band gap of α-$SnWO_4$. In this region, band-to-band transitions, followed by spatial redistribution, are responsible for the generation of the *X* and *Y* signal, as schematically illustrated in Figure 4.3a.[164] The signs of the *X* and *Y* signals indicate the preferential direction, in which the generated charge carriers move.[166] The positive *X* signal observed above the band gap energy indicates that electrons contributing to the fast response are preferentially moving away from the surface of α-$SnWO_4$, i.e., towards the FTO back electrode. This preferential direction of charge separation is indicated

by the arrows in Figure 4.3a. Although dependent on the exact nature of the charge carrier relaxation mechanism, the fast response (*X*) signal is typically assigned to the generation and spatial redistribution of free charge carriers that recombine via fast processes.[166] As illustrated by the black arrow in Figure 4.3d, a possible fast recombination process may occur via direct band-to-band transitions without involvement of intermediate trapping in defect states.

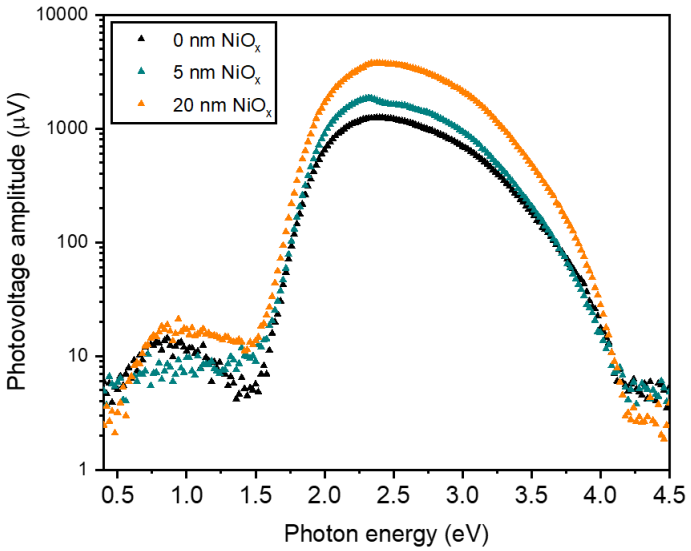

Figure 4.1. Surface photovoltage amplitude *R* of a pristine α-$SnWO_4$ film and α-$SnWO_4$/NiO_x samples. The amplitude is defined as the square root of the sum of the squares of the *X* and *Y* signals (equation 2.7). For an increasing NiO_x layer thickness, the amplitude above the band gap increases, indicating enhanced charge separation. This follows the same trend as the trend observed for the band bending upon deposition of NiO_x in Figure 3.7. An indication for charge carrier generation below the band gap can be seen as well, which indicates the presence of surface states or bulk defect states.

For the *Y signal*, preferential movement away from the surface of α-$SnWO_4$ is indicated by a *negative* signal due to the 90° phase shift. In this slow response signal often charge carriers dominate, which recombine via trap-mediated processes.[166] Possible relaxation processes that may contribute to the slow *Y* signal are illustrated in Figure 4.3d. Relaxation may occur via intermediate trapping in bulk defect states or surface states. Note, however, that without complementary measurement techniques we cannot definitely assign the observed *X* and *Y* signals to specific physical processes. The signals may arise from a combination of different processes, which depending on their time scales, either contribute to the fast or slow response signals.

Overall, the opposite signs of the *X* and *Y* signals indicate preferential charge separation in the same direction. This is true for all three samples independent on the NiO_x layer thickness. Preferential movement of electrons towards the FTO back contact is generally expected for an

n-type semiconductor such as α-$SnWO_4$. As already observed in Figure 4.1, with increasing NiO_x thickness, the SPV signals (both *X* and *Y*) above the band gap increase in Figure 4.2. Most notably, the amplitude of the *Y* signal (slow response) increases more than that of the *X* signal (fast response) for the sample with 20 nm NiO_x (see Figure 4.2), which causes the increase of the overall photovoltage amplitude shown in Figure 4.1. This suggests that the deposition of 20 nm NiO_x may lead to enhanced trapping during charge relaxation. The possible consequence of this observation is discussed below.

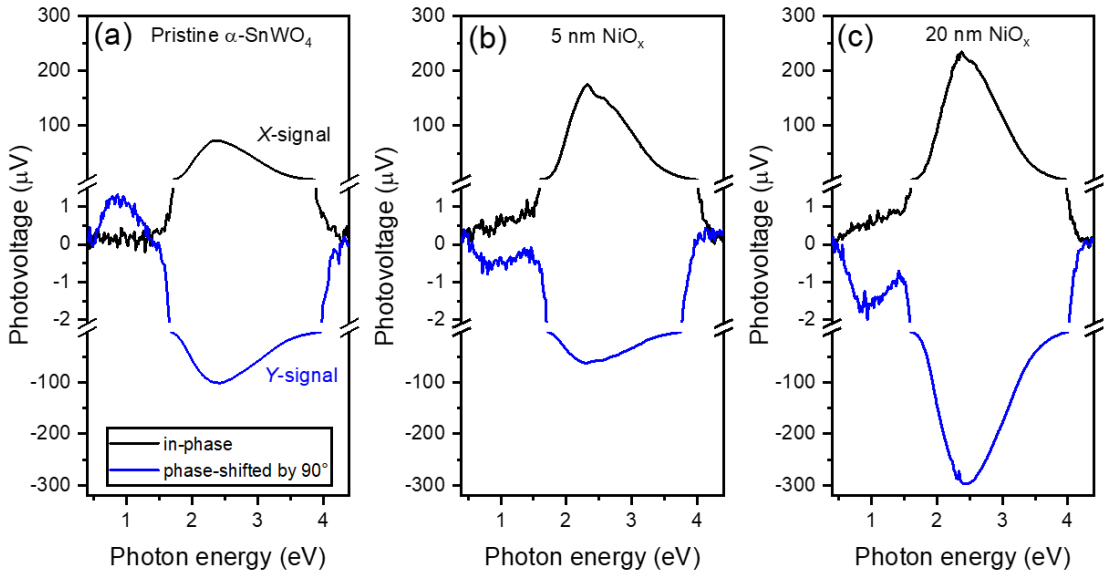

Figure 4.2. In-phase (*X*) and out-of-phase (*Y*) signals of modulated surface photovoltage measurements of a pristine α-$SnWO_4$ film (a), and α-$SnWO_4$ films coated with 5 nm and 20 nm NiO_x (panel b and c respectively). The modulation frequency of the light was f_{mod} = 8 Hz. Deposition of NiO_x has a clear impact on the modulated SPV signals, especially below the band gap energy. This can also be seen in the analysis of the phase angle, which can be found in the Appendix B, Figure B1.

We now turn our attention on the region below the band gap of α-$SnWO_4$ in Figure 4.2. Below the band gap, generation of the SPV signal can in general occur from surface or bulk defect states through sub-band gap absorption.[164] Possible sub-band gap transitions, followed by spatial redistribution, are indicated in Figure 4.3b and (c). For the pristine α-$SnWO_4$ sample, only a slow response signal can be observed below the band gap energy (blue curve in Figure 4.2a). The signal has a positive sign and, therefore, separated charge carriers have an opposite preferential direction in comparison to the energy region above the band gap, i.e., electrons move towards the surface. A possible process that may be consistent with this, is a bulk defect-to-band transition followed by a slow relaxation via trapping in a surface state. Such a process is schematically illustrated in Figure 4.3e.

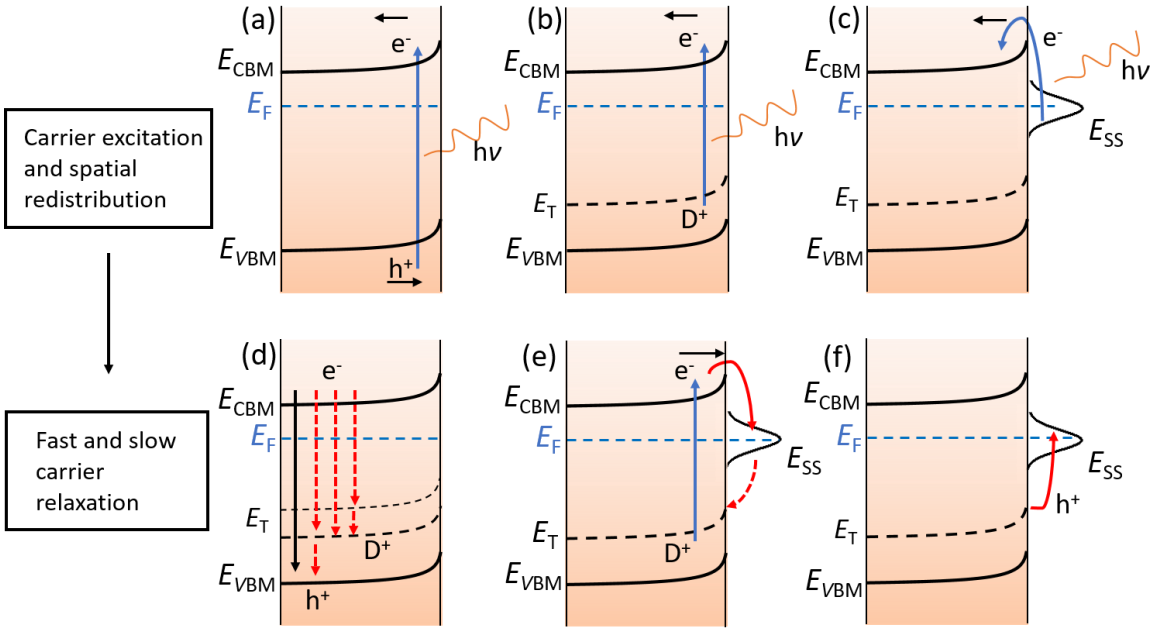

Figure 4.3. Schematic illustration of possible charge carrier excitation mechanisms, spatial redistribution, and relaxation processes during the generation of a SPV signal. (a) Band-to-band transition followed by spatial redistribution of e^- and h^+ as indicated by the arrows. (b) Bulk trap-to-band transition followed by separation of e^- and ionized donor D^+ with energy level E_T. (c) Surface state-to-band transition. (d) Different relaxation mechanisms via band-to-band recombination (black arrow) or bulk defect-mediated processes indicated by the dashed red arrows. The time scales of these processes either result in a fast or slow response signal. (e) Trapping of an e^- in a surface state and relaxation into a bulk state. The presence of such a relaxation process may alter the preferential direction of e^- in (b) towards the surface, and result in a positive slow response signal. (f) Trapping of a h^+ in a surface state.[164, 191-192] Note that the SPV signals cannot be definitely assigned to specific processes without complementary analysis.

The situation is modified by the deposition of NiO_x. A fast and positive response signal (*X*) is observed in addition to the slow response signal (*Y*) that now has a negative sign. Recall that opposite signs for *X* and *Y* indicate that the slow and fast charge carriers move in the same direction. For the negative sub-band gap slow response signal, charge carrier trapping in bulk defect states or surface states (see Figure 4.3d and (f)) may be responsible. In these processes, electrons are preferentially separated towards the FTO back electrode and, therefore, in the opposite direction compared to the slow response signal of the pristine film. The positive fast response signal after deposition of NiO_x may be related to spatial charge separation towards the FTO back electrode followed by fast relaxation mechanisms, as indicated in Figure 4.3b and (d). For the α-$SnWO_4$ film coated with 20 nm NiO_x (Figure 4.2c), the slow response signal increases, which is attributed to enhanced charge carrier trapping. At the same time no noticeable increase of the fast response signal below the band gap region is observed for increasing NiO_x thickness. These observations are also found in the phase angle analysis of the SPV signal, as described in more detail in Figure B1.

Overall, the SPV analyses suggest the modification of the charge generation, separation, and relaxation processes in α-$SnWO_4$ films upon NiO_x deposition. This is especially observed for the sub-band gap transitions. The overall modifications upon deposition of NiO_x may be related to the results in Chapter 3. Remember that in Chapter 3 it was suggested that a mechanism exists, which negates the favorable band bending upon deposition of NiO_x. It was proposed that this process may be responsible for the photovoltage losses. The identification of this modification is discussed next with the help of photoemission spectroscopy.

4.3. Investigation of the α-$SnWO_4$/SnO_2 interface by Hard X-ray Photoelectron Spectroscopy

Motivated by the interfacial SnO_2 layer formation at the interface of α-$SnWO_4$ and NiO_x in the previous chapter, an investigation of the interface between α-$SnWO_4$ and SnO_2 was performed using HAXPES. As already described in more detail in Chapter 2.3 and 3.3, this technique allows us to de-convolute spectral features arising from the surface/interface and the bulk of the investigated materials. It is therefore suitable to detect the evolution of the chemical states or electronic band shifts at the interface.

Figure 4.4 shows the W 4f and Sn 3d spectra of α-$SnWO_4$/SnO_2 (red), which are compared with the spectra measured on pristine α-$SnWO_4$ (black). Note that the photon energies indicated in the graphs are slightly different in comparison to the previous chapter, to align the core level measurement with the following ResPES analysis (vide infra). The SnO_2 layer was formed by photoelectrochemical oxidation at 1.23 V vs. RHE in pH 7 KP_i. An SnO_2 layer thickness of ~1 nm was estimated based on the integrated charge during the oxidation step. A first glance at the W 4f spectral features in Figure 4.4a reveals a small contribution of W^{5+}. This was also observed earlier and was found to have no significant impact on the PEC performance. More details on this can be found in Chapter 3. The relative W^{5+} contributions of the pristine and SnO_2 covered α-$SnWO_4$ films are of comparable magnitude for the measurement with $h\nu$ = 3880 eV. The peak positions of the W^{5+} and the nominal W^{6+} contributions are indicated by the dashed vertical lines in the graph.

Comparing the W 4f spectra of the α-$SnWO_4$/SnO_2 and α-$SnWO_4$ samples, a peak broadening can be observed if SnO_2 is present. An estimation of the FWHM is given in Figure B2, which also reveals that the FWHM increases with increasing SnO_2 thickness. This broadening is attributed to the appearance of an additional W^{6+} species other than that of α-$SnWO_4$. WO_3 is a possible candidate, and was also suggested to be a possible degradation product earlier.[90] However,

band bending may also contribute to peak broadening. More details on this are discussed in the next chapter with respect to the stability of α-$SnWO_4$ photoelectrodes.

The Sn 3d core level spectra of the pristine (black) and the SnO_2-modified (red) films are presented in Figure 4.4b. All peaks show an asymmetry at the higher binding energy side, which indicates the presence of a Sn^{4+} contribution as observed previously.[90, 92] Depending on the probing depth σ (i.e., the photon energy) a clear variation of the Sn^{4+} contribution is found for the α-$SnWO_4$/SnO_2 sample. As expected, the relative contribution of Sn^{4+}, originating from SnO_2 on the surface, decreases for larger probing depths. Samples with a thicker oxidized SnO_2 layer (~12 nm) were also measured. The spectra can be found in Figure B3. These spectra follow the same trends as described here for the sample with the thin SnO_2 layer.

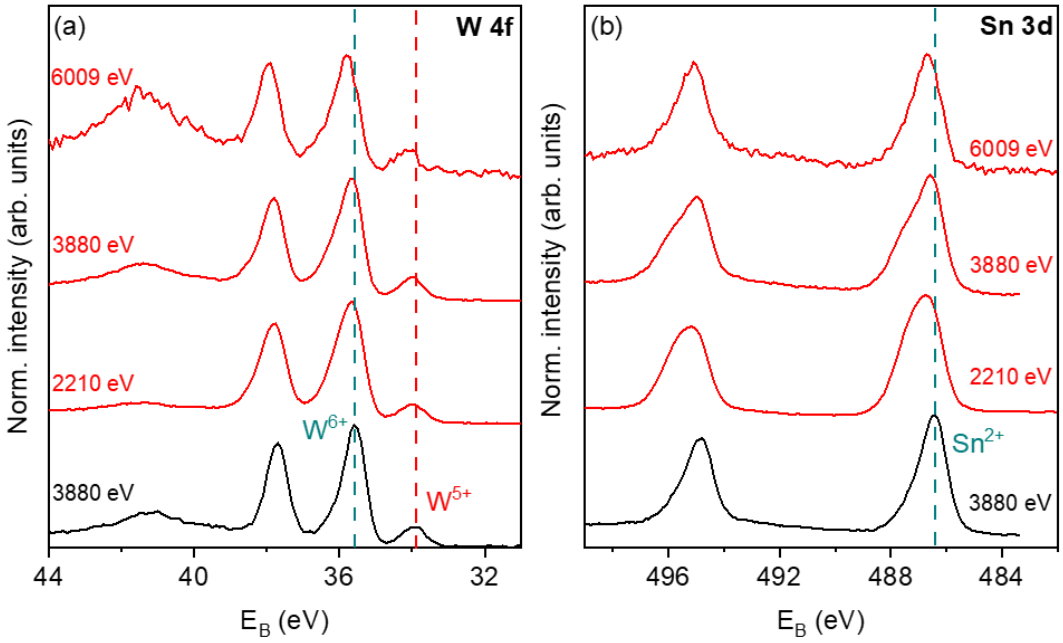

Figure 4.4. (a) W 4f core level spectra measured by HAXPES on a pristine α-$SnWO_4$ film (black) and α-$SnWO_4$/SnO_2 samples (red). A thickness of ~1 nm was estimated for the SnO_2 layer, which was formed by photoelectrochemical oxidation at 1.23 V vs. RHE in pH 7 KP_i. The α-$SnWO_4$ films have a thickness of 100 nm. (b) Sn 3d core level spectra of the same samples measured by HAXPES. Formation of Sn^{4+} can be clearly seen by the peak asymmetry towards higher binding energy. The photon energies used in the measurements are indicated in both graphs. Note that the photon energies are partially different in comparison to the previous chapter, to align the core level measurements with the following ResPES analysis. The peak positions of W^{5+}, W^{6+}, and Sn^{2+} in the pristine film are indicated by dashed vertical lines.

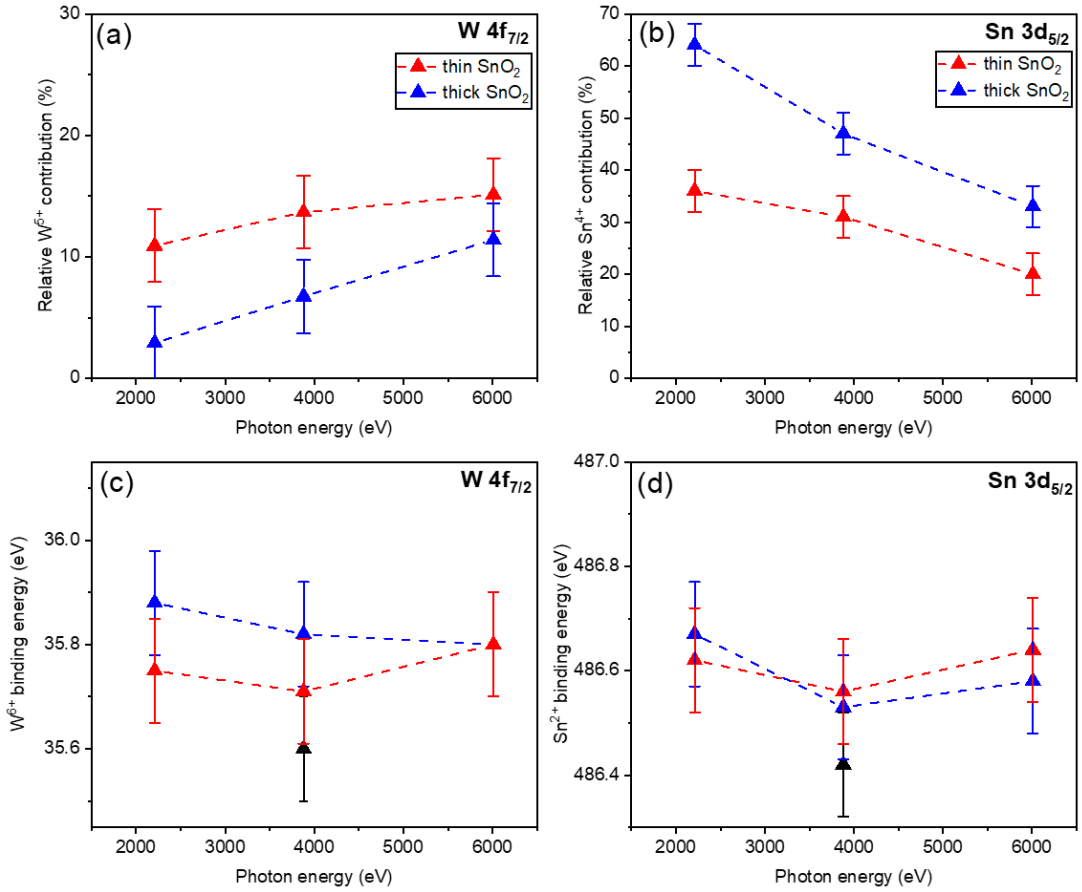

Figure 4.5. (a) Relative W^{5+} contributions extracted from the W $4f_{7/2}$ core level by peak fitting (see Figure B4 for representative fits). (b) Sn^{4+} contributions estimated by peak fitting procedure of the Sn $3d_{5/2}$ core level. The pristine sample was measured with hν = 3880 eV. A W^{5+} contribution of 10 ± 3 % and a Sn^{4+} contribution of 19 ± 4 % were estimated. (c) shows the W^{6+} binding energies and (d) the Sn^{2+} binding energies. The spectra of the thick SnO_2 sample can be found in Figure B3. The size of the error bars for of the binding energy corresponds to the step size (0.1 eV) of the core level measurements.

A quantitative analysis of the relative contributions and binding energies at the interface was performed, using the peak fitting procedure described in Chapter 2.3. The relative W^{5+} and Sn^{4+} contributions are shown in Figure 4.5a and (b). Example fits to selected spectra are shown in Figure B4. An increase of the W^{5+} contribution with an increasing photon energy can be observed. This was also observed in the previous chapter, and was attributed to a higher W^{5+} content in the bulk than at the surface of the sample. For the thin SnO_2 sample, the overall contribution is higher in comparison to the thick SnO_2 layer, which agrees with the finding that W^{5+} is more present in the bulk of α-$SnWO_4$. The pristine film was measured with hν = 3880 eV, and has a W^{5+} contribution of 10 ± 3 %. Acknowledging sample to sample variation, this is of similar magnitude as observed previously.[92] The Sn^{4+} contribution in Figure 4.5b decreases with increasing photon energies, indicating the presence of the SnO_2 layer at the surface. As expected, the contribution is overall higher for the thick SnO_2 sample. A Sn^{4+} contribution of

19 ± 4 % was estimated for the pristine α-$SnWO_4$ film, which is a bit higher than in the previous chapter.

The binding energies for W^{6+} and Sn^{2+} are shown in Figure 4.5c and (d). In both cases, a small increase of the binding energies can be observed for the SnO_2 coated films in comparison to the pristine sample. This may suggest an electronic shift and a slight band bending with the formation of surface SnO_2, but it should be noted that the uncertainty for the estimation of the binding energy is ± 0.1 eV.

4.4. Resonant photoemission spectroscopy

Finally, photoemission spectroscopy of the valence band was performed with the aim for resonant enhancement of element-specific features (ResPES). This was performed at the BESSY II synchrotron facility to reveal the possible presence of intra-band gap states. Measurements were performed on pristine α-$SnWO_4$, α-$SnWO_4$/SnO_2 and α-$SnWO_4$/NiO_x samples. In order to determine the excitation energies required for the valence band measurement under resonant conditions, X-ray absorption spectra of the the Sn L-edge and W M-edge were recorded for the different samples.

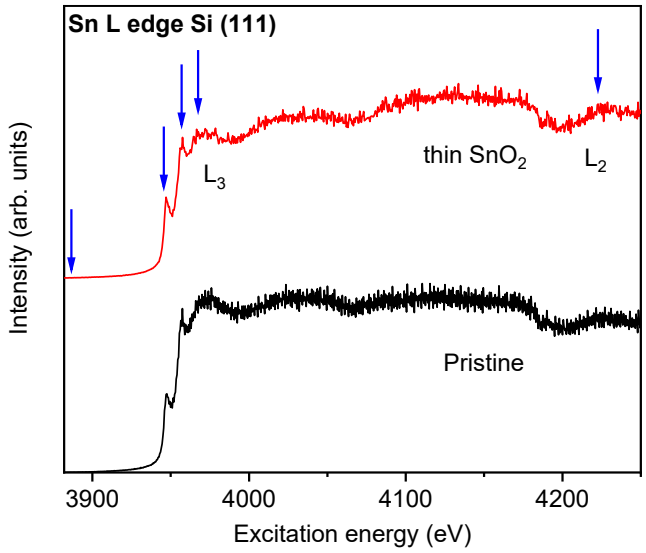

Figure 4.6. Sn $L_{3,2}$-edge measured by X-ray absorption spectroscopy (XAS) on pristine α-$SnWO_4$ and α-$SnWO_4$/SnO_2. The measurements were performed using the Si (111) double crystal monochromator. Clear differences in the absorption edge could not be observed, also for the other samples (see Figure B5). The arrows in the graph indicate the excitation energies used for the valence band spectra measurement in Figure 4.7. A representative measurement of the W M-edge is shown in Figure B6. Note that there are differences in the energies when using different crystal monochromators (see Table B1).

Representative XAS spectra of the Sn $L_{3,2}$-edge are shown in Figure 4.6 for pristine α-$SnWO_4$, and for α-$SnWO_4$ coated with ~1 nm SnO_2. No significant difference can be observed in the presented spectra as well as in the other spectra for NiO_x-coated α-$SnWO_4$ shown in Figure B5. This is expected as XAS probes more of the bulk of the material, i.e., changes in the absorption due to changes of the Sn oxidation state at the surface would not be visible. In addition, only small differences are reported in the absorption edges of Sn, SnO, and SnO_2, even when the whole film exhibits the varying oxidation states.[193] At this point it is briefly noted that a variety of information can be deduced from the detailed interpretation of XAS spectra. For instance, stereochemical information (i.e., atomic coordination, bond length, etc.) can be obtained from interpreting the XANES (X-ray absorption near edge structure) and EXAFS (Extended X-ray absorption fine structure) regions.[194] The detailed interpretation is, however, not the focus of the present study. Instead, the relevance of these spectra is in determining the excitation energies at which the valence band spectra should be taken. These excitation energies are indicated by the arrows in the graph. In the W M-edge spectra clear differences between the different samples cannot be found as well, which was also expected. A representative spectrum can be found in Figure B6.

Valence band spectra of pristine α-$SnWO_4$ and α-$SnWO_4$/SnO_2 samples were recorded with different excitation energies in and out of resonance with the Sn L_3-edge ($h\nu$ = 3880, 3933, 3942, and 3952 eV). The recorded spectra are depicted in Figure 4.7. Note that these spectra were measured with the Si (311) crystal monochromator. As shown in Table B1, there are differences in the energy calibration of measurement with the Si (111) and Si (311). All spectra are normalized to the first maximum at ~2.8 eV, and the plots are shown in a logarithmic scale. First, it is noted that the valence band of the pristine film α-$SnWO_4$ appears as expected.[92] The valence band maximum (VBM) is located at 1.5 ± 0.1 eV and agrees well with a previous report on PLD-deposited α-$SnWO_4$, where a VBM of 1.6 ± 0.1 eV was determined by UPS.[90] For the oxidized samples, the SnO_2 valence band features have a stronger contribution at higher binding energies (> 4 eV), which can be seen by the increasing intensity in this regime with an increasing SnO_2 layer thickness. The most important observation is the presence of an intra-bandgap state above the valence band maximum (peak at ~0.7 eV), which can be seen irrespective of the excitation energies. While the presence of this state can already be vaguely seen in the pristine film, it is clear that it becomes more obvious with the presence of the SnO_2 layer on the surface. It is also noted that the intra-bandgap state is visible as well for the photon energy that was chosen as the non-resonant condition (i.e., $h\nu$ = 3880 eV). Although it is not fully clear why this is the case, there are two possible reasons. First, the chosen energy may not reflect non-resonance

conditions, i.e., it is still not too far from the absorption edge. Second, it is possible that the density of states is sufficiently high so that it is already visible without resonance. In this case, the signal enhancement by performing on-resonance measurements would be rather small as the intensities of the state are similar for the different energies. The notion of a rather weak resonance effect can also be found when the orbital contributions to the valence band are considered. As shown in the electronic structure (Figure 3.8), mainly Sn 5s and O 2p states contribute to the valence band of α-$SnWO_4$. For a strong resonance effect, an enhancement of Sn 5s features in the valence band would be expected in comparison to the off-resonance measurement. Such a strong enhancement is not clearly observed, as there is no significant difference in the valence band shape between off-resonance and resonance conditions.

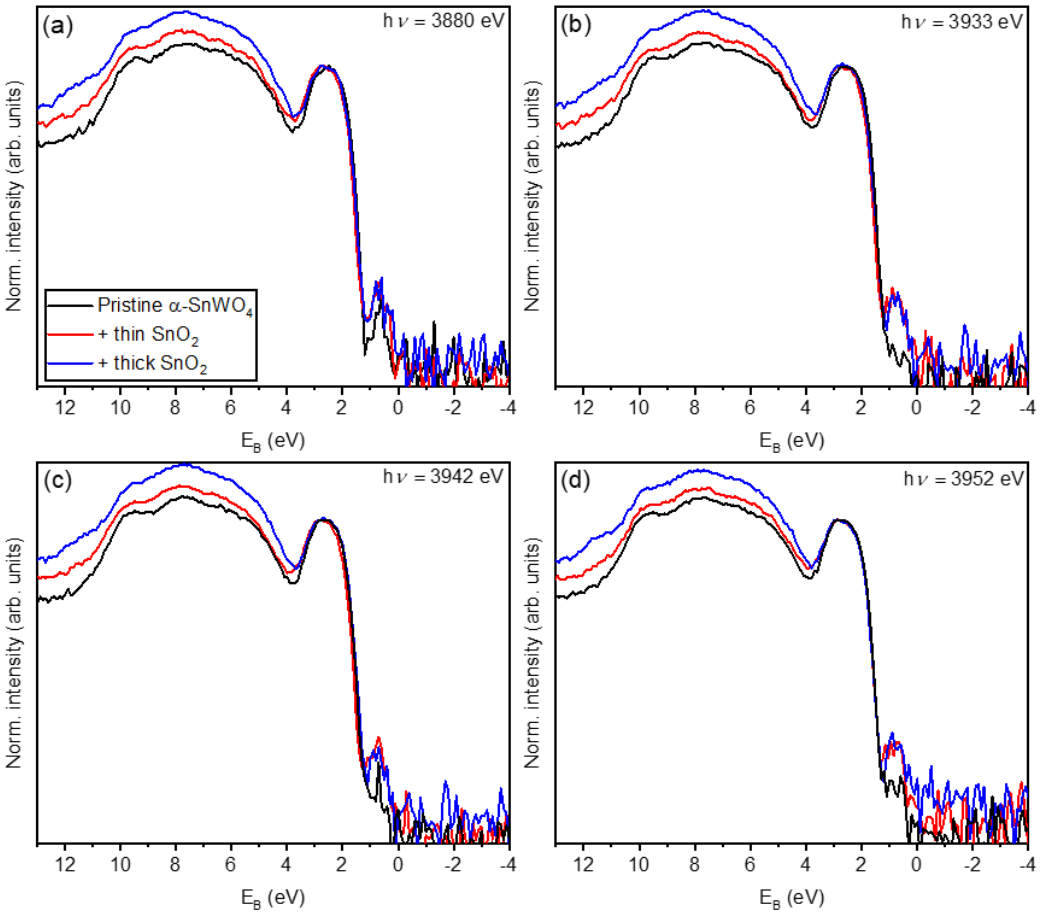

Figure 4.7. Valence band spectra measured by ResPES on α-$SnWO_4$ and α-$SnWO_4$/SnO_2 samples with different photon energies as indicated in the panels. The photon energies were chosen to measure in resonance with the features of the Sn L_3-edge depicted in Figure 4.6. Spectra were normalized to the feature at ~2.8 eV. Note that the intensity scale in all panels is logarithmic. An indication for the presence of an intra-band state above the valence band maximum can be observed, which intensity tends to increase for the SnO_2-coated samples.

Spectra in resonance with the W absorption edge were recorded as well, and can be seen in Figure B8. Due to limitations of the experimentally accessible photon energy at the beamline only the M-edge could be accessed. Three different photon energies were chosen in resonance with the absorption edge (hν = 2210 eV, 2288 eV, and 2585 eV). Presence of a feature above the valence band maximum can be observed as well, which is most prominent for the measurement performed with 2585 eV. Whether this feature is related to an enhancement of the resonance condition with W cannot be defined unambiguously at this point.

Although it seems that the resonance effect is not that obvious, the experimental data clearly show the presence of an intra-bandgap state at the surface of α-$SnWO_4$, which is enhanced with the presence of SnO_2. At this point, the modulated SPV measurements in the beginning of this chapter are recalled. In Figure 4.2 a SPV signal could be observed from below the band gap, which increases with increasing NiO_x thickness. The presence and the relatively low intensity of sub-bandgap signals in the SPV coincide well with the intra-bandgap features seen in the valence band spectra. Since it is known from the previous chapter that an interfacial oxide layer (SnO_2) is formed between NiO_x and α-$SnWO_4$, these two observations are attributed to the same origin.

As mentioned in the beginning of this subchapter, ResPES was also performed on α-$SnWO_4$/NiO_x samples, where NiO_x thicknesses of 5 and 20 nm were used. In the same way as for the other samples, first the XAS spectra were measured and as mentioned above clear differences are not observable in comparison to the other samples without NiO_x layer. Subsequently, the valence band spectra were recorded under resonant condition. The recorded spectra in resonance with the Sn L_3-edge are shown in Figure B9. Valence band states of p-type NiO_x overlap with the valence band maximum of α-$SnWO_4$ and conceal the possible presence of gap states. For valence band spectra measured in resonance with the W-edge the observation is the same.

After clarifying the presence of the state in the band gap, the remaining questions are related to the origin of this state, and the implications for the performance of α-$SnWO_4$ with respect to the analysis in Chapter 3. On the basis of DFT calculations in the previous chapter the probability for the presence of gap states was discussed. In this discussion, however, only defects present in α-$SnWO_4$ were considered as the origin for defect states in the band gap. Based on several arguments this was discarded for the favor of the proposed interfacial SnO_2 layer. Although the presence of the interfacial oxide layer at the interface of α-$SnWO_4$ and NiO_x was revealed, the implications were discussed on a rather phenomenological level. With the new results in this chapter it seems, however, more likely that the defect state is introduced by the formation of the oxide layer on the surface. This may occur in a similar way either by (photo)electrochemical

oxidation in the present chapter or by interfacial oxidation upon deposition of NiO_x. Rather than being of high quality in terms of electronic defects, it seems likely that the introduced oxide layer has a high defect density. Several experimental and theoretical studies have investigated the defect structure of SnO_2,[195-200] which is in some studies referred to SnO_x due to oxygen deficiency. The presence of intra-band states is reported for SnO_x. As the origin for these defect states, the non-stoichiometry due to oxygen vacancies is suggested in some reports.[195-196] Similar mechanisms may be responsible for the gap state in the present study.

Finally, based on the analysis in the present chapter, a more detailed description of the α-$SnWO_4$ interface limitation can be proposed. The Fermi level pinning may be related to the interface of a defective oxide layer at the surface of α-$SnWO_4$ with the NiO_x layer. As described in Chapter 1.5, such a Fermi level pinning can be responsible for the reduction of the photovoltage. A schematic band diagram of an idealized α-$SnWO_4$ films is shown in Figure 4.8a for the HAXPES measurement conditions (vacuum). In this representation, is assumed that no defects or overlayers are present at the surface to illustrate the impact below more clearly. Deposition of NiO_x results in the introduction of band bending with a space charge layer width *W*, as shown in Figure 4.8b. This is accompanied by the formation of a defective SnO_x layer and the introduction of an intra-band state. In order to understand the photovoltage limitation, the PEC measurement condition needs to be illustrated. Below, the band diagrams for both cases are suggested, when the samples are in contact with the electrolyte in the dark. In the idealized α-$SnWO_4$ film, a space charge layer is introduced, which has a width W_I. More details of the origin of this band bending are provided in Chapter 1.2. The schematic band diagram of the NiO_x-coated sample, in contact with the electrolyte, is shown in panel (d). Additional band banding is not introduced in this illustration, due to the Fermi level pinning. Finally, the impact of illumination is illustrated for both cases, i.e., ideal and NiO_x-coated α-$SnWO_4$ samples. For the idealized sample, the bands are flattening under illumination, as shown in Figure 4.8e. The quasi Fermi levels of the electrons ($E_{qF,n}$) and holes ($E_{qF,h}$) split up. The splitting of the quasi Fermi levels determines the ΔOCP that can be measured in PEC. However, Fermi level pinning at the interface, limits the system's ability to reduce the band bending under illumination in open circuit conditions (see Figure 4.8f). The splitting of the quasi Fermi levels and, consequently, the ΔOCP is reduced in comparison to the ideal α-$SnWO_4$ surface without defect state. Overall, the illustrated Fermi level pinning at the intra-band defect state can provide a more fundamental explanation of the observed limitation of the photovoltage in Figure 3.1.

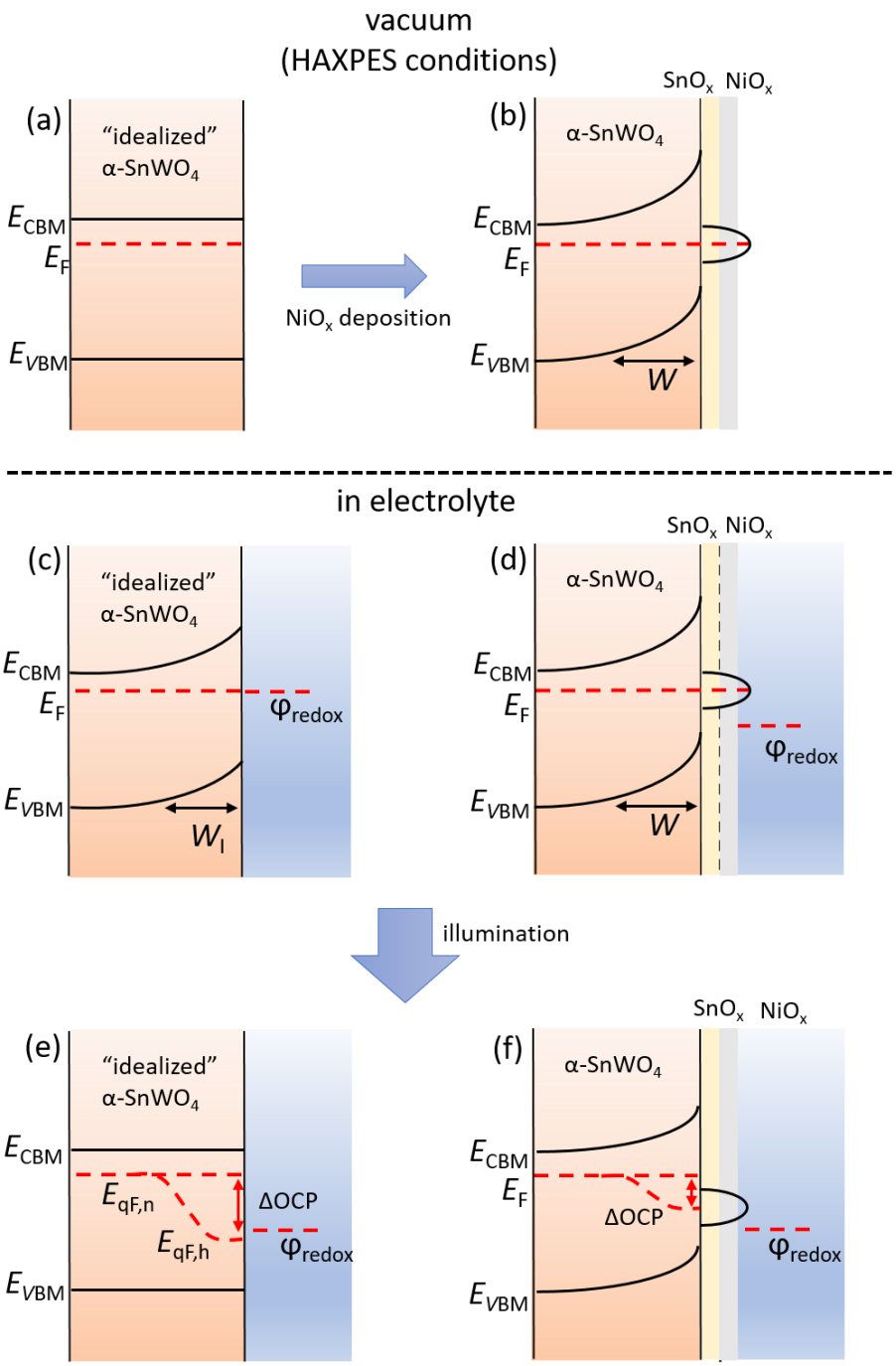

Figure 4.8. (a) Schematic band diagram of an idealized α-$SnWO_4$ film without surface defects under vacuum conditions. (b) Introduction of band bending (space charge layer width W) by deposition of NiO_x. This is accompanied by the formation of SnO_x and introduction of an intra-band defect state. (c) Idealized α-$SnWO_4$ in contact with electrolyte. A space charge layer having a width W_I is introduced. (d) In the NiO_x-covered sample no additional band bending is introduced in contact with the electrolyte, due to the Fermi level pinning at the defect state. (e) Under illumination the bands become flat. The quasi Fermi levels of electrons ($E_{qF,n}$) and holes ($E_{qF,h}$) split up, giving rise to the ΔOCP. (f) The Fermi level pinning limits the flattening of the bands, and reduces the splitting of the quasi Fermi levels. Consequently, the ΔOCP is reduced. Note that the band diagrams are shown in a simplified way to better illustrate the effect of the Fermi level pinning.

4.5. Summary and conclusion

In this chapter, the previous interface analysis of α-$SnWO_4$ films was extended using surface photovoltage analysis, XAS and HAXPES. Modulated SPV analysis suggested that a substantial part of generated charge carriers in α-$SnWO_4$ relax via trapping related processes. Clear modification of the signal could be observed upon deposition of NiO_x with different thicknesses. Especially for the SPV signal below the band gap energy, the nature of charge recombination seems to be influenced significantly. This suggests that together with the interfacial oxide layer proposed in Chapter 3, the NiO_x deposition results in substantial modification of the electronic situation at the interface. In the next step, the interface between α-$SnWO_4$ and SnO_2 was investigated, which represents one side of the proposed interfacial layer structure (α-$SnWO_4$/SnO_2/NiO_x). As expected, depth dependent increase of the Sn^{4+} contribution could clearly be observed. Finally, XAS and HAXPES were combined with the aim for resonant enhancement of element-specific features, to investigate the valence band spectra of pristine and SnO_2-coated α-$SnWO_4$ samples. Presence of a state above the valence band maximum was indicated by valence band spectroscopy. The origin of this state may be related to the introduction of the interfacial oxide layer, which is thought to have a high defect density. Combination of the defective interfacial layer with the NiO_x overlayer may result in a Fermi level pining at the interface, which may explain the limited photovoltage in α-$SnWO_4$/NiO_x structures. This suggestion extends the understanding of the interface of α-$SnWO_4$ and NiO_x presented in the previous chapter. Thereby it emphasizes the importance of finding suitable alternatives to prevent the oxide layer and interfacial defect formation, to utilize the full potential of α-$SnWO_4$ photoelectrodes. General importance of suitable interface engineering for metal oxide semiconductor is thereby emphasized as well.

5. pH-dependent stability of α-$SnWO_4$ photoanodes

Parts of this chapter are included in the following publication:

Patrick Schnell, J. Mark C. M. Dela Cruz, Moritz Kölbach, Roel van de Krol and Fatwa F. Abdi

In preparation

5.1. Introduction

The long-term (photo)electrochemical stability of photoelectrodes in aqueous electrolyte is one of the most important properties among the various requirements for photoabsorber materials.[19, 50] Especially for practical solar water splitting devices, this crucially determines the suitability of a specific semiconductor.[27, 52] A theoretical prediction of the materials stability based on thermodynamics can be done with Gerischer's stability criteria.[127, 201] In addition to these thermodynamic considerations, also kinetic aspects have an influence on the stability. Here, the ratio between the charges consumed by the self-oxidation/reduction reaction and charges consumed by the OER or HER determine the overall stability of photoelectrodes.[132] More details on the stability of photoelectrodes can be found in Chapter 1.6. Several approaches have been reported to stabilize photoelectrode materials, which includes the deposition of protection overlayers,[89, 202-203] co-catalysts,[99, 103] and tuning of the electrolyte composition.[204] In order to choose an appropriate protection strategy, understanding of the origin of the instability is in general of great importance.

Among the different types of photoelectrode materials that have been investigated for water splitting applications, metal oxides are often considered as stable in aqueous solution, especially in comparison to Si or III-V semiconductors.[46, 125] However, metal oxides can also suffer from corrosion, and only a few studies have demonstrated long-term stability above 1000 h.[85, 205] In order to become economically viable, practical devices would need to be operated for at least several years.[42, 45] In general, a large amount of studies refer to the stability of photoelectrodes, for instance, reports on extensively studied materials such as $BiVO_4$,[147, 204, 206] $CuBi_2O_4$,[160, 207-208] or Fe_2O_3.[209-210] For α-$SnWO_4$ films, systematic studies of the stability as a function of varying PEC conditions are not available thus far. It has been observed, however, that in neutral pH conditions the PEC performance of α-$SnWO_4$ quickly deteriorates. Formation of an SnO_2 surface layer, which blocks the photocurrent, has been suggested to be the origin of this behavior. The observed interfacial oxide layer in Chapter 3 and 4 also suggests a high sensitivity for surface oxidation.[90] An additional factor that needs to be considered has been revealed by the HAXPES

analysis in Chapter 3. The NiO_x deposition, which has been shown to extend the PEC stability to at least 30 min,[90] does not result in a conformal layer. It rather exhibits island formation, which means that certain areas of the α-$SnWO_4$ surface remain uncovered. This is generally not a desired growth mode for a protection layer. Previously it has been suggested that the surface layer formation may be self-limiting.[90] The exposed area of α-$SnWO_4$ would then be self-passivated by SnO_2 under the PEC conditions and further corrosion prohibited. This would relax the requirements for the protection layer deposition. However, this mechanism has not been fully proven yet, and it is not clear under which PEC conditions the self-passivation mechanism is operational. The presence of a self-terminating surface layer is, in general, an interesting feature for metal oxide photoelectrodes, as the presence of pinholes in a protection layer is often hard to prevent. Complete device failure could then be prevented by application of self-passivating materials.

In the present chapter, the (photo)electrochemical stability α-$SnWO_4$ photoelectrodes was investigated in a broad range of pH values from acidic to alkaline conditions (pH 2 – 13). Inductively coupled plasma - optical emission spectroscopy (ICP-OES) was complemented with X-ray photoelectron spectroscopy (XPS), X-ray diffraction (XRD), and in-situ spectro(photo)electrochemistry. With this approach the stability window of α-$SnWO_4$ films is defined. The experimentally obtained data are compared with a calculated Pourbaix diagram. In the last step, the proposed formation of a thin passivating oxide layer on the surface of α-$SnWO_4$ is confirmed.

5.2. pH-dependent stability of α-$SnWO_4$

First, the stability of α-$SnWO_4$ films is investigated in dependence on the pH of the electrolyte. As in the previous chapters, phase-pure α-$SnWO_4$ films with a thickness of ~100 nm were deposited by PLD. Under simulated AM1.5 illumination, a potential of 1.23 V vs. RHE was applied for a total of 1 h. Afterwards the electrolyte was investigated by ICP-OES to evaluate the possible presence of corrosion products. Details on the procedure and the electrolytes can be found in Chapter 2. In Figure 5.1 the concentration of W and Sn in the electrolyte is shown as a function of the H^+ concentration, i.e., the pH of the electrolyte shown on the top x-axis. The stability clearly depends on the pH of the electrolyte, and a stability window can be defined in the blue shaded region from pH 2 - 7. In this range, the concentration of W and Sn in the electrolyte is smaller than 1 μM. Significant corrosion and, therefore, instability is found in alkaline conditions. After PEC measurement in pH 13, W and Sn concentrations of ~22 μM are found in the electrolyte.

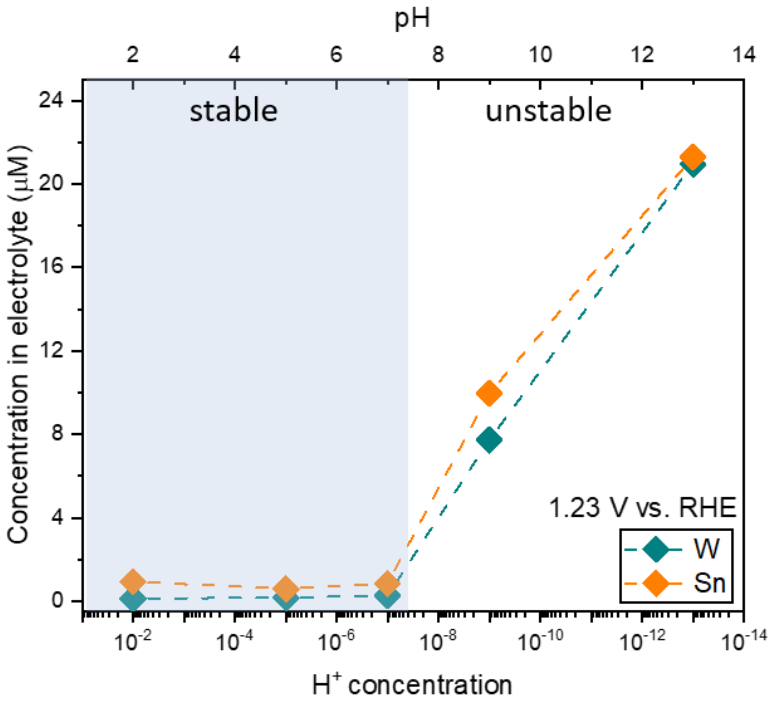

Figure 5.1. Photoelectrochemical stability of α-$SnWO_4$ films as function of the H^+ concentration in the electrolyte (i.e., the pH value which is shown on the top x-axis). Photoelectrochemical measurements of the α-$SnWO_4$ films were performed for 1 h with an applied potential of 1.23 V vs. RHE. Details of the used electrolytes can be found in Chapter 2.4. After the PEC measurements, the presence of corrosion products (i.e., W and Sn) in the electrolyte was evaluated by ICP - OES. The blue shaded area indicates the range, in which relative stability is observed (pH 2 – 7). Instability (i.e., strong dissolution) is observed in alkaline pH.

Lab-based XPS (photon energy λ = 1486.74 eV) was used in the next step to study the impact of the PEC measurements on the surface oxidation states of α-$SnWO_4$. The W 4f and Sn 3d core level spectra of a pristine α-$SnWO_4$ sample are shown in Figure 5.2a and (b). The contribution of different oxidation states was de-convoluted by peak fitting, as described in more detail in Chapter 2.3.1. In addition to the nominally expected W^{6+} state, also a smaller W^{5+} contribution can be observed. This reduced species has a contribution of 20 ± 3 % and was observed in the previous chapters in a similar amount. It was found to have no significant impact on the PEC performance compared to samples without this contribution in previous reports.[90-91] The Sn 3d core level can be de-convoluted into the Sn^{2+} state, as nominally expected in α-$SnWO_4$, and the oxidized Sn^{4+} state. A Sn^{4+} contribution of 22 ± 4 % was estimated from the peak fitting, which is of similar magnitude as in the previous chapters and in the literature.[90] In Figure 5.2c and (d) the relative contributions of W 4f and Sn 3d of the α-$SnWO_4$ samples after PEC measurement are shown as a function of the pH of the electrolyte. These are compared with the values of the pristine α-$SnWO_4$ film (dashed horizontal lines). The fitted spectra can be found in Figure C1. Although the W^{5+} contributions are varying, a systematic impact of the PEC measurements in

different pH values is not observed. The situation is different for the Sn^{4+} contribution, where a significant increase is be observed after the PEC measurement, independent on the pH conditions. At first glance, this suggests that the impact on the Sn^{4+} contribution does not depend on pH, although the origin for the increase is probably different for the different pH regimes. In strong alkaline pH, the strong dissolution observed in Figure 5.1 exposes the FTO (i.e., F-doped SnO_2) substrates and, thus, may be responsible for the increase of the Sn^{4+} contribution. This is supported by the XRD analysis shown in Figure 5.3. The measurements were performed on the samples after they were exposed to the PEC measurements. For comparison, the diffractogram of a pristine α-$SnWO_4$ film was recorded as well. When comparing the ratios of the α-$SnWO_4$ peaks with the FTO peaks, it is clear that the α-$SnWO_4$ intensity decreases in alkaline pH due to exposure of the FTO substrate. The photographs of the samples shown in Figure C2 indicate the film dissolution and the exposure of the substrate in pH 13, which is consistent with the explanation of the Sn^{4+} increase in alkaline pH. In acidic and neutral pH, the Sn^{4+} increase is not related to exposure of the FTO substrate. This is indicated by the absence of strong dissolution in Figure 5.1, and supported by the XRD measurements and the photographs of the samples, where exposure of the substrate is not observed. Instead, the increase of Sn^{4+} is attributed to secondary phase formation (i.e., SnO_2) at the surface according to the reaction equation 5.1, which has been suggested in earlier reports.[90, 92]

$$\alpha - SnWO_4 + H_2O + 2h^+ \rightarrow SnO_2 + WO_3 + 2H^+ \quad (5.1)$$

In this reaction, the formation of WO_3 is suggested as well. This is, however, difficult to verify unambiguously with the available data. Observation of the secondary phase formation in XRD is not expected, due to the expected small thickness of the WO_3 layer, and the possibly amorphous structure. Indeed, secondary phase formation after PEC treatment is not observed in Figure 5.3, independent of the pH of the solution. W in WO_3 has the same oxidation state as in α-$SnWO_4$ and is, therefore, also difficult to verify with XPS. However, clear broadening of the W $4f_{5/2}$ peak after PEC treatment may indicate the presence of WO_3, due to slightly differing binding energies of W^{6+} in WO_3 and α-$SnWO_4$ (see Figure C3). It is noted that the presence of the W peak in Figure C1 suggests that a few nm of α-$SnWO_4$ remain on the surface of the FTO substrate after measurement in pH 13, despite the optical transparency in the photograph in Figure C2.

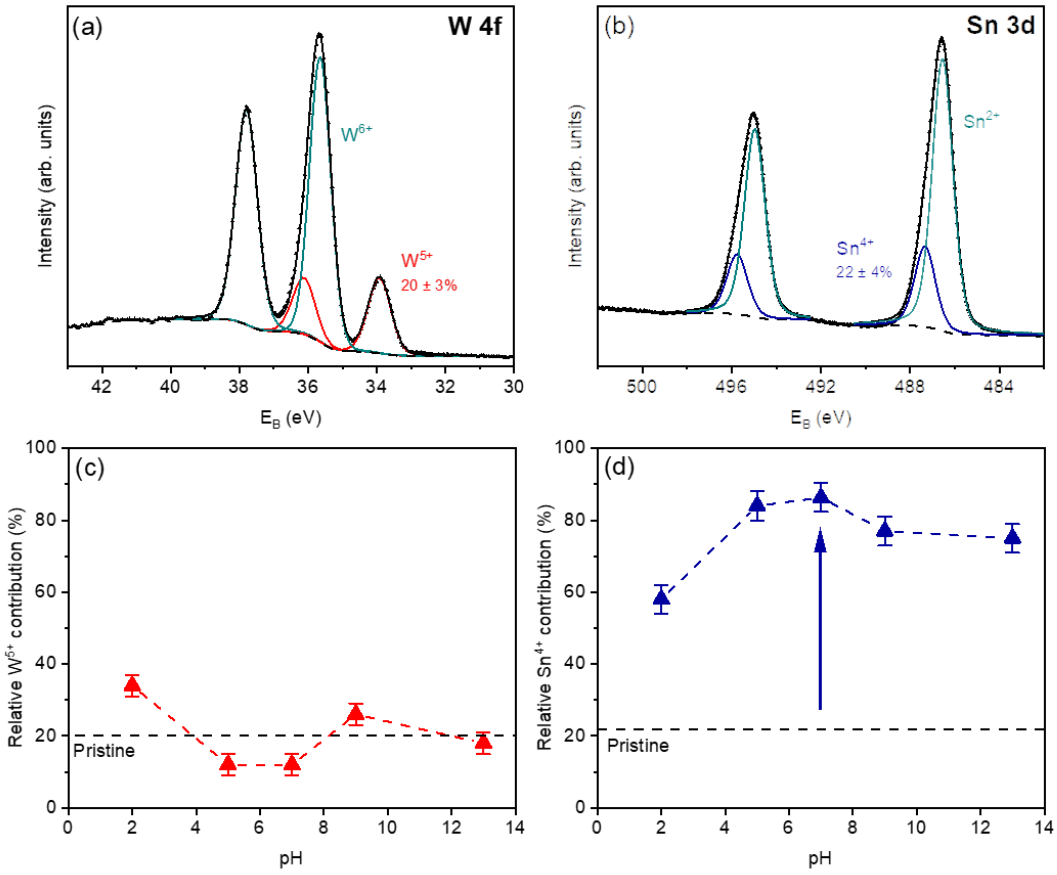

Figure 5.2. (a) De-convoluted W 4f spectrum of a pristine α-$SnWO_4$ film measured by lab-based XPS (λ = 1486.74 eV). The W^{6+} contribution can be seen as expected in nominal α-$SnWO_4$ as well as a reduced W^{5+} species. (b) Sn 3d core level spectrum of the pristine α-$SnWO_4$ film. The main contribution is attributed to Sn^{2+} and a smaller contribution of Sn^{4+} is found. (c) Relative W^{5+} contribution after PEC measurements in various pH electrolytes for the samples investigated in Figure 5.1, in comparison to the pristine α-$SnWO_4$ sample. XPS measurements were only performed on the area exposed to the PEC measurements. (d) Significant increase of the Sn^{4+} contribution after PEC treatment in different pH electrolytes.

Finally, the observed stability in acidic to neutral pH in Figure 5.1 may be explained by the stability of the formed surface layers (i.e., SnO_2 and WO_3) in this pH regime. WO_3 is known to be stable in acidic to semi-acidic pH conditions.[211-213] SnO_2 is expected to be stable in acidic to neutral pH conditions and even in alkaline conditions at pH 9.[179, 214] Both surface layers are unstable in strong alkaline pH (pH > 13). Consequently, the observed stability of α-$SnWO_4$ in acidic to neutral pH can be explained by the formation of the surface oxide layers. The dissolution of α-$SnWO_4$ in pH 9 may be related to the known instability of WO_3. The dissolution of WO_3 may weaken the structural integrity of α-$SnWO_4$, and cause the entire film to dissolve.

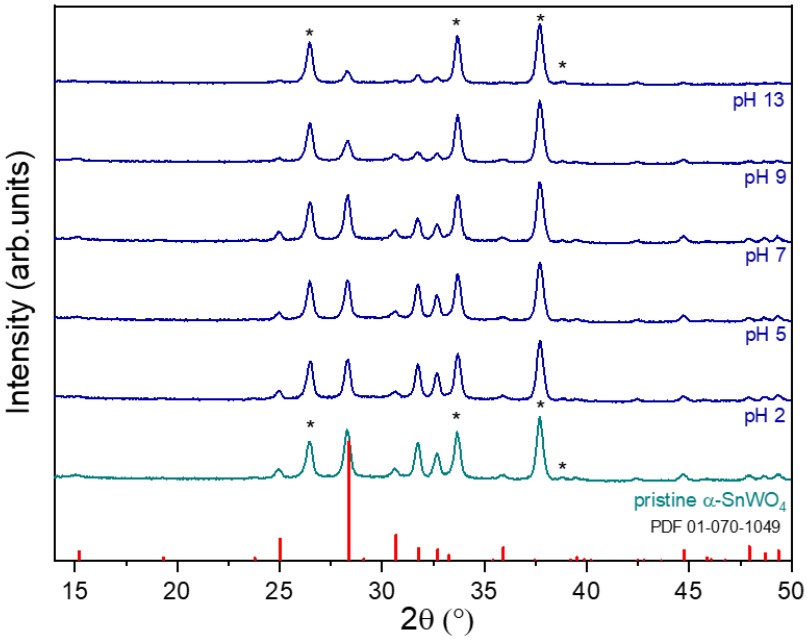

Figure 5.3. XRD analysis of a pristine α-$SnWO_4$ film and samples treated in different pH electrolytes. Measurement was performed at 1.23 V vs. RHE for a total of 1 h. The FTO reflections are indicated by asterisks. The reference pattern for α-$SnWO_4$ is shown in red and was taken from JCPDS 01-070-1049. Formation of additional phases is not observed after the PEC measurements. The intensity ratio of α-$SnWO_4$/FTO decreases in alkaline pH and indicates the exposure of the FTO (i.e., F-doped SnO_2) substrate due to dissolution of the α-$SnWO_4$ film.

5.3. Potential-dependent stability of α-$SnWO_4$

After clarifying the influence of the pH conditions at a fixed applied potential, in the next step, the potential-dependent stability of α-$SnWO_4$ is evaluated. ICP-OES was again measured on the electrolyte solutions after the PEC measurements in a potential range between 0.6 V and 1.23 V vs. RHE. The lower limit is the minimum operating voltage typically required in a tandem configuration with a Si bottom absorber. First, the behavior in pH 13 is investigated, and it is evaluated whether the application of less-positive potentials can prevent or reduce degradation. In Figure 5.4a and (b) the Sn and W concentrations in the electrolyte are shown, which were measured after several time steps at various applied potentials. A potential dependence is observed within the first 15 min, where a smaller dissolution of Sn and W is observed for less-positive potentials. Afterwards the concentration in the electrolyte saturates for both elements and the potential dependence disappears. This saturation probably corresponds to the almost complete dissolution of the film, expect a few nm of α-$SnWO_4$ that remain on the surface as suggested by XPS. Overall, degradation of α-$SnWO_4$ also occurs at less-

positive potentials, and the initially slower dissolution does not prevent it from happening after a longer time. Thus, alkaline pH conditions (pH 13) are not suitable for the operation of α-$SnWO_4$ photoanodes.

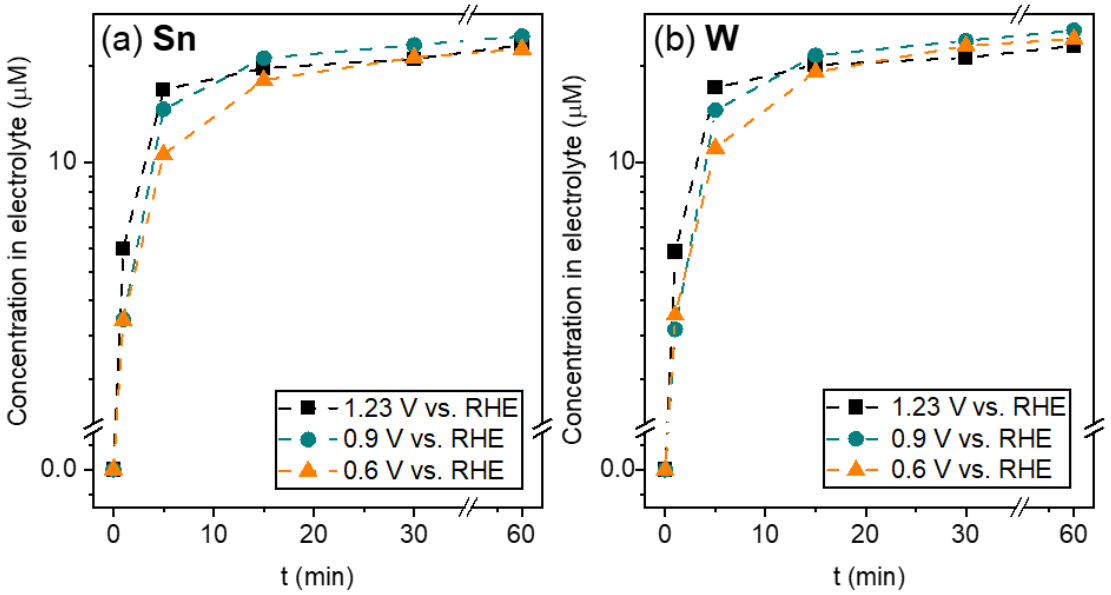

Figure 5.4. Degradation of α-$SnWO_4$ films in pH 13 (0.1 M KOH) as a function of the applied potential. Corrosion products in the electrolyte were evaluated by ICP-OES after several time steps. (a) The Sn concentration significantly increases within the first 15 min. Afterwards it saturates and the degradation process stops due to the almost complete dissolution of the film. In the initial stage a potential dependence is observed, where slower dissolution is found for less-positive potentials compared to 1.23 V vs. RHE. (b) The W concentration in the electrolyte follows the same trend as the Sn concentration. This shows that α-$SnWO_4$ films are also not stable at less-positive potentials in pH 13 electrolyte.

In acidic to neutral pH conditions the potential dependence was explored as well by performing PEC measurements with various applied potentials. ICP-OES measurements shown in Figure C4a could not reveal a systematic trend. A possible potential dependence, however, may not be visible, due to the sensitivity of the ICP-OES measurements. The element concentrations in acidic to neutral pH are close to the detection limit. In the XPS measurements in Figure C4b a potential dependence of the Sn^{4+} contribution at the surface can be found. The Sn^{4+} contribution decreases when less-positive potentials are applied. Overall, in acidic and neutral pH electrolyte α-$SnWO_4$ films exhibit relatively good stability. The dissolution of the surface, however, due to the formation of binary surface oxide layers, cannot be completely prevented by applying less-positive potentials.

5.4. Stability investigation by spectro(photo)electrochemistry

Stability investigation of α-$SnWO_4$ films was also performed by in-situ spectro(photo)electrochemistry experiments. During the PEC measurement for 1 h with an applied potential of 1.23 V vs. RHE, the change in transmission was monitored to investigate the stability of the samples. A white light source was used to monitor the change in the transmitted light intensity, which was recorded with a spectrometer. Charge carrier generation in the films was induced by illumination with a UV-LED (λ = 365 nm). More details on the setup can be found in Chapter 2.5. In Figure 5.5 the change in transmission expressed as ΔOD is presented for λ > 400 nm. A clear increase in the transmission (i.e., a decrease of ΔOD) can be observed for pH 13 in Figure 5.5a, which confirms the instability in this pH regime. For a probe wavelength of λ = 450 nm the change in ΔOD is shown in (d) as a function of time. Within the first few minutes (~15 min), the largest change in ΔOD and, therefore, degradation can be observed. Afterwards, the change is smaller and the ΔOD saturates, when the film is almost completely dissolved. Overall, good agreement can be found with the ICP-OES measurements presented in Figure 5.4, where the same trend could be observed in alkaline electrolyte.

In Figure 5.5b and (c) the contour plots for the measurements in acidic (pH 2) and neutral (pH 7) are presented. Relative stability is observed due the absence of significant changes in ΔOD. The trend observed for λ = 450 nm in (d) supports the suggestion of the formation of the surface layer. After a small initial drop in ΔOD, as seen in more detail in the inset, further significant changes cannot be observed. This suggests a self-limiting nature of the surface layer formation.

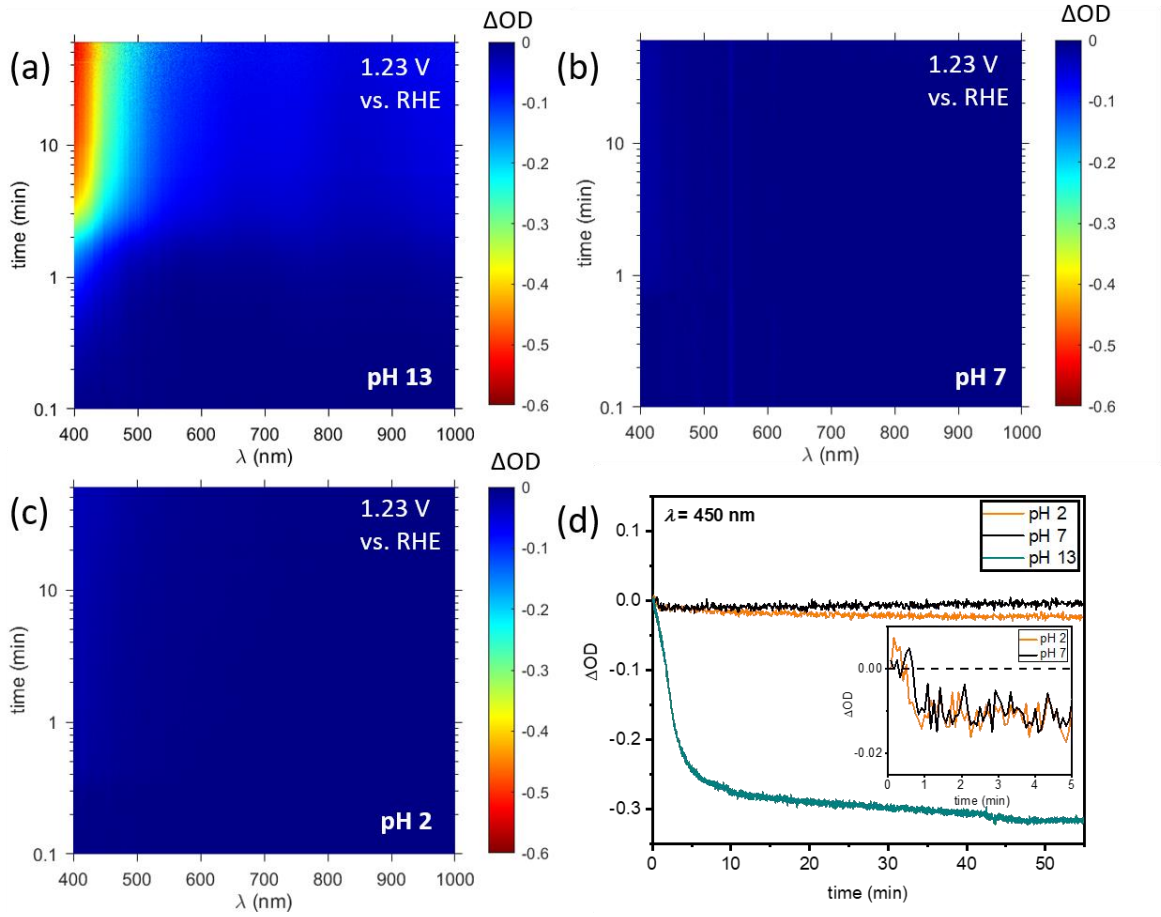

Figure 5.5. In-situ stability investigation of α-SnWO4 films by spectro(photo)electrochemistry measurements. α-SnWO4 samples were mounted in a PEC cell and a potential of 1.23 V vs. RHE was applied for 1 h. Charge carriers were generated by irradiation with a UV-LED (λ = 365 nm). The change in transmission was monitored with a separated white light source in combination with a spectrometer (see Chapter 2.5 for more details). (a) shows the behavior in pH 13, where strong dissolution can be observed. In (b) and (c) relative stability is observed for pH 2 and 7. (d) Comparison of the change in transmission at λ = 450 nm for the different pH conditions, which emphasizes that the change in transmission mainly happens within the first few minutes. The small initial changes for pH 2 and 7 can be seen more clearly in the inset.

The influence of less-positive applied potentials during the PEC treatment was also investigated with the same approach. In Figure 5.6 the measurements are presented, which were performed at 0.6 V vs. RHE in pH 2 and 7. When comparing the contour plots in (a) and (b) with the previous measurements at higher potential in Figure 5.5, clear differences cannot be found at first glance. However, comparing the change in ΔOD for λ = 450 nm in panel (c) and (d), reveals the higher sensitivity of the spectro(photo)electrochemistry measurements in comparison to the ICP-OES measurements. A smaller change in ΔOD is observed for lower potentials, which also correlates with the XPS measurements shown in Figure C4b, where less surface oxidation (Sn^{4+}) was observed for less-positive potentials. Such a clear trend could not be observed by ICP-OES, as discussed above, due to the detection limit.

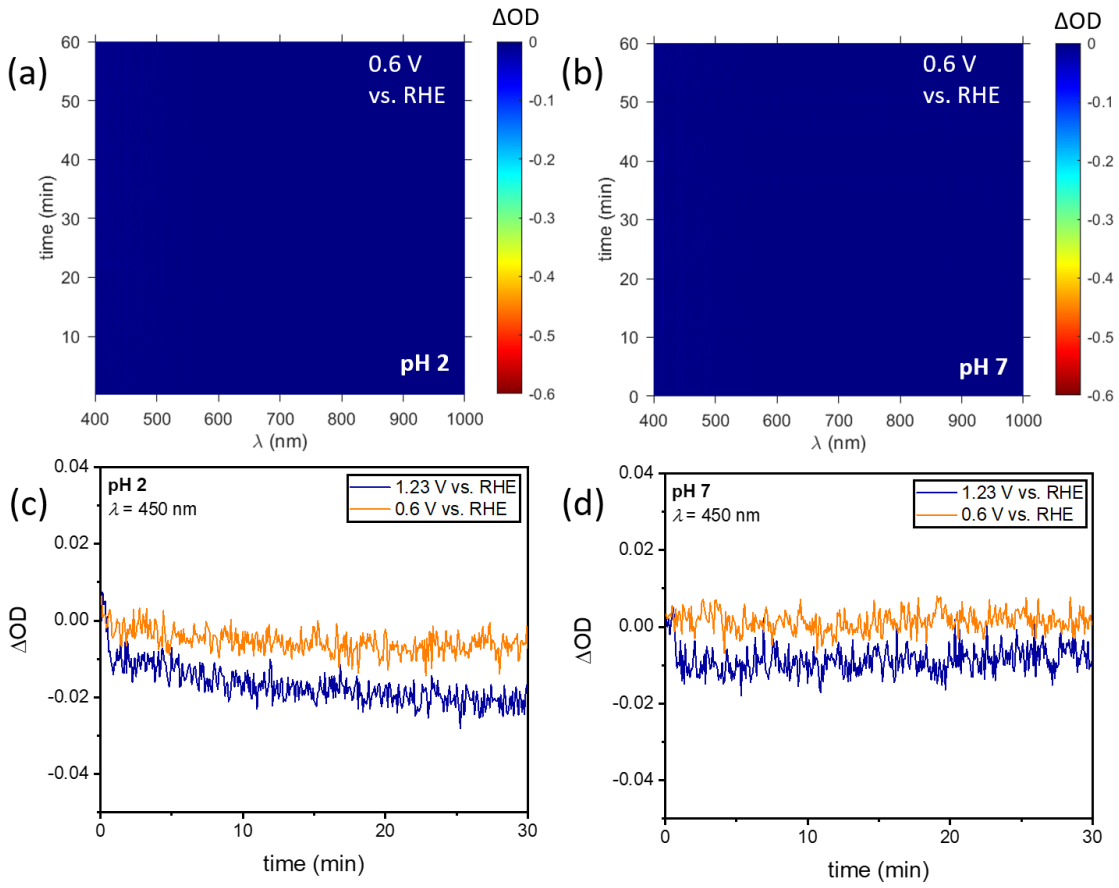

Figure 5.6. Spectro(photo)electrochemistry measurements of α-$SnWO_4$ films performed at less-positive potentials. The change in transmission is expressed as ΔOD. (a) and (b) show the measurements performed at 0.6 V vs. RHE for 1 h in pH 2 and pH 7, where stability can be observed by the absence of a significant change in transmission. In (c) and (d) the measurements performed at 0.6 V vs. RHE are compared with the measurements performed at 1.23 V vs. RHE (see Figure 5.5) for λ = 450 nm. A smaller drop in ΔOD can be observed for less-positive potentials.

5.5. Comparison of the experimental results with the calculated Pourbaix diagram

In the next step, the experimental results obtained by ICP-OES are compared with a theoretical Pourbaix diagram,[179, 214] which is provided by the Materials Project.[4] In general, a Pourbaix diagram provides information about the thermodynamic stability of a material system, which depends on the pH of the aqueous solution, and the electrochemical potentials of all species present in the solution.[129] Pourbaix diagrams can be constructed experimentally. However, this may be challenging and especially for rather new materials this may not be available. Theoretical calculations of Pourbaix diagrams, therefore, offer a convenient approach to predict the stability of a material, although these may not be fully accurate and other factors beyond the

[4] The Materials Project is an open database that aims to provide the properties of inorganic materials via computational approaches.

thermodynamic stability may play a role. In the Materials Project the calculation is based on free energies of aqueous ions taken form experimental reports and free energies of the solid phases calculated by DFT.[214]

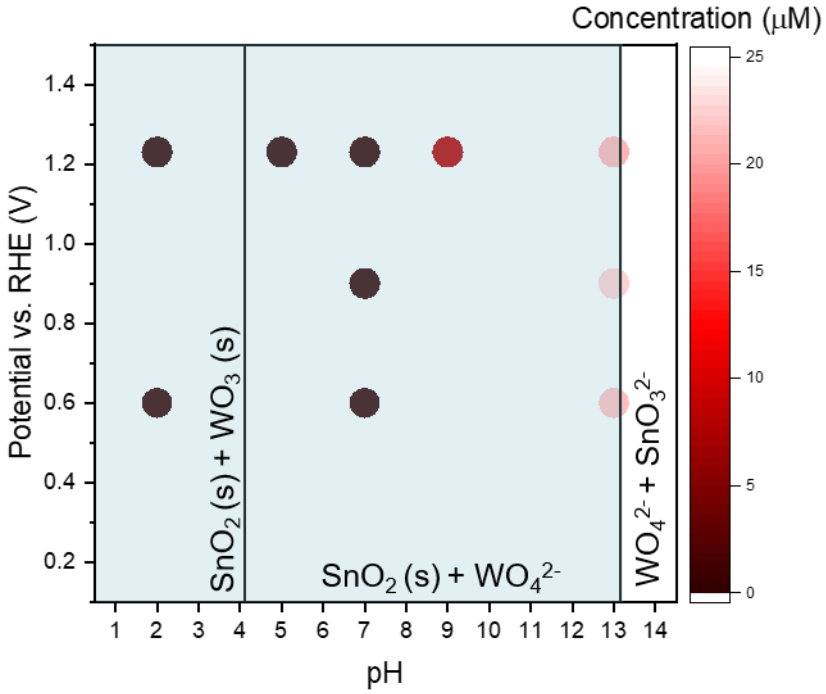

Figure 5.7. Summary of the experimentally observed stability and degradation of α-$SnWO_4$ films measured by ICP-OES and comparison with a modified theoretical Pourbaix diagram provided by the Materials Project.[179, 214] The diagram is calculated for W and Sn ion concentrations of 10^{-6} mol/kg. The phases that are expected to be stable in the respective pH regimes are indicated. In the blue shaded region, stability of at least one solid phase is expected. In acidic to neutral pH good agreement can be observed between experiment and calculation. In alkaline pH 9 and 13 the experimental data disagree with the theoretical prediction.

In Figure 5.7 the experimentally obtained stability data are summarized and compared with the theoretical Pourbaix diagram. Based on the Pourbaix diagram, stability of at least one solid phase is predicted in a broad pH range from acidic to alkaline pH in the blue shaded range. The experimentally measured concentrations in the electrolyte after the 1 h PEC measurements are represented by color-coded points. The solid SnO_2 and WO_3 phases are predicted to be thermodynamically stable in acidic conditions (pH < 4). In this region good agreement between experiment and calculation exists. The suggestion derived from XPS that SnO_2 and WO_3 forms at the surface supports the agreement. Between pH 4.1 and 13.2 the formation of SnO_2 and WO_4^{2-} (i.e., dissolution of W) is predicted in the Pourbaix diagram. In the experiment, stability is observed in pH 5 and 7. If in this regime indeed SnO_2 and WO_3 is formed on the surface as proposed above in Chapter 5.2, this may suggest that the stability regime of SnO_2 and WO_3 is

actually larger than thermodynamically predicted. Kinetics may influence the overall stability that is experimentally observed in this regime. In pH 5 and 7, the dissolution of WO_3 and thus the formation of WO_4^{2-} may be very slow, such that a protecting SnO_2 layer can form, which inhibits further dissolution of α-$SnWO_4$. Disagreement between experiment and the thermodynamic prediction can be found in alkaline conditions. The strong dissolution of Sn *and* W in pH 9, and especially in pH 13 is not predicted by the Pourbaix diagram. Instead, the experimental observation in alkaline conditions agrees with the thermodynamic instability region above pH 13.2 in the calculation. In this region, the dissolution of Sn and W is predicted by formation of SnO_3^{2-} and WO_4^{2-}. The instability region in alkaline pH is, consequently, larger than predicted.

5.6. Long-term stability and self-passivation

Finally, the long-term stability of α-$SnWO_4$ films is investigated in neutral pH conditions. In Figure 5.8 the element concentrations in the electrolyte are shown, measured by ICP-OES after PEC measurements for 1 h and 24 h. The measurements were performed in pH 7 electrolyte with an applied potential of 1.23 V vs. RHE. After 24 h both the Sn and W concentrations are of similar magnitude as observed after 1 h, indicating that within this time period further dissolution does not occur. For comparison the element concentrations after 1 h measurement in pH 13 is indicated, where strong dissolution is found. The observations in the ICP-OES data are complemented with the XPS measurements presented in panel (b). After 1 h and 24 h a significant increase of the Sn^{4+} contribution at the surface can be seen. In both cases the relative contributions are very similar, which indicates that further oxidation (i.e., further growth of the oxide layer) does not occur. This suggests the self-limiting nature of this passivating oxide layer in pH 7 electrolyte formed at the surface of α-$SnWO_4$.

Although further film dissolution is prevented, the hole blocking nature of this surface layer limits charge transfer to the electrolyte. The photocurrent measured in the pristine α-$SnWO_4$ film drops within the initial stage of the PEC measurement by ~90 % as seen in Figure 5.9. To exclude kinetic limitations at the surface, in this case the measurement was performed in pH 7 electrolyte with the addition of 0.5 M Na_2SO_3 as a hole scavenger. As shown in more detail in Figure C5, the presence of the scavenger does not have a significant impact on the stability. The clear drop of the photocurrent density can be prevented by deposition of a 20 nm NiO_x overlayer, which partially prevents the oxide layer formation (see the previous chapters and reports).[90, 92] In Figure 5.9 the photocurrent of the NiO_x protected film is indeed higher and more stable.

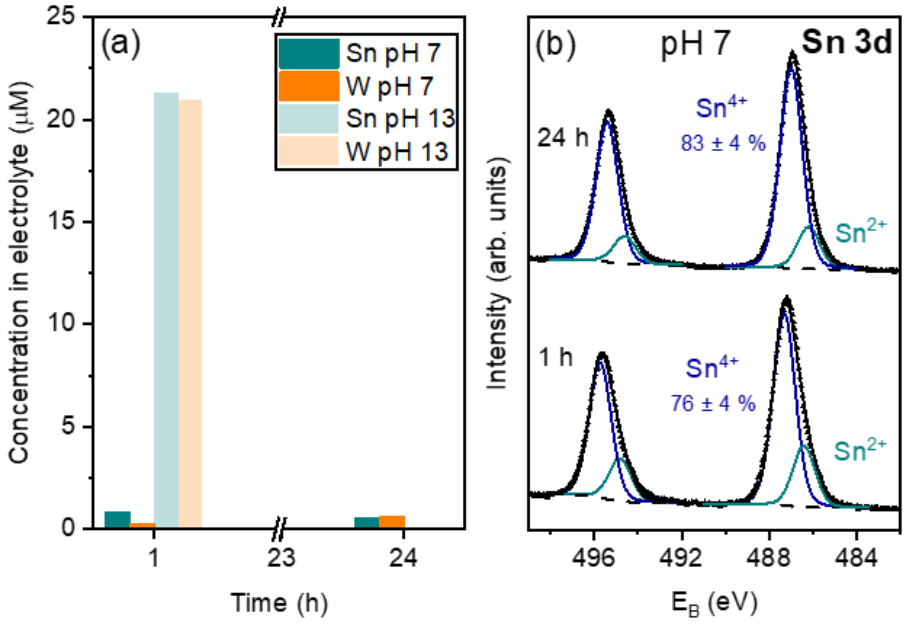

Figure 5.8. Long-term stability of α-$SnWO_4$ films. In (a) the W and Sn concentrations in the electrolyte after the measurements for 1 h and 24 h are shown, where a significant difference in the element concentrations between both measurement times cannot be observed. Further film dissolution is inhibited. This is also supported by the Sn 3d core level spectra shown in (b). There is no significant difference in the Sn^{4+} contribution between the spectra measured after the 1 h PEC measurement and the one measured after 24 h PEC exposure.

It decreases, however, continuously within the measurement period and after 24 h only ~50 % of the initial current can be measured. The origin of this decrease can be found again with the help of ICP-OES measurements. After several time steps, the electrolyte was measured by ICP-OES, and in Figure 5.9b the results are presented. The concentration of Ni increases significantly, which correlates with the decrease of the photocurrent. At the same time the concentrations of Sn and W remain relatively constant in the electrolyte. Overall, this suggest that the loss in photocurrent is related to the dissolution of the NiO_x layer and shows that the NiO_x film is not completely stable in pH 7 conditions. The stability of the NiO_x layer is, consequently, another limitation of the α-$SnWO_4$ photoelectrodes, in addition to the photovoltage limitation discussed in the previous chapters.

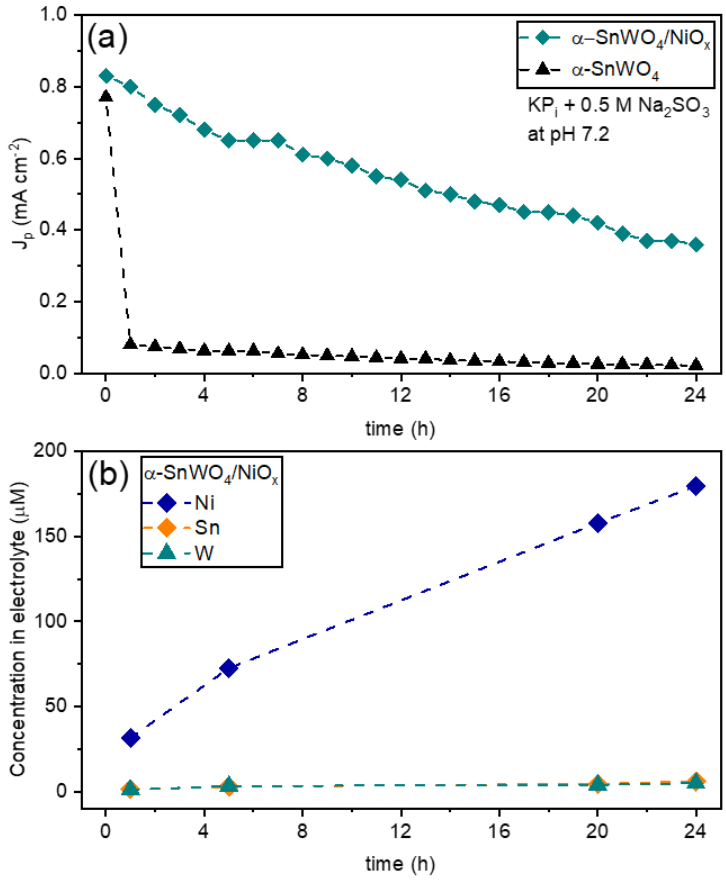

Figure 5.9. (a) Photocurrent J_p of a pristine α-$SnWO_4$ film and a film coated with 20 nm NiO_x. For the pristine film J_p decreases in the initial period of the measurement, which can be correlated with the surface oxide layer formation. The origin for the decreasing J_p of the NiO_x coated sample can be found in the ICP-OES measurements shown in (b). The NiO_x layer dissolves as indicated by the increase of the Ni concentration in the electrolyte. At the same time the W and Sn concentrations remain relatively constant.

5.7. Summary and conclusion

In this chapter, the (photo)electrochemical stability of α-$SnWO_4$ photoanodes prepared by PLD was studied in detail. A combination of the complementary techniques ICP-OES, XPS, XRD, and spectro(photo)electrochemistry was used. Thereby the dependence on the pH of the electrolyte, and the impact of the applied potential during the PEC measurement were investigated. Strong dependence on the pH conditions was found. A regime with relatively good stability could be defined from acidic to neutral (2 – 7) pH. Significant dissolution was found in alkaline electrolyte (pH > 9), which was reduced at less-positive potentials. A calculated Pourbaix diagram from the Materials Project[179, 214] was used for comparison with the experimental results. Good agreement exists in acidic to neutral pH. In alkaline conditions, however, the Pourbaix diagram underestimates the instability region. Although the dissolution

in acidic to neutral pH was limited, oxidation of Sn^{2+} to Sn^{4+} could clearly be observed. Formation of SnO_2 as well as WO_3 was also suggested. PEC measurements resulted in the formation of a surface oxide layer probably consisting of a mixture both oxides. The overall stability of α-$SnWO_4$ is defined by this surface layer, which forms within the first few minutes of the PEC treatment. Most effective protection of α-$SnWO_4$ by the surface layer was found in neutral pH conditions, which is consequently the most suitable operation condition. Long-term stability (24 h) investigations finally confirmed the self-limiting nature of the surface layer formation, which demonstrates the self-passivation of α-$SnWO_4$ photoelectrodes. The extractable photocurrent is, however, limited by the charge transfer blocking nature of the passivation layer. High photocurrents can only be achieved with the help of a hole-conducting protection layer. NiO_x is the best working solution so far, although the limited stability in pH 7 is another challenge in addition to the previously discussed photovoltage issue. The self-passivation mechanism is, however, an important feature of α-$SnWO_4$ photoelectrodes, especially for long-term operation in a water splitting device. In general, with the presence of a self-passivation mechanism the requirements for overlayer deposition are relaxed. Absence of full layer conformality, due to the presence of pinholes or an island type growth of the overlayer, will not result in complete operational breakdown.

6. Summary, conclusions and outlook

In order to mitigate the impact of climate change on environment, society, and economy, a transition to a system based on sustainable energy sources is required. Hydrogen produced via photoelectrochemical water splitting may become an important contribution in the coming decades. One of the main challenges for the success of this technology is the development of suitable semiconducting materials. These may be found in the class of metal oxide materials. An ideal candidate, however, has not been found thus far. α-$SnWO_4$ is an emerging candidate of this material class, which offers promising properties. The development of highly efficient α-$SnWO_4$ photoelectrodes is however challenging. Therefore, in the present thesis, major challenges of this material were addressed, with a focus on the understanding of the underlying mechanisms.

In the first part, the photovoltage limitation in α-$SnWO_4$ films coated with NiO_x overlayers was investigated. Open circuit potential analysis was used to confirm the limitation. A relation of the photovoltage reduction with the thickness of NiO_x was found, where the ΔOCP decreased with increasing NiO_x thickness. This motivated the thorough investigation of the interface between α-$SnWO_4$ and NiO_x by hard X-ray photoelectron spectroscopy. Strong upwards band bending in α-$SnWO_4$ was observed at the interface, which may be beneficial for the separation of photogenerated charge carriers. However, an effect that negates this beneficial property seems to be present. Significant oxidation of Sn^{2+} to Sn^{4+} was found at the same time, which increased with the thickness of the NiO_x layer. Density functional theory calculations and Monte Carlo-based peak intensity simulation of the spectroscopy data were used to understand the impact of the interfacial oxidation. Secondary phase formation at the interface in the form of SnO_2 was proposed. This observation was correlated with the photovoltage limitation with the help of control experiments. Step-wise oxidation and, thus, SnO_2 formation was accompanied by a similar decrease in the ΔOCP as for the NiO_x coated films. A first phenomenological understanding of the α-$SnWO_4$/NiO_x interface could be generated in this chapter.

Modulated surface photovoltage spectroscopy indicated the substantial alteration of the charge separation and relaxation processes upon deposition of NiO_x on α-$SnWO_4$. First indication for the presence of intra-band defect states was found. Further photoelectron spectroscopy studies were performed to complement this analysis. A thorough analysis of the interface of α-$SnWO_4$ and SnO_2 was performed. Valence band spectroscopy revealed the presence of a state above the valence band maximum. This state may be the origin of the Fermi level pinning at the interface of surface oxidized α-$SnWO_4$ and NiO_x, as illustrated by the band diagrams.

Consequently, the photovoltage limitation in α-$SnWO_4$ may be a result of the substantial surface modification of α-$SnWO_4$. Overall, the first two chapters provided detailed understanding of the photovoltage limitation in α-$SnWO_4$/NiO_x photoelectrodes.

The final chapter in this thesis showed again the importance to understand the impact of surface modifications on the photoelectrode properties. In this case, the impact was investigated with respect to the (photo)electrochemical stability of α-$SnWO_4$ films. Inductively coupled plasma - optical emission spectroscopy was used to investigate the stability in dependence on pH and applied potential during operation. The stability clearly depends on the pH of the electrolyte, and relative stability is found in neutral to acidic pH. Potential dependence of the stability was found as well. Spectro(photo)electrochemistry was used to investigate the stability in-situ under PEC conditions. The high sensitivity of these measurements even revealed a potential dependence in pH 2 and pH 7 electrolyte, where relative stability was found. The overall stability of α-$SnWO_4$ films depends on the formation of the binary surface oxide layer (containing SnO_2 and WO_3), as suggested by the combination of the dissolution data with X-ray photoelectron spectroscopy and X-ray diffraction. Comparison with a calculated Pourbaix diagram was performed. The experimentally determined stability window agrees well with the calculation. However, the instability region in alkaline conditions was underestimated by the calculated potential-pH diagram. Long-term stability investigations performed in pH 7 electrolyte showed the self-passivation of α-$SnWO_4$ films. Further film dissolution is inhibited by this mechanism. This mechanism can be a great advantage for the long-term operation of photoelectrodes. The performance of NiO_x coated α-$SnWO_4$ films is, however, limited by the stability of NiO_x in neutral pH electrolyte. This indicated another limitation of NiO_x as a protection layer for α-$SnWO_4$. In addition to the photovoltage limitation, the stability of NiO_x is another motivation to develop alternative protection strategies for α-$SnWO_4$.

Overall, in this thesis, fundamental understanding of two important aspects of α-$SnWO_4$ photoelectrodes was achieved, i.e., the photovoltage limitation and the photoelectrochemical stability. Further fundamental understanding may also be generated with epitaxial α-$SnWO_4$ films in future studies. Pulsed laser deposition, used in the present study, is generally suitable for the deposition of such films. The basic understanding can help to find suitable strategies to enhance the performance of α-$SnWO_4$ films. In order to mitigate the discussed limitations, new protection strategies need to be developed. Here, it is essential to protect the sensitive α-$SnWO_4$ surface from oxidation. Passivation of the surface may also be achieved, for instance, with the help of self-assembling monolayers. If the discussed challenges will be solved, then α-$SnWO_4$ photoanodes are, in principle, a promising candidate for tandem

devices in combination with a Si bottom absorber. Development of such devices is crucial to achieve highly efficient photoelectrochemical water splitting.[55] While it seems realistic that significant improvements of α-$SnWO_4$ films can be achieved on a laboratory scale with elaborate protection and device concepts, the perspective of α-$SnWO_4$ to become the "ideal absorber material", should be critically assessed. A potential limitation of α-$SnWO_4$, which has not been in the focus of the present study, is the rather low absorption coefficient in the visible wavelength range.[90, 118] As already proposed previously, this may be overcome by nano-structuring to achieve higher efficiencies. [90, 118] The "ideal photoabsorber", however, should not only be efficient, but it should also be scalable, of low-cost, and easy to manufacture.[46] These typical advantages of metal oxides may be partially negated by high demands on the protection layer deposition and by the need for nanostructuring. Despite these drawbacks, it seems advisable to invest further research efforts in the development of α-$SnWO_4$-based photoelectrodes, also because of the beneficial self-passivation effect. In parallel to the development of α-$SnWO_4$ films, further efforts should be put on the screening and development of emerging metal oxide materials. Here, the general importance of the obtained results in the present study can contribute to an efficient development of other metal oxide photoelectrodes. These development efforts can help to finally establish PEC water splitting as the production route for sustainable hydrogen in the coming decades.

List of selected publications

1. **P. Schnell**, M. Kölbach, M. Schleuning, K. Obata, R. Irani, I. Y. Ahmet, M. Harb, D. E. Starr, R. van de Krol and F. F. Abdi, Interfacial oxide formation limits the photovoltage in α-$SnWO_4$/NiO_x photoanodes prepared by pulsed laser deposition, *Advanced Energy Materials* **2021,** 2003183
2. **P. Schnell,** J. M. C. M. Dela Cruz, M. Kölbach, R. van de Krol and Fatwa F. Abdi, pH-dependent stability of α-$SnWO_4$ photoelectrodes, *in preparation*
3. **P. Schnell**, Erwin Fernandez, Keisuke Obata, Jennifer Velázquez Rojas, Thomas Dittrich, Roel van de Krol and Fatwa F. Abdi, Intra-band gap states in α-$SnWO_4$ photoanodes introduced by surface modifications, *in preparation*
4. S. Zhang, I. Y. Ahmet, S. Kim, O. Kasian, A. Mingers, **P. Schnell**, M. Kölbach, J. Lim, A. Fischer, K. J. J. Mayerhofer, S. Cherevko, B. Gault, R. van de Krol and C. Scheu, Different Photostability of $BiVO_4$ in Near-pH-Neutral Electrolytes, *ACS Applied Energy Materials* **2020**, 3, 9523-9527
5. D. A Grave, D. S. Ellis, Y. Piekner, M. Kölbach, H. Dotan, A. Kay, **P. Schnell**, R. van de Krol, F. F. Abdi, D. Friedrich and A. Rothschild, Extraction of mobile charge carrier photogeneration yield spectrum of ultrathin film metal oxide photoanodes for solar water splitting**,** *Nature Materials* **2021 20**, pages 833–840
6. N. Yulianto, A. D. Refino, S. Mariana, N. Majid, A. Syring, **P. Schnell**, R. A. Wahyuono, K. Triyana, W. Daum, F. F. Abdi, T. Voss, H. S. Wasisto, A. Waag, Wafer-scale transfer route for top-down III-nitride nanowire LED arrays based on femtosecond laser lift-off technique, *Microsystems and Nanoengineering* **2021,** 7, 23
7. S. Gahlawat, I. Y. Ahmet, **P. Schnell**, I. Levine, T Dittrich, S. Zhang, P. Ingole, and F. F. Abdi, Enhancing the photon absorption and charge carrier dynamics of $BaSnO_3$ photoanodes via intrinsic and extrinsic defects, *in peer review*
8. D. S. Ellis, Y. Piekner, D. A. Grave, **P. Schnell** and A. Rothschild, Considerations for the accurate measurement of incident photon to current efficiency (IPCE) in photoelectrochemical (PEC) cells, *submitted*
9. R. Irani, K. Obata, P. Plate, S. P. Berglund, K. Harbauer, C. Höhn, I. Ahmet, **P. Schnell**, M. Kölbach, P. Bogdanoff, R. van de Krol, F. F. Abdi, the role of interfacial energetics in determining charge transfer between semiconductor photoelectrodes and co-catalyst, *in preparation*

10. S. Gahlawat, **P. Schnell,** R. Irani, I. Y. Ahmet, L. Choubrac, S. Fiechter,P. P. Ingole, F. F. Abdi, extending the absorption limit of $BiVO_4$ with anion doping for photo-electrochemical water splitting (working title), *in preparation*

A. Supplemental information for Chapter 3: interfacial oxide formation limits the photovoltage in α-$SnWO_4$/NiO_x photoanodes prepared by pulsed laser deposition

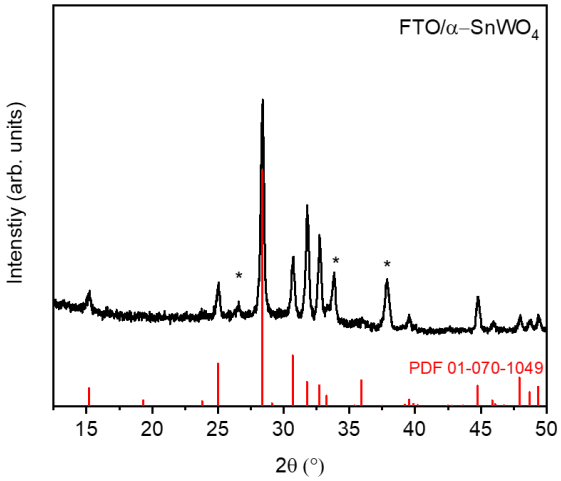

Figure A1. X-ray diffractogram of our 100 nm-thick α-$SnWO_4$ film. All reflections can be assigned to the α-phase (PDF 01-070-1049, blue vertical lines) and the underlying FTO substrate (marked with asterisks).

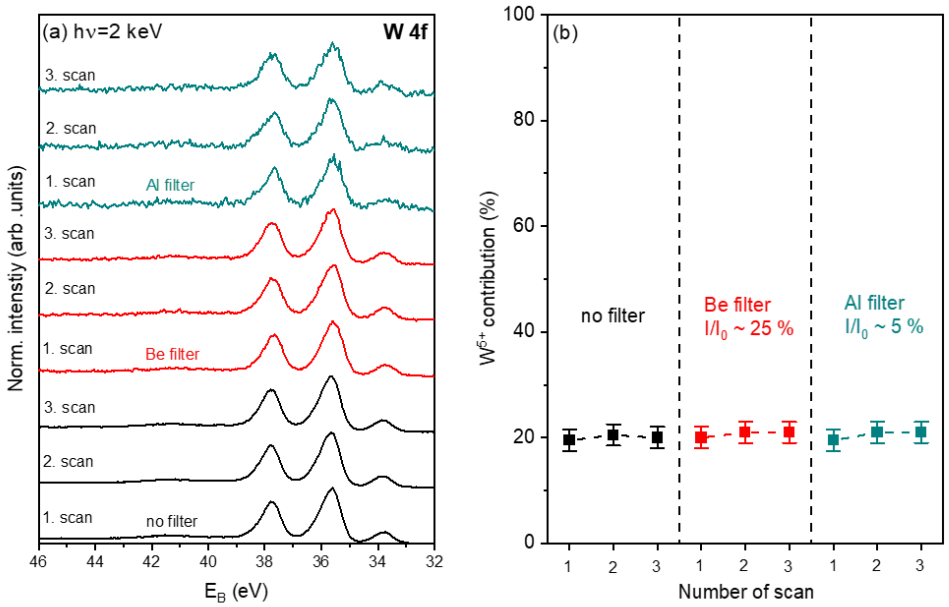

Figure A2. Beam damage study performed on pristine α-$SnWO_4$ by HAXPES. In (a) the W 4f core level spectra are shown, which were measured without filter (100 % intensity), with the use of a Be filter (~25 % intensity), and with the use of a Al filter (~5 % of the original intensity). Measurements were performed on three different and fresh measurement spots. For all measured scans the W^{5+} contribution was determined, which is shown in (b). A clear difference of the W^{5+} contribution cannot be observed, indicating that beam damage is not the origin of the W^{5+} contribution.

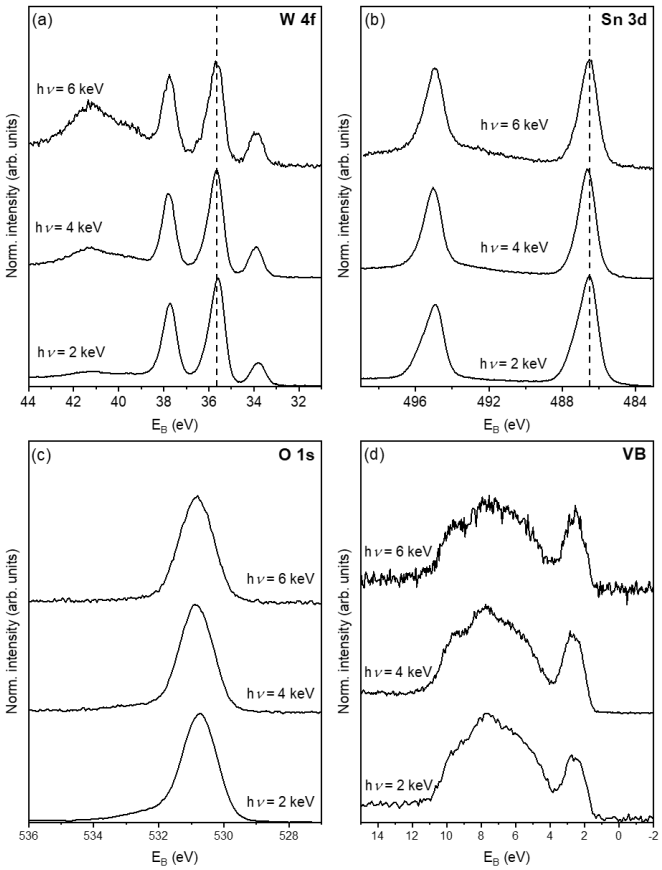

Figure A3. HAXPES measurements performed on pristine α-$SnWO_4$ films using photon energies of 2, 4, and 6 keV as indicated in the graphs. The W 4f core level is shown in (a), the Sn 3d core level in (b), the O 1s spectra in (c), and the valence band (VB) spectra are depicted in (d).

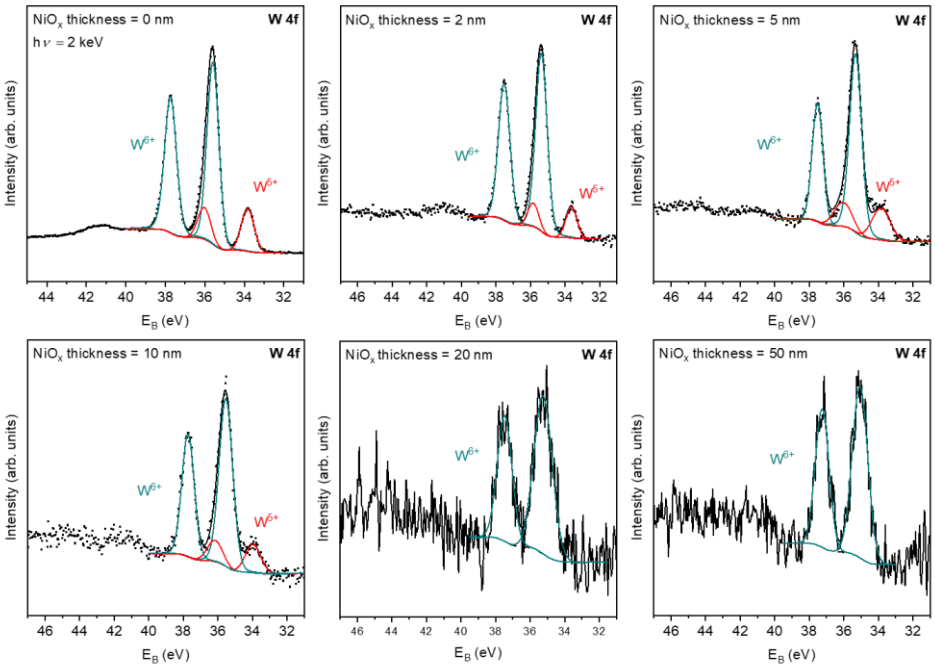

Figure A4. De-convoluted W 4f core level spectra of α-$SnWO_4$ measured by HAXPES with a photon energy of 2 keV. The NiO_x thickness is indicated in the graphs, and varies between 0 nm (i.e., the pristine film) and 50 nm. The fits for the measurements with 4 keV and 6 keV were performed based on the same procedure as presented here or 2 keV. They can be found in the supplemental information of reference.[92]

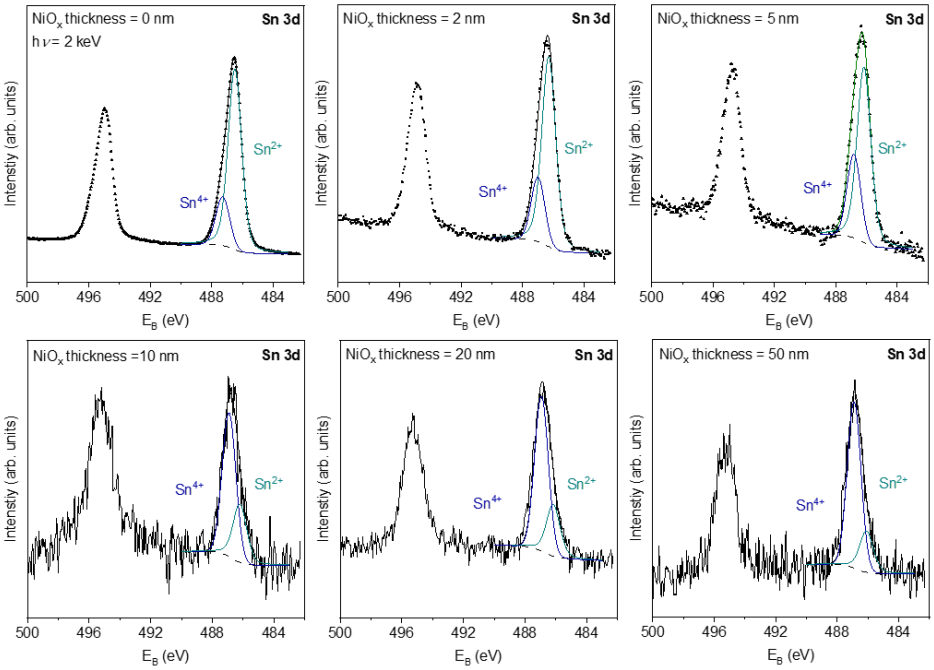

Figure A5. De-convoluted Sn 3d core level spectra of α-$SnWO_4$ measured by HAXPES with photon energy of 2 keV. The NiO_x thickness is indicated in the graphs, and varies between 0 nm (i.e., the pristine film) and 50 nm. The fits for the Sn 3d spectra measured with 4 keV and 6 keV can be found in the supplemental information of reference.[92]

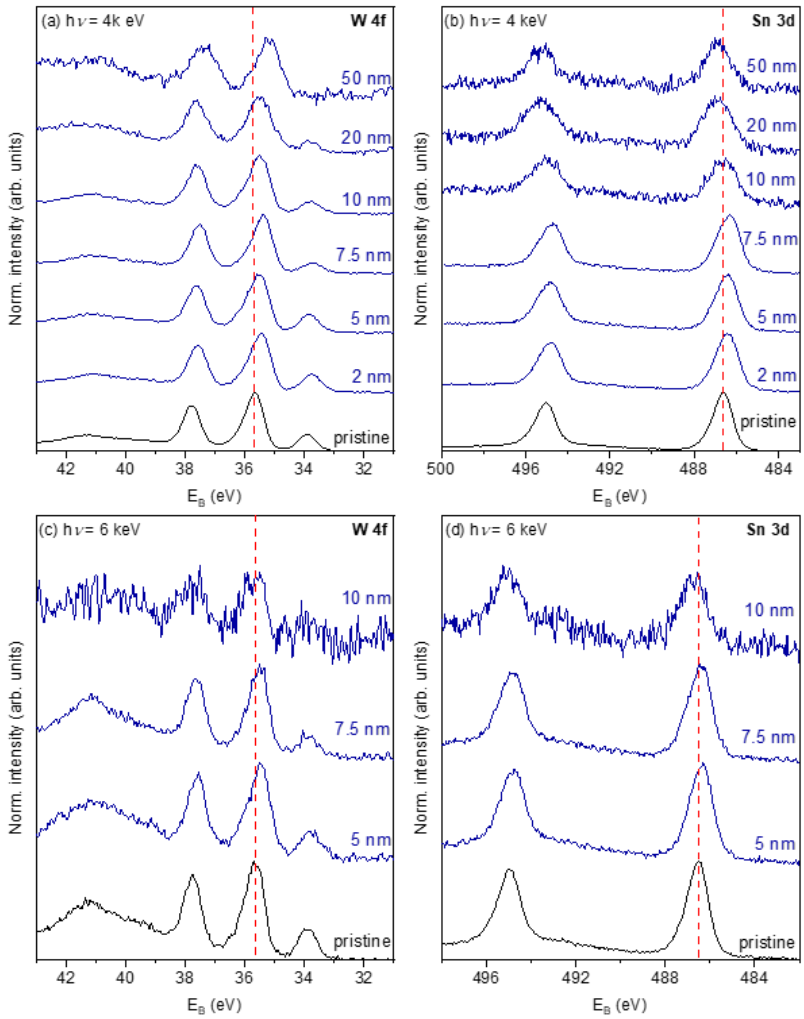

Figure A6. In (a) and (b) W 4f and Sn 3d core level spectra of α-$SnWO_4$ are shown, which were measured with HAXPES using a photon energy of 4 keV. As indicated in the graphs the pristine film is compared with samples coated with an increasing NiO_x thickness. The W 4f and Sn 3d core level measurements performed with 6 keV are depicted in (c) and (d). In all graphs the position of the W^{6+} and Sn^{2+} peaks corresponding to the pristine sample are indicated.

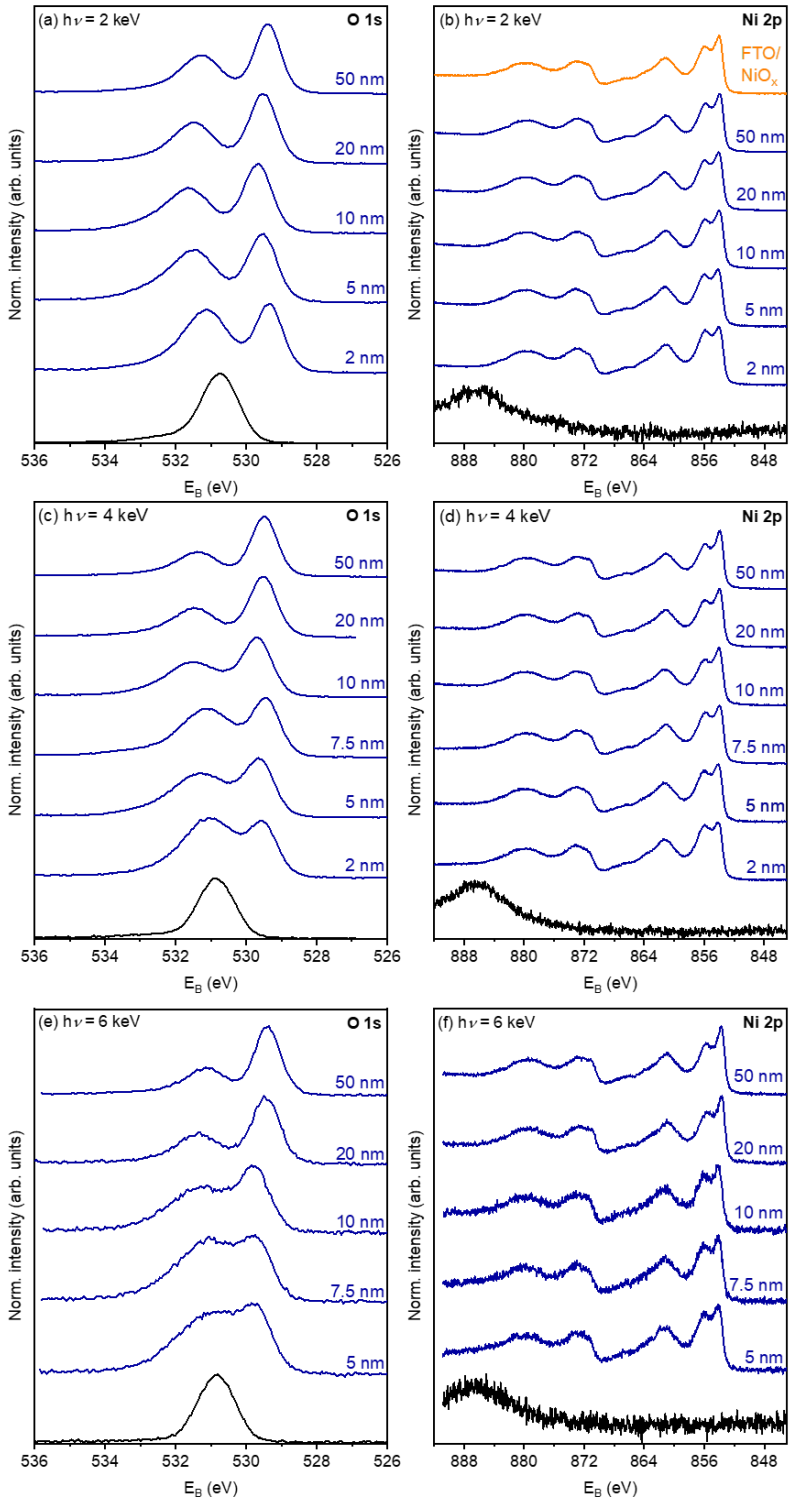

Figure A7. (a) O 1s core level spectra of α-$SnWO_4$ and α-$SnWO_4$/NiO_x measured with HAXPES using a photon energy of 2 keV. The pristine film (black) is compared with the NiO_x coated films. (b) Ni 2p spectra measured with 2 keV. For comparison the measurement performed on a FTO/NiO_x reference sample is shown. (c) O 1s spectra measured with 4 keV. (d) Ni 2p core level spectra measured with 4 keV. The O 1s and Ni 2p core level spectra measured with HAXPES using a photon energy of 6 keV are shown in (e) and (f), respectively.

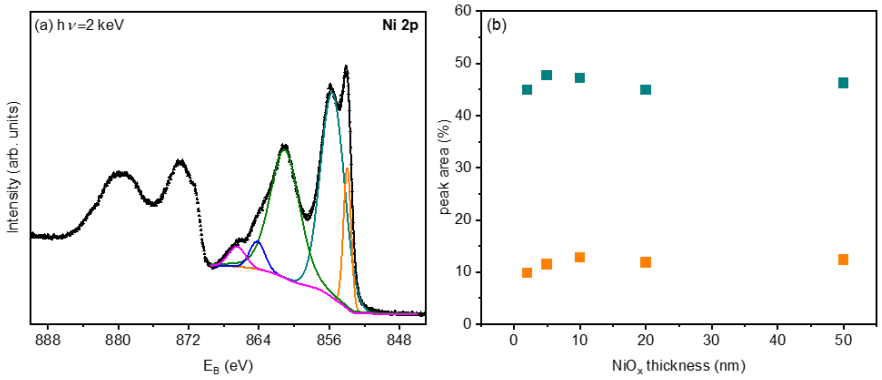

Figure A8. De-convoluted Ni 2p spectrum of a α-$SnWO_4$ film coated with 2 nm NiO_x. Measurement was performed with HAXPES using a photon energy of 2 keV. The peaks were fitted based on a procedure reported in literature (peak 1 = red, peak 2 = cyan, peak 3 = olive, peak 4 = blue and peak 5 = magenta).[215] (b) Peak contributions of peak 1 and 2 as a function of the NiO_x layer thickness. A significant change cannot be found, indicating that the chemical nature of NiO_x does no change when varying the thickness. Extracted peak areas were normalized on the total area of the de-convoluted spectrum. The peak contributions also agree well with the reported fitting procedure.[215]

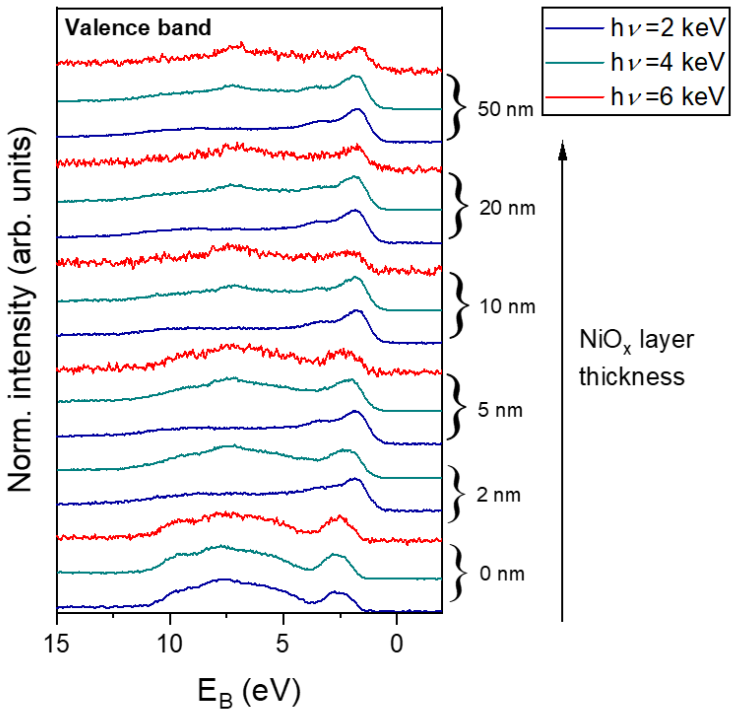

Figure A9. Valence band spectra of pristine α-$SnWO_4$ and α-$SnWO_4$ films coated with different thicknesses of NiO_x. HAXPES measurements were performed with photon energies of 2, 4, and 6 keV. The NiO_x thickness is indicated in the figure. With an increasing thickness of NiO_x valence band features related to α-$SnWO_4$ are attenuated and NiO_x features are enhanced. An effect of change in probing depth can also be observed, due to the variation of the photon energy.

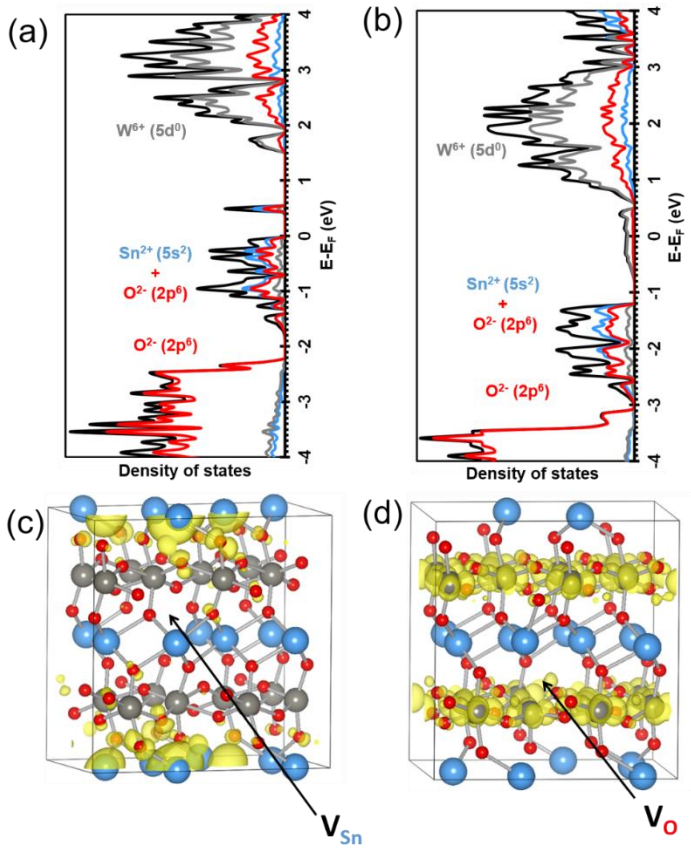

Figure A10. (a) Effect of Sn-vacancies on the electronic density of states of α-$SnWO_4$ calculated by DFT. Presence of a shallow electronic state is observed in the band gap above the VBM. The introduction of the Sn-vacancies is accompanied by the partial oxidation of Sn^{2+}. (b) Appearance of a broad electronic state in the band gap is found, if O-vacancies are introduced in the model calculation. The introduction of O-vacancies represents the reduction of W^{6+} to W^{5+}. (c) shows the partial charge density map of the Sn-vacancy model, which suggests that the presence of Sn-vacancies is related to the oxidation of Sn^{2+} to Sn^{3+}. This originates from the charge distribution of the released holes over two Sn species. The partial charge density map in (d) reveals a strong delocalization of released charges for the case of O-vacancies. Sn atoms = blue, W atoms = grey, O atoms = red.

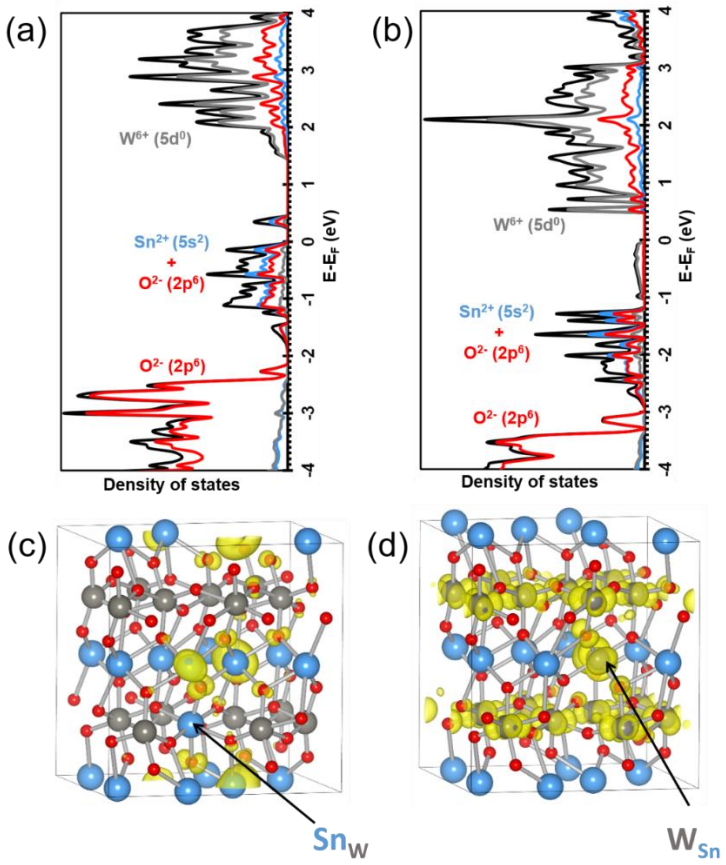

Figure A11. (a) Density of states calculated by DFT for the α-$SnWO_4$ structure, where Sn replaces W (antisite defect). An additional electronic state in the band gap can be observed above the VBM. The situation is similar to the case of the Sn-vacancy in Figure A.10. (b) Density of states for α-$SnWO_4$, in which W replaces Sn. A broad electronic state is introduced in the band gap. (d) Partial charge density map for the calculation shown in (a). The charge density around the atoms is indicated in yellow. (d) Partial charge density map for the calculation shown in (b). Sn atoms = blue, W atoms = grey, O atoms = red.

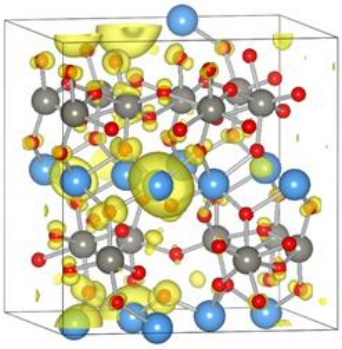

Figure A12. Partial charge density map for the DFT calculation in Figure 3.8d. In this model, the α-$SnWO_4$ structure shown in Figure 3.8b contains a W-vacancy, which compensates Sn^{4+} defects. The charge distribution is indicated in yellow, which indicates a localized character of the electronic state associated with the presence of W-vacancy. Sn atoms = blue, W atoms = grey, O atoms = red.

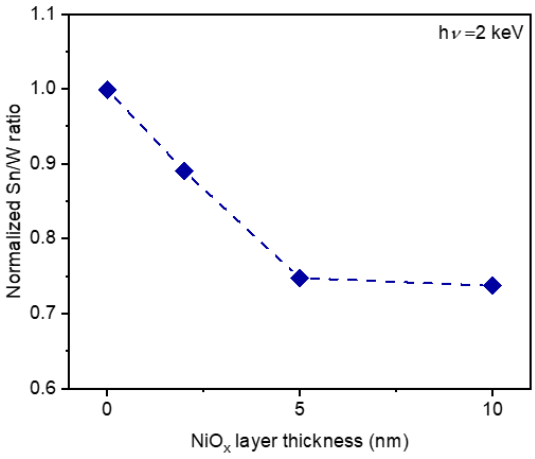

Figure A13. Normalized Sn/W ratio extracted from W 4f and Sn 3d core levels measured by HAXPES with a photon energy of 2 keV. The pristine α-$SnWO_4$ film is compared with samples coated with an increasing thickness of NiO_x. The peak areas and ionization cross-sections were used to estimate the Sn/W ratio. Normalization of the values was performed with respect to the pristine film. For the Sn^{4+} compensation by W-vacancies, a decrease of the W contribution would be expected for an increasing NiO_x layer thickness (the corresponding DFT calculations are shown in Figure 3.8 and A.13, which show the localized character of this in the middle of the band gap). This however is not the case for the data obtained in this study and, thus, considered as an argument against the presence of a significant amount of W-vacancies.

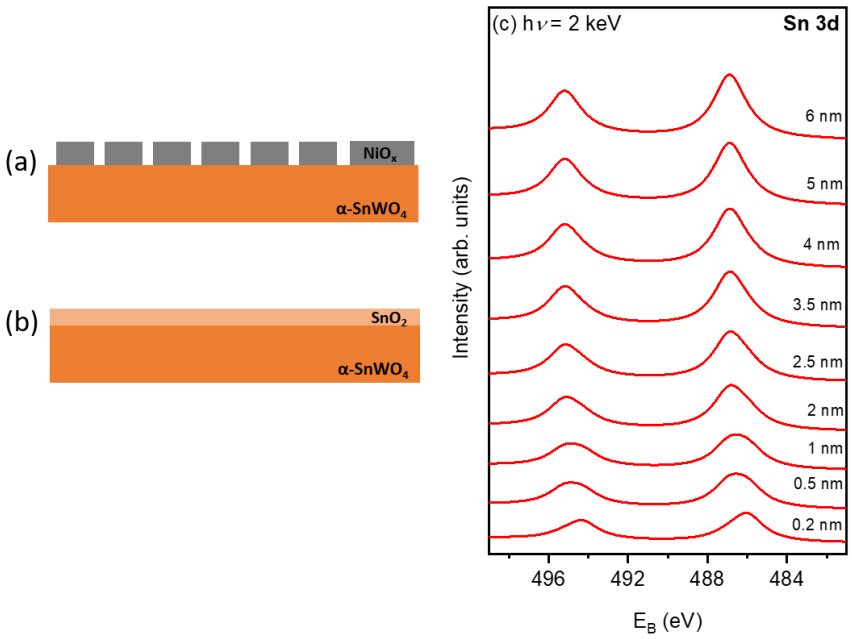

Figure A14. (a) Illustration of an α-$SnWO_4$ film coated with a NiO_x layer, which exhibits an island growth. This model structure as well as a model with a dense and flat NiO_x layer on top of α-$SnWO_4$ were used to simulate the Sn 3d core level spectra using the SESSA software package. [180] Peak intensity simulations performed with this software are based on a Monte Carlo algorithm. Comparing the simulated spectra for both morphologies with the experimental data, suggests that an estimated ~20 % of the α-$SnWO_4$ surface is not covered by NiO_x. Hence, the NiO_x layer deposited by PLD exhibits an island morphology. (b) The NiO_x layer only attenuates the signal arising from α-$SnWO_4$ and other phases, and has no impact on the relative ratio of the different oxidation states of the underlying phases. Therefore, only α-$SnWO_4$ covered with different thicknesses of SnO_2 is simulated, as schematically illustrated. In this model the SnO_2 layer is assumed to have a flat and dense morphology. (c) For the different SnO_2 thicknesses, the Sn 3d core level spectra were simulated, and the relative contributions of Sn^{4+} to the total signal were extracted from the simulated spectra.

B. Supplemental information for Chapter 4: intra-band gap states in α-$SnWO_4$ photoanodes introduced by surface modifications

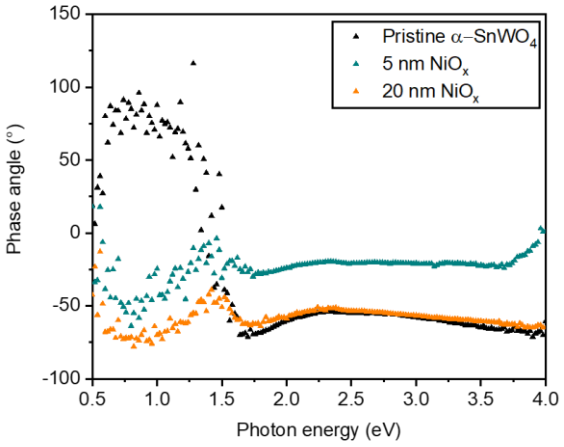

Figure B1. Phase angle analysis as function of the photon energy of the modulated SPV measurements shown in Figure 4.2. A pristine α-$SnWO_4$ film and NiO_x-coated films are compared. Below the band gap energy, the charge carrier recombination has a different nature for pristine and NiO_x coated films, indicated by the different sign of the phase angle. This suggests the modification of bulk or surface state related charge generation/recombination by deposition of NiO_x.

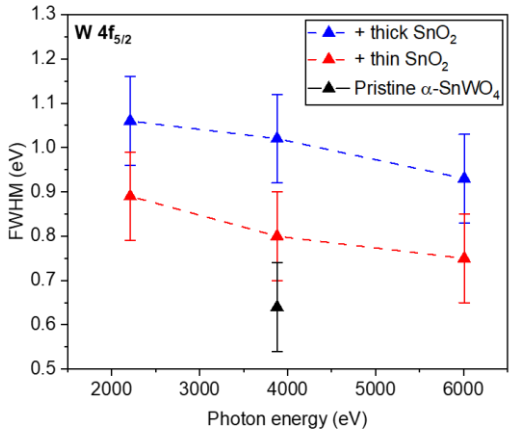

Figure B2. Estimation of the FWHM of the W $4f_{5/2}$ peak measured by HAXPES on a pristine α-$SnWO_4$ film and SnO_2 coated α-$SnWO_4$. The peak broadening may indicate the presence of two different W^{6+} species. This may suggest the presence of WO_3.

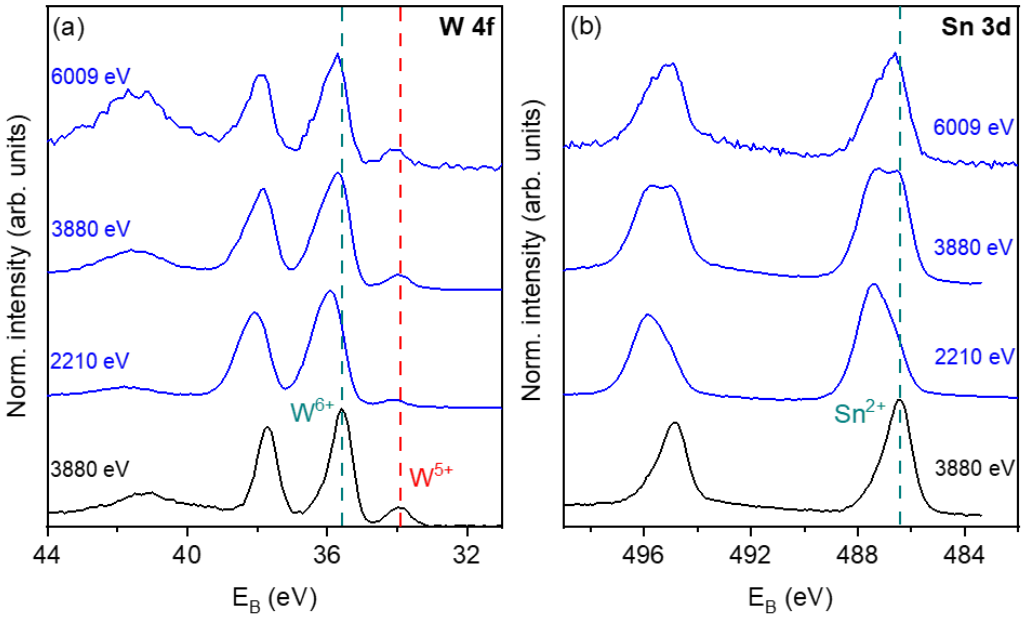

Figure B3. HAXPES measurements performed on pristine a α-$SnWO_4$ film and α-$SnWO_4$/SnO_2 samples using various photon energies as indicated in the graphs. The SnO_2 layer has an estimated thickness of ~12 nm and was formed by photoelectrochemical oxidation at 1.23 V vs. RHE in pH KP_i. The W 4f core level is shown in (a), and the Sn 3d core level in (b). The relative contributions of the different oxidation states and the binding energies are represented in Figure 4.4. Note that the photon energies were chosen differently compared to Chapter 3, to match with the valence band measurements in resonant condition.

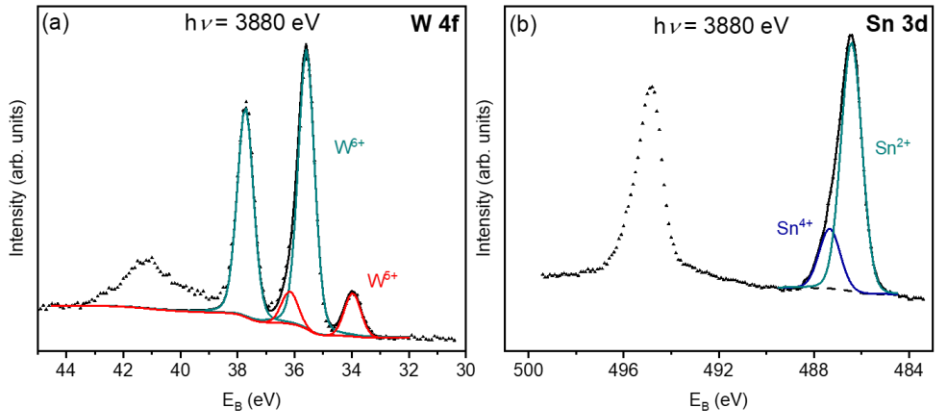

Figure B4. (a) De-convoluted W 4f spectrum of a pristine α-$SnWO_4$ film measured with hν = 3880 eV. (b) Sn 3d core level spectrum of the same sample de-convoluted into Sn^{2+} and Sn^{4+} contributions. Fitting was performed as described in Chapter 2.3.1.

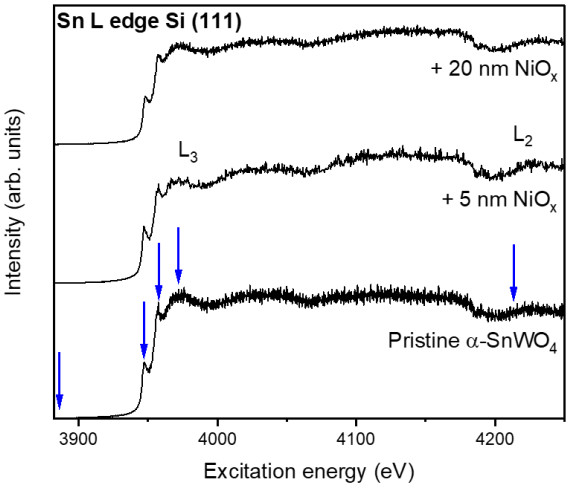

Figure B5. XAS spectra of pristine and NiO_x-coated α-$SnWO_4$ films. Measurement of the Sn $L_{3,2}$-edge was performed with the Si (111) double crystal monochromator. The arrows indicate the absorption features at which the valence band measurements were performed.

Table B1. Comparison of the excitation energies of the absorption features in the Sn L_3-edge measured with the Si (111) and Si (311) double crystal monochromator.

Si (111)	Si (311)
3933 eV	3947 eV
3942 eV	3956 eV
3952 eV	3572 eV

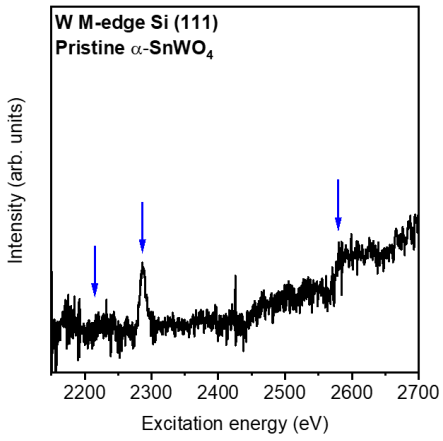

Figure B6. Representative W M-edge spectrum of a pristine α-$SnWO_4$ film measured by XAS using the Si (111) double monochromator crystal. Due to experimental limitations (the minimum photon energy at the beamline is 2003 eV), only the W M_1-edge could be measured. The M-edge has in general a lower fluorescence yield in comparison to K- or L-edges.

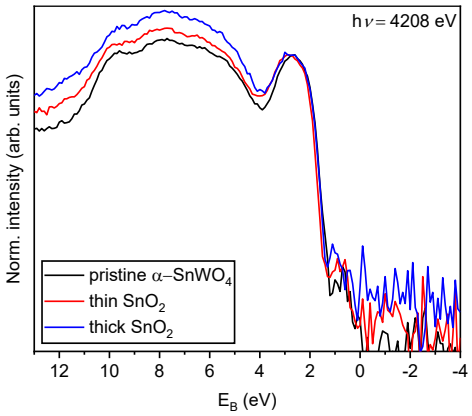

Figure B7. Valence band spectra of pristine and SnO_2 coated α-$SnWO_4$ films measured with HAXPES using the Si (311) monochromator, under resonance condition with the Sn L_2 absorption edge. A photon energy of hν = 4208 eV was used.

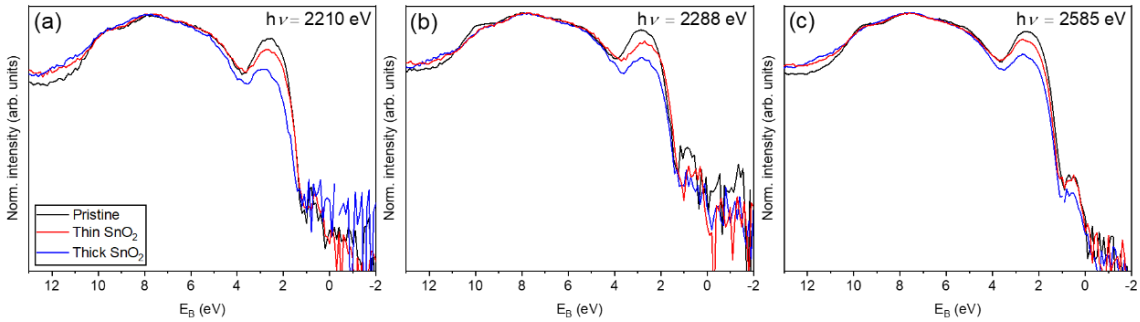

Figure B8. Valence band spectra of a pristine α-$SnWO_4$ film and α-$SnWO_4$/SnO_2 samples measured by HAXPES in resonance with the W M-edge. The different photon energies are indicated in the panels (a), (b), and (c). Indication of an intra-band state can be seen especially in (c).

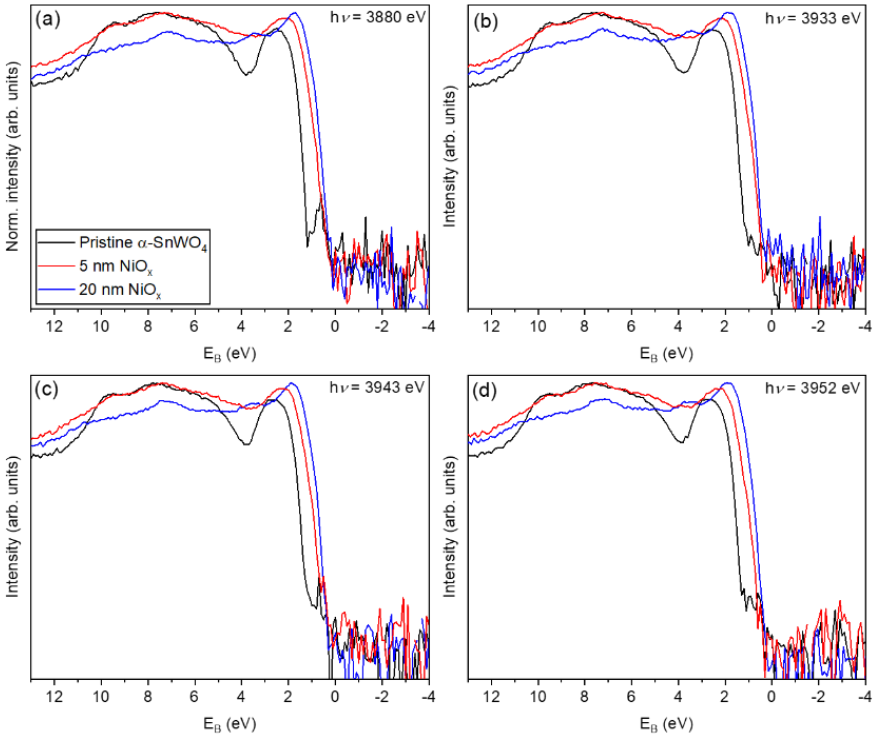

Figure B9. Valence band spectra of a pristine α-$SnWO_4$ film and α-$SnWO_4$/NiO_x samples measured with HAXPES. The used photon energies are indicated in the graphs, which correspond to features in the L_3-absorption edge of Sn. The NiO_x valence band overlaps with the valence band maximum of α-$SnWO_4$, and conceals the possible presence of the intra-band gap state.

C. Supplemental information for Chapter 5: pH-dependent stability of α-$SnWO_4$ photoelectrodes

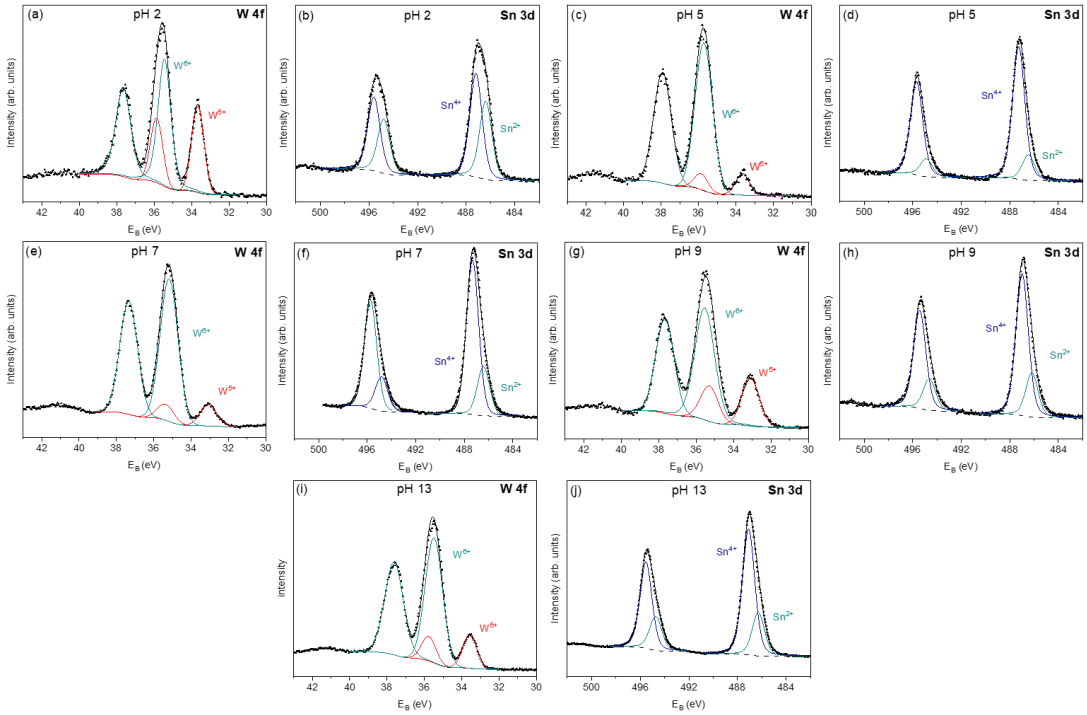

Figure C1. De-convoluted W 4f and Sn 3d core level spectra of α-$SnWO_4$ samples after PEC treatment measured by lab-based XPS. Samples were measured for 1 h at 1.23 V. vs. RHE in various pH electrolytes, as indicated in the panels. In all cases, a significant increase of the Sn^{4+} contribution can be observed after the PEC measurement in comparison to the pristine sample, which has a Sn^{4+} contribution of 22 ± 4 %, and agrees well with previous reports.[90, 92]

Figure C2. Photographs of α-$SnWO_4$ films after PEC treatment in various pH electrolytes. PEC measurements were performed for 1 h with an applied potential of 1.23 V vs. RHE. Clear dissolution and exposure of the FTO substrate can be observed in alkaline conditions. A visual change cannot be observed in acidic to neutral pH. The black dot indicates the center of the exposed film area.

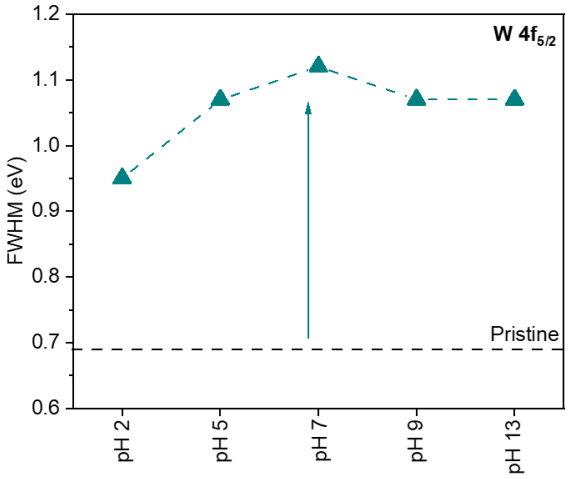

Figure C3. Full width at half maximum (FWHM) of the W $4f_{5/2}$ peak of α-$SnWO_4$ films. The samples were measured for 1h in various pH electrolytes with an applied potential of 1.23 V vs. RHE. For comparison the value of the pristine α-$SnWO_4$ film is indicated by the horizontal dashed line. A clear increase of the FWHM after the PEC measurements can be an indication for the presence of two W^{6+} species with differing binding energies. This may support the proposed formation of WO_3 on top of the α-$SnWO_4$ films, in addition to the SnO_2 phase.

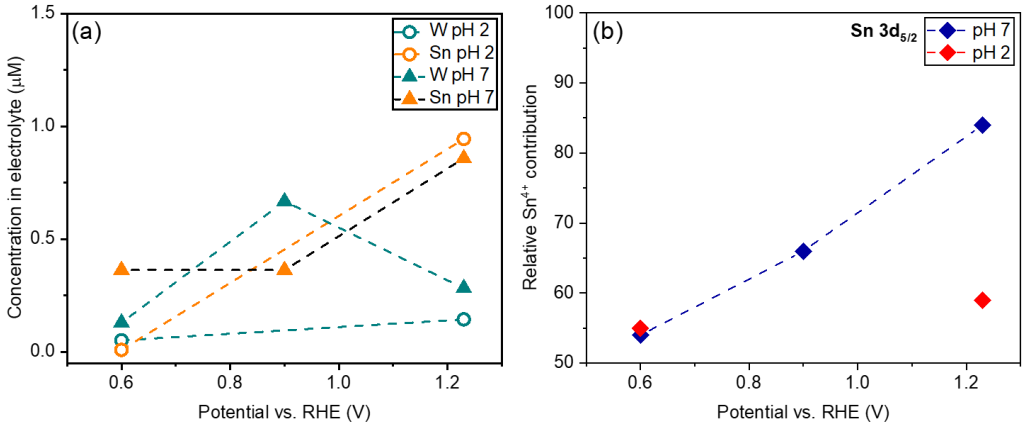

Figure C4. Potential dependence of the stability of α-$SnWO_4$ films in pH 2 and pH 7 electrolytes. (a) Concentration in the electrolyte after PEC measurements with various applied potentials measured by ICP-OES. A systematic trend cannot be observed. (b) Relative Sn^{4+} contribution estimated from peak fitting of Sn $3d_{5/2}$ spectra measured by lab-based XPS. Surface oxidation decreases for lower potentials in pH 2 and 7.

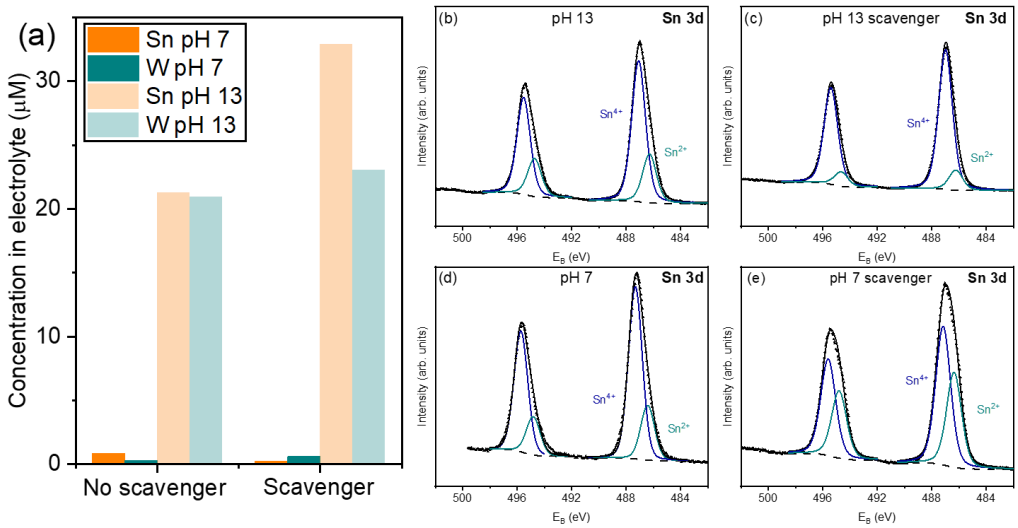

Figure C5. Comparison of the stability of α-$SnWO_4$ samples measured with and without scavenger. (a) ICP-OES measurements of the electrolyte performed after 1 h PEC treatment with an applied potential of 1.23 V vs. RHE. A clear impact of the presence of the scavenger cannot be observed. For comparison the measurements in pH 13 are presented, where strong dissolution was found. (b) and (c) show the de-convoluted Sn 3d spectra measured by lab-based XPS after PEC measurement in pH 13 with and without scavenger. The spectra for samples measured in pH 7 are shown in (d) and (e). In all cases, a significant increase of the relative Sn^{4+} contribution is observed. In pH 13 this is mainly related to exposure of the FTO substrate (i.e., F-doped SnO_2).

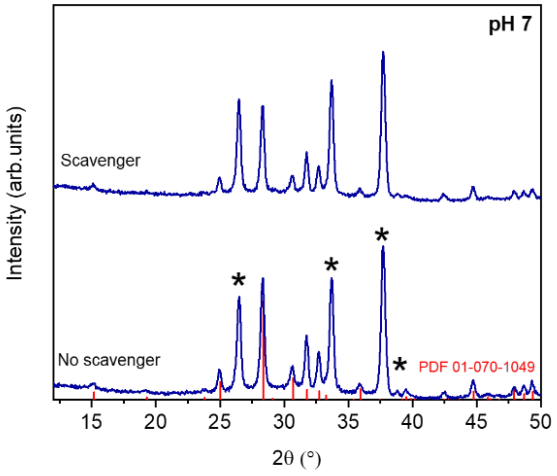

Figure C6. XRD analysis of the α-$SnWO_4$ samples evaluated in Figure C5. A difference between the pH 7 measurements performed at 1.23 V vs. RHE with and without scavenger is not observed. There is no clear change of the intensity ratio between α-$SnWO_4$ and FTO, as well as no secondary phase formation in both cases. The reference pattern for α-$SnWO_4$ is indicated in red and was taken from JCPDS 01-070-1049. FTO reflections are marked with asterisks.

D. List of abbreviations

IPCC	Intergovernmental Panel on Climate Change
MOF	Metal organic framework
PEC	photoelectrochemistry
STH efficiency	Solar-to-hydrogen efficiency
PEM	Proton exchange membrane
e^-	electron
h^+	hole
OER	Oxygen evolution reaction
HER	Hydrogen evolution reaction
φ_{OER} (H_2O/O_2)	Redox potential OER
φ_{HER} (H_2/H_2O)	Redox potential HER
ΔG	Gibbs free energy
F	Faraday constant
n	Number of charges
J_{photo}	Photocurrent density
P_{in}	Incident Power
AM1.5	Air Mass 1.5
E_F	Fermi level
W	Width of space charge layer
W_H	Width of Helmholtz layer
$E_{qF,n}$	Quasi Fermi level of electrons
$E_{qF,h}$	Quasi Fermi level of holes
ΔV_{photo}	Photovoltage
J_{max}	Theoretical maximum photocurrent density
ICPE	Incident photo-to-current efficiency
λ	Wavelength
E_{VBM}	Valence band maximum
E_{CBM}	Conduction band minimum
$\alpha(\lambda)$	Absorption coefficient

J_{abs}	Photocurrent density with 100 % APCE
APCE	Absorbed photon-to-current efficiency
$\xi(\lambda)$	Wavelength-dependent photogeneration yield
J_{PEC}	Measured photocurrent density
η_{sep}	Separation efficiency
η_{in}	Injection Efficiency
L_D	Diffusion length of minority charge carriers
D	Diffusivity
τ	Charge carrier lifetime
μ	Charge carrier mobility
T	Temperature
2-jn-a-Si	Double junction amorphous silicon solar cell
PLD	Pulsed laser deposition
DFT	Density functional theory
$\varphi_{SB,n}$	Schottky barrier height
ϕ_M	Work function of the metal
X_S	Electron affinity of the semiconductor
HAXPES	Hard X-ray photoelectron spectroscopy
SPV	Surface photovoltage
ICP – OES	Inductively coupled plasma – optical emission spectroscopy
XPS	X-ray photoelectron spectroscopy
XRD	X-ray diffraction
FTO	Fluorine doped tin oxide
F	Laser fluence
d	Target-to-substrate distance
PES	Photoelectron spectroscopy
E_{kin}	Kinetic energy of photoelectron
hν	Photon energy
E_{bind}	Binding energy
φ_{spec}	Spectrometer work function
IMPF (λ_{IMPF})	Inelastic mean free path

UPS	Ultraviolet photoelectron spectroscopy
E_{core}	Core level energy
φ_{Sample}	Sample work function
FWHM	Full width at half maximum
C_A	Relative contribution of species A
ResPES	Resonant photoelectron spectroscopy
XAS	X-ray absorption spectroscopy
d_{WE}	Radius of PEC exposed area of the working electrode
RHE	Reversible hydrogen electrode
V_{app}	Applied potential
$V_{Ag/AgCl}$	Potential versus Ag/AgCl reference electrode
KP_i	Potassium phosphate buffer
OCP	Open circuit potential
ΔOD	Change in optical density
T_I	Transmitted intensity
T_{ref}	Transmitted intensity before start of PEC measurement
Δ*CPD*	Contact potential difference
C_m	Measurement capacitor
R_m	Measurement resistance
X	Fast response signal in modulated SPV
Y	Slow response signal in modulated SPV
F_{mod}	Modulation frequency in SPV
T_{mod}	Modulation period in SPV
φ	Phase angle in modulated SPV
TEM	Transmission electron microscopy
LSV	Linear sweep voltammetry
DOS	Density of states
Q	Charge transferred across the interface

E. References

1. IEA, World Energy Outlook **2019**. https://www.iea.org/reports/world-energy-outlook-2019.
2. Howarth, R. W., A Bridge to Nowhere: Methane emissions and the greenhouse gas footprint of natural gas. *Energy Science & Engineering* **2014**, *2*, 47-60.
3. Yoosefian, M., Powerful greenhouse gas nitrous oxide adsorption onto intrinsic and Pd doped single walled carbon nanotube. *Applied Surface Science* **2017**, *392*, 225-230.
4. United Nations, Department of Economic and Social Affairs, Population Division, World Population Prospects **2019**. https://population.un.org/wpp/Graphs/Probabilistic/POP/TOT/900 (accessed 05.07.2021).
5. Allen, M. R.; Dube, O.P.; Solecki, W.; Aragón-Durand, F.; Cramer, W.; Humphreys, S.; Kainuma, M.; Kala, J.; Mahowald, N.; Mulugetta, Y.; Perez, R.; Wairiu, M.; Zickfeld, K., Framing and Context. In: Global Warming of 1.5°C. An IPCC Special Report on the Impacts of Global Warming of 1.5°C above Pre-Industrial Levels and Related Global Greenhouse Gas Emission Pathways, in the Context of Strengthening the Global Response to the Threat of Climate Change, Sustainable Development, and Efforts to Eradicate Poverty [Masson-Delmotte, V., P. Zhai, H.-O. Pörtner, D. Roberts, J. Skea, P. R. Shukla, A. Pirani, W. Moufouma-Okia, C. Péan, R. Pidcock, S. Connors, J. B. R. Matthews, Y. Chen, X. Zhou, M. I. Gomis, E. Lonnoy, T. Maycock, M. Tignor, and T. Waterfield (Eds.)] in Press. **2018**.
6. Fischer, E. M.; Knutti, R., Anthropogenic contribution to global occurrence of heavy-precipitation and high-temperature extremes. *Nature Climate Change* **2015**, *5*, 560-564.
7. Stott, P. A.; Stone, D. A.; Allen, M. R., Human contribution to the european heatwave of 2003. *Nature* **2004**, *432*, 610-614.
8. Pall, P.; Aina, T.; Stone, D. A.; Stott, P. A.; Nozawa, T.; Hilberts, A. G. J.; Lohmann, D.; Allen, M. R., Anthropogenic greenhouse gas contribution to flood risk in england and wales in autumn 2000. *Nature* **2011**, *470*, 382-385.
9. Norby, R. J.; Luo, Y., Evaluating ecosystem responses to rising atmospheric CO_2 and global warming in a multi-factor world. *New Phytologist* **2004**, *162*, 281-293.
10. IPCC, 2018: Summary for Policymakers. In: Global Warming of 1.5°C. An Ipcc Special Report on the Impacts of Global Warming of 1.5°C above Pre-Industrial Levels and Related Global Greenhouse Gas Emission Pathways, in the Context of Strengthening the Global Response to the Threat of Climate Change, Sustainable Development, and Efforts to Eradicate Poverty [Masson-Delmotte, V., P. Zhai, H.-O. Pörtner, D. Roberts, J. Skea, P. R. Shukla, A. Pirani, W. Moufouma-Okia, C. Péan, R. Pidcock, S. Connors, J. B. R. Matthews, Y. Chen, X. Zhou, M.I. Gomis, E. Lonnoy, T. Maycock, M. Tignor, and T. Waterfield (Eds.)]. In Press. 2018.
11. Hoegh-Guldberg, O.; Jacob, D.; Taylor, M.; Bindi, M.; Brown, S.; Camilloni, I.; Diedhiou, A.; Djalante, R.; Ebi, K. L.; Engelbrecht, F.; Guiot, J.; Hijioka, Y.; Mehrotra, S.; Payne, A.; Seneviratne, S. I.;Thomas, a; Warren, R.; Zhou; G., 2018: Impacts of 1.5°C Global Warming on Natural and Human Systems. In: Global Warming of 1.5°C. An IPCC Special Report on the Impacts of Global Warming of 1.5°C above Pre-Industrial Levels and Related Global Greenhouse Gas Emission Pathways, in the Context of Strengthening the Global Response to the Threat of Climate Change, Sustainable Development, and Efforts to Eradicate Poverty [Masson-Delmotte, V., P. Zhai, H.-O. Pörtner, D. Roberts, J. Skea, P. R. Shukla, A. Pirani, W. Moufouma-Okia, C. Péan, R. Pidcock, S. Connors, J. B. R. Matthews, Y. Chen, X. Zhou, M. I. Gomis, E. Lonnoy, T. Maycock, M. Tignor, and T. Waterfield (Eds.)]. In Press. **2018**.
12. IEA, Technology Roadmap, Hydrogen and Fuel Cells. **2015**. All Rights Reserved.
13. Chu, S.; Majumdar, A., Opportunities and challenges for a sustainable energy future. *Nature* **2012**, *488*, 294-303.
14. Chu, S.; Cui, Y.; Liu, N., The path towards sustainable energy. *Nature Materials* **2017**, *16*, 16-22.
15. van de Krol, R.; Grätzel, M., *Photoelectrochemical Hydrogen Production*; Springer, **2012**.

16. Cano, Z. P.; Banham, D.; Ye, S.; Hintennach, A.; Lu, J.; Fowler, M.; Chen, Z., Batteries and fuel cells for emerging electric vehicle markets. *Nature Energy* **2018**, *3*, 279-289.
17. Liu, Y.; Zhu, Y.; Cui, Y., Challenges and opportunities towards fast-charging battery materials. *Nature Energy* **2019**, *4*, 540-550.
18. Parkinson, B., Advantages of solar hydrogen compared to direct carbon dioxide reduction for solar fuel production. *ACS Energy Letters* **2016**, *1*, 1057-1059.
19. van de Krol, R.; Parkinson, B. A., Perspectives on the photoelectrochemical storage of solar energy. *MRS Energy & Sustainability* **2017**, *4*, E13.
20. Debe, M. K., Electrocatalyst approaches and challenges for automotive fuel cells. *Nature* **2012**, *486*, 43-51.
21. Dry, M. E., The Fischer–Tropsch Process: 1950–2000. *Catalysis Today* **2002**, *71*, 227-241.
22. da Rosa, A. V., *Fundamentals of Renewable Energy Processes,* Elsevier, **2008**.
23. Graetz, J., New approaches to hydrogen storage. *Chemical Society Reviews* **2009**, *38*, 73-82.
24. Schlapbach, L.; Züttel, A., hydrogen-storage materials for mobile applications. *Nature* **2001**, *414*, 353-358.
25. Erisman, J. W.; Sutton, M. A.; Galloway, J.; Klimont, Z.; Winiwarter, W., How a century of ammonia synthesis changed the world. *Nature Geoscience* **2008**, *1*, 636-639.
26. International Fertilizer Industry Association, Fertilizers, Climate Change and Enhancing Agricultural Productivity Sustainably; Paris, France, **2009**.
27. Ardo, S.; Fernandez Rivas, D.; Modestino, M. A.; Schulze Greiving, V.; Abdi, F. F.; Alarcon Llado, E.; Artero, V.; Ayers, K.; Battaglia, C.; Becker, J.-P.; Bederak, D.; Berger, A.; Buda, F.; Chinello, E.; Dam, B.; Di Palma, V.; Edvinsson, T.; Fujii, K.; Gardeniers, H.; Geerlings, H.; H. Hashemi, S. M.; Haussener, S.; Houle, F.; Huskens, J.; James, B. D.; Konrad, K.; Kudo, A.; Kunturu, P. P.; Lohse, D.; Mei, B.; Miller, E. L.; Moore, G. F.; Muller, J.; Orchard, K. L.; Rosser, T. E.; Saadi, F. H.; Schüttauf, J.-W.; Seger, B.; Sheehan, S. W.; Smith, W. A.; Spurgeon, J.; Tang, M. H.; van de Krol, R.; Vesborg, P. C. K.; Westerik, P., Pathways to electrochemical solar-hydrogen technologies. *Energy & Environmental Science* **2018**, *11*, 2768-2783.
28. Nielander, A. C.; Shaner, M. R.; Papadantonakis, K. M.; Francis, S. A.; Lewis, N. S., A Taxonomy for solar fuels generators. *Energy & Environmental Science* **2015**, *8*, 16-25.
29. Jacobsson, T. J.; Fjällström, V.; Edoff, M.; Edvinsson, T., Sustainable solar hydrogen production: from photoelectrochemical cells to PV-electrolyzers and back again. *Energy & Environmental Science* **2014**, *7*, 2056-2070.
30. Bodner, M.; Hofer, A.; Hacker, V., H_2 generation from alkaline electrolyzer. *WIREs Energy and Environment* **2015**, *4*, 365-381.
31. Jia, J.; Seitz, L. C.; Benck, J. D.; Huo, Y.; Chen, Y.; Ng, J. W. D.; Bilir, T.; Harris, J. S.; Jaramillo, T. F., solar water splitting by photovoltaic-electrolysis with a solar-to-hydrogen efficiency over 30 %. *Nature Communications* **2016**, *7*, 13237.
32. Verlage, E.; Hu, S.; Liu, R.; Jones, R. J. R.; Sun, K.; Xiang, C.; Lewis, N. S.; Atwater, H. A., A monolithically integrated, intrinsically safe, 10 % efficient, solar-driven water-splitting system based on active, stable earth-abundant electrocatalysts in conjunction with tandem III–V light absorbers protected by amorphous TiO_2 films. *Energy & Environmental Science* **2015**, *8*, 3166-3172.
33. Young, J. L.; Steiner, M. A.; Döscher, H.; France, R. M.; Turner, J. A.; Deutsch, Todd G., Direct solar-to-hydrogen conversion via inverted metamorphic multi-junction semiconductor architectures. *Nature Energy* **2017**, *2*, 17028.
34. Cheng, W.-H.; Richter, M. H.; May, M. M.; Ohlmann, J.; Lackner, D.; Dimroth, F.; Hannappel, T.; Atwater, H. A.; Lewerenz, H.-J., Monolithic photoelectrochemical device for direct water splitting with 19 % efficiency. *ACS Energy Letters* **2018**, *3*, 1795-1800.

35. Ye, X.; Melas-Kyriazi, J.; Feng, Z. A.; Melosh, N. A.; Chueh, W. C., A semiconductor/mixed ion and electron conductor heterojunction for elevated-temperature water splitting. *Physical Chemistry Chemical Physics* **2013**, *15*, 15459-15469.
36. Haussener, S.; Hu, S.; Xiang, C.; Weber, A. Z.; Lewis, N. S., Simulations of the irradiation and temperature dependence of the efficiency of tandem photoelectrochemical water-splitting systems. *Energy & Environmental Science* **2013**, *6*, 3605-3618.
37. Würfel, P., *Physics of Solar Cells*; Wiley-VCH: Weinheim, **2005**.
38. Kölbach, M.; Rehfeld, K.; May, M. M., Efficiency gains for thermally coupled solar hydrogen production in extreme cold. *Energy & Environmental Science* **2021,** *14***,** 4410-4417.
39. Turan, B.; Becker, J.-P.; Urbain, F.; Finger, F.; Rau, U.; Haas, S., Upscaling of integrated photoelectrochemical water-splitting devices to large areas. *Nature Communications* **2016**, *7*, 12681.
40. Obata, K.; van de Krol, R.; Schwarze, M.; Schomäcker, R.; Abdi, F. F., *In situ* observation of pH change during water splitting in neutral pH conditions: impact of natural convection driven by buoyancy effects. *Energy & Environmental Science* **2020**, *13*, 5104-5116.
41. Ahmet, I. Y.; Ma, Y.; Jang, J.-W.; Henschel, T.; Stannowski, B.; Lopes, T.; Vilanova, A.; Mendes, A.; Abdi, F. F.; van de Krol, R., Demonstration of a 50 cm^2 $BiVO_4$ tandem photoelectrochemical-photovoltaic water splitting device. *Sustainable Energy & Fuels* **2019**, *3*, 2366-2379.
42. Shaner, M. R.; Atwater, H. A.; Lewis, N. S.; McFarland, E. W., A comparative technoeconomic analysis of renewable hydrogen production using solar energy. *Energy & Environmental Science* **2016**, *9*, 2354-2371.
43. Zhai, P.; Haussener, S.; Ager, J.; Sathre, R.; Walczak, K.; Greenblatt, J.; McKone, T., Net primary energy balance of a solar-driven photoelectrochemical water-splitting device. *Energy & Environmental Science* **2013**, *6*, 2380-2389.
44. Sathre, R.; Scown, C. D.; Morrow, W. R.; Stevens, J. C.; Sharp, I. D.; Ager, J. W.; Walczak, K.; Houle, F. A.; Greenblatt, J. B., Life-cycle net energy assessment of large-scale hydrogen production via photoelectrochemical water splitting. *Energy & Environmental Science* **2014**, *7*, 3264-3278.
45. Pinaud, B. A.; Benck, J. D.; Seitz, L. C.; Forman, A. J.; Chen, Z.; Deutsch, T. G.; James, B. D.; Baum, K. N.; Baum, G. N.; Ardo, S.; Wang, H.; Miller, E.; Jaramillo, T. F., Technical and economic feasibility of centralized facilities for solar hydrogen production via photocatalysis and photoelectrochemistry. *Energy & Environmental Science* **2013**, *6*, 1983-2002.
46. Sivula, K.; van de Krol, R., Semiconducting materials for photoelectrochemical energy conversion. *Nature Reviews Materials* **2016**, *1*, 15010.
47. Walter, M. G.; Warren, E. L.; McKone, J. R.; Boettcher, S. W.; Qixi Mi; Santori, E. A.; Lewis, N. S., Solar water splitting cells. *Chemical Reviews* **2010**, *110*, 6446-6473.
48. Turner, J. A., Energetics of the semiconductor-electrolyte interface. *Journal of Chemical Education* **1983**, *60*, 327-329.
49. Reichman, J., The current-voltage characteristics of semiconductor-electrolyte junction photovoltaic cells. *Applied Physics Letters* **1980**, *36*, 574-577.
50. Lee, D. K.; Lee, D.; Lumley, M. A.; Choi, K. S., Progress on ternary oxide-based photoanodes for use in photoelectrochemical cells for solar water splitting. *Chemical Society Reviews* **2019**, *48*, 2126-2157.
51. Abdi, F. F.; Berglund, S. P., Recent developments in complex metal oxide photoelectrodes. *Journal of Physics D: Applied Physics* **2017**, *50*, 193002.
52. Jiang, C.; Moniz, S. J. A.; Wang, A.; Zhang, T.; Tang, J., Photoelectrochemical devices for solar water splitting – materials and challenges. *Chemical Society Reviews* **2017**, *46*, 4645-4660.
53. Bolton, J. R.; Strickler, S. J.; Connolly, J. S., Limiting and realizable efficiencies of solar photolysis of water. *Nature* **1985**, *316*, 495-500.

54. Weber, M. F.; Dignam, M. J., Splitting water with semiconducting photoelectrodes—efficiency considerations. *International Journal of Hydrogen Energy* **1986**, *11*, 225-232.
55. Seitz, L. C.; Chen, Z.; Forman, A. J.; Pinaud, B. A.; Benck, J. D.; Jaramillo, T. F., Modeling practical performance limits of photoelectrochemical water splitting based on the current state of materials research. *ChemSusChem* **2014**, *7*, 1372-1385.
56. The American Society for Testing and Materials (ASTM) G-173 Spectra. https://www.nrel.gov/grid/solar-resource/spectra-am1.5.html (accessed 13.08.2021).
57. Grave, D. A.; Ellis, D. S.; Piekner, Y.; Kölbach, M.; Dotan, H.; Kay, A.; Schnell, P.; van de Krol, R.; Abdi, F. F.; Friedrich, D.; Rothschild, A., Extraction of mobile charge carrier photogeneration yield spectrum of ultrathin-film metal oxide photoanodes for solar water splitting. *Nature Materials* **2021**, *20*, 833-840.
58. Dotan, H.; Sivula, K.; Grätzel, M.; Rothschild, A.; Warren, S. C., Probing the photoelectrochemical properties of hematite (α-Fe_2O_3) electrodes using hydrogen peroxide as a hole scavenger. *Energy & Environmental Science* **2011**, *4*, 958-964.
59. Foley, J. M.; Price, M. J.; Feldblyum, J. I.; Maldonado, S., Analysis of the operation of thin nanowire photoelectrodes for solar energy conversion. *Energy & Environmental Science* **2012**, *5*, 5203-5220.
60. Zhou, M.; Bao, J.; Bi, W.; Zeng, Y.; Zhu, R.; Tao, M.; Xie, Y., Efficient water splitting via a heteroepitaxial $BiVO_4$ photoelectrode decorated with Co-Pi catalysts. *ChemSusChem* **2012**, *5*, 1420-1425.
61. Govindaraju, G. V.; Wheeler, G. P.; Lee, D.; Choi, K.-S., Methods for electrochemical synthesis and photoelectrochemical characterization for photoelectrodes. *Chemistry of Materials* **2017**, *29*, 355-370.
62. Hu, S.; Xiang, C.; Haussener, S.; Berger, A. D.; Lewis, N. S., An analysis of the optimal band gaps of light absorbers in integrated tandem photoelectrochemical water-splitting systems. *Energy & Environmental Science* **2013**, *6*, 2984.
63. Fujishima, A.; Honda, K., Electrochemical photolysis of water at a semiconductor electrode. *Nature* **1972**, *238*, 37-38.
64. Tang, J.; Durrant, J. R.; Klug, D. R., Mechanism of photocatalytic water splitting in TiO_2. Reaction of water with photoholes, importance of charge carrier dynamics, and evidence for four-hole chemistry. *Journal of the American Chemical Society* **2008**, *130*, 13885-13891.
65. Wang, G.; Wang, H.; Ling, Y.; Tang, Y.; Yang, X.; Fitzmorris, R. C.; Wang, C.; Zhang, J. Z.; Li, Y., Hydrogen-treated TiO_2 nanowire arrays for photoelectrochemical water splitting. *Nano Letters* **2011**, *11*, 3026-3033.
66. Kavan, L.; Grätzel, M., Highly efficient semiconducting TiO_2 photoelectrodes prepared by aerosol pyrolysis. *Electrochimica Acta* **1995**, *40*, 643-652.
67. Hou, Y.; Abrams, B. L.; Vesborg, P. C. K.; Björketun, M. E.; Herbst, K.; Bech, L.; Setti, A. M.; Damsgaard, C. D.; Pedersen, T.; Hansen, O.; Rossmeisl, J.; Dahl, S.; Nørskov, J. K.; Chorkendorff, I., Bioinspired molecular co-catalysts bonded to a silicon photocathode for solar hydrogen evolution. *Nature Materials* **2011**, *10*, 434-438.
68. Kenney, M. J.; Gong, M.; Li, Y.; Wu, J. Z.; Feng, J.; Lanza, M.; Dai, H., High-performance silicon photoanodes passivated with ultrathin nickel films for water oxidation. *Science* **2013**, *342*, 836-840.
69. Luo, Z.; Wang, T.; Gong, J., Single-crystal silicon-based electrodes for unbiased solar water splitting: current status and prospects. *Chemical Society Reviews* **2019**, *48*, 2158-2181.
70. Khaselev, O.; Turner, J. A., A monolithic photovoltaic-photoelectrochemical device for hydrogen production via water splitting. *Science* **1998**, *280*, 425-427.
71. Gu, J.; Yan, Y.; Young, J. L.; Steirer, K. X.; Neale, N. R.; Turner, J. A., Water reduction by a p-$GaInP_2$ photoelectrode stabilized by an amorphous TiO_2 coating and a molecular cobalt catalyst. *Nature Materials* **2016**, *15*, 456-460.

72. Khaselev, O.; Turner, J. A., Electrochemical stability of p-$GaInP_2$ in aqueous electrolytes toward photoelectrochemical water splitting. *Journal of The Electrochemical Society* **1998**, *145*, 3335-3339.
73. Nann, T.; Ibrahim, S. K.; Woi, P.-M.; Xu, S.; Ziegler, J.; Pickett, C. J., Water splitting by visible light: A nanophotocathode for hydrogen production. *Angewandte Chemie International Edition* **2010**, *49*, 1574-1577.
74. Sun, K.; Kuang, Y.; Verlage, E.; Brunschwig, B. S.; Tu, C. W.; Lewis, N. S., Sputtered NiO_x films for stabilization of p+n-InP photoanodes for solar-driven water oxidation. *Advanced Energy Materials* **2015**, *5*, 1402276.
75. Gao, X.; Kocha, S.; Frank, A. J.; Turner, J. A., Photoelectrochemical decomposition of water using modified monolithic tandem cells. *International Journal of Hydrogen Energy* **1999**, *24*, 319-325.
76. Ziwritsch, M.; Müller, S.; Hempel, H.; Unold, T.; Abdi, F. F.; van de Krol, R.; Friedrich, D.; Eichberger, R., Direct time-resolved observation of carrier trapping and polaron conductivity in $BiVO_4$. *ACS Energy Letters* **2016**, *1*, 888-894.
77. Rettie, A. J. E.; Chemelewski, W. D.; Emin, D.; Mullins, C. B., Unravelling small-polaron transport in metal oxide photoelectrodes. *The Journal of Physical Chemistry Letters* **2016**, *7*, 471-479.
78. Kamins, T. I., Hall mobility in chemically deposited polycrystalline silicon. *Journal of Applied Physics* **1971**, *42*, 4357-4365.
79. Woodhouse, M.; Parkinson, B. A., Combinatorial approaches for the identification and optimization of oxide semiconductors for efficient solar photoelectrolysis. *Chemical Society Reviews* **2009**, *38*, 197-210.
80. Castelli, I. E.; Landis, D. D.; Thygesen, K. S.; Dahl, S.; Chorkendorff, I.; Jaramillo, T. F.; Jacobsen, K. W., New cubic perovskites for one- and two-photon water splitting using the computational materials repository. *Energy & Environmental Science* **2012**, *5*, 9034-9043.
81. Castelli, I. E.; Hüser, F.; Pandey, M.; Li, H.; Thygesen, K. S.; Seger, B.; Jain, A.; Persson, K. A.; Ceder, G.; Jacobsen, K. W., New light-harvesting materials using accurate and efficient bandgap calculations. *Advanced Energy Materials* **2015**, *5*, 1400915.
82. Xiong, Y; Campbell, Q. T.; Fanghanel, J.; Badding, C. K.; Wang, H.; Kirchner-Hall, N. E.; Theibault, M. J.; Timrov, I.; Mondschein, J. S.; Seth, K.; Katz, R.; Villarino, A. M.; Pamuk, B.; Penrod, M. E.; Khan, M. M.; Rivera, T.; Smith, N. C.; Quintana, X.; Orbe, P.; Fennie, C. J.; Asem-Hiablie, S.; Young, J. L.; Deutsch, T. G.; Cococcioni, M.; Gopalan, V.; Abruña, H. D.; Schaak, R. E.; Dabo, I., Optimizing accuracy and efficacy in data-driven materials discovery for the solar production of hydrogen. *Energy & Environmental Science* **2021**, *14*, 2335-2348.
83. Katz, J. E.; Gingrich, T. R.; Santori, E. A.; Lewis, N. S., Combinatorial synthesis and high-throughput photopotential and photocurrent screening of mixed-metal oxides for photoelectrochemical water splitting. *Energy & Environmental Science* **2009**, *2*, 103-112.
84. Kudo, A.; Ueda, K.; Kato, H.; Mikami, I., Photocatalytic O_2 evolution under visible light irradiation on $BiVO_4$ in aqueous $AgNO_3$ solution. *Catalysis Letters* **1998**, *53*, 229-230.
85. Kuang, Y.; Jia, Q.; Ma, G.; Hisatomi, T.; Minegishi, T.; Nishiyama, H.; Nakabayashi, M.; Shibata, N.; Yamada, T.; Kudo, A.; Domen, K., Ultrastable low-bias water splitting photoanodes via photocorrosion inhibition and in situ catalyst regeneration. *Nature Energy* **2017**, *2*, 16191.
86. Pan, L.; Kim, J. H.; Mayer, M. T.; Son, M.-K.; Ummadisingu, A.; Lee, J. S.; Hagfeldt, A.; Luo, J.; Grätzel, M., Boosting the performance of Cu_2O photocathodes for unassisted solar water splitting devices. *Nature Catalysis* **2018**, *1*, 412-420.
87. Kay, A.; Cesar, I.; Grätzel, M., New benchmark for water photooxidation by nanostructured α-Fe_2O_3 films. *Journal of the American Chemical Society* **2006**, *128*, 15714-15721.

88. Cesar, I.; Kay, A.; Gonzalez Martinez, J. A.; Grätzel, M., Translucent thin film Fe_2O_3 photoanodes for efficient water splitting by sunlight: nanostructure-directing effect of Si-doping. *Journal of the American Chemical Society* **2006**, *128*, 4582-4583.
89. Paracchino, A.; Laporte, V.; Sivula, K.; Grätzel, M.; Thimsen, E., Highly active oxide photocathode for photoelectrochemical water reduction. *Nature Materials* **2011**, *10*, 456-461.
90. Kölbach, M.; Pereira, I. J.; Harbauer, K.; Plate, P.; Höflich, K.; Berglund, S. P.; Friedrich, D.; van de Krol, R.; Abdi, F. F., Revealing the performance-limiting factors in α-$SnWO_4$ photoanodes for solar water splitting. *Chemistry of Materials* **2018**, *30*, 8322-8331.
91. Kölbach, M.; Hempel, H.; Harbauer, K.; Schleuning, M.; Petsiuk, A.; Höflich, K.; Deinhart, V.; Friedrich, D.; Eichberger, R.; Abdi, F. F.; van de Krol, R., Grain boundaries limit the charge carrier transport in pulsed laser deposited α-$SnWO_4$ thin film photoabsorbers. *ACS Applied Energy Materials* **2020**, *3*, 4320-4330.
92. Schnell, P.; Kölbach, M.; Schleuning, M.; Obata, K.; Irani, R.; Ahmet, I. Y.; Harb, M.; Starr, D. E.; van de Krol, R.; Abdi, F. F., Interfacial oxide formation limits the photovoltage of α-$SnWO_4$/NiO_x photoanodes prepared by pulsed laser deposition. *Advanced Energy Materials* **2021**, *11*, 2003183.
93. Yang, W.; Prabhakar, R. R.; Tan, J.; Tilley, S. D.; Moon, J., Strategies for enhancing the photocurrent, photovoltage, and stability of photoelectrodes for photoelectrochemical water splitting. *Chemical Society Reviews* **2019**, *48*, 4979-5015.
94. Kudo, A.; Omori, K.; Kato, H., A novel aqueous process for preparation of crystal form-controlled and highly crystalline $BiVO_4$ powder from layered vanadates at room temperature and its photocatalytic and photophysical properties. *Journal of the American Chemical Society* **1999**, *121*, 11459-11467.
95. Parmar, K. P. S.; Kang, H. J.; Bist, A.; Dua, P.; Jang, J. S.; Lee, J. S., Photocatalytic and photoelectrochemical water oxidation over metal-doped monoclinic $BiVO_4$ photoanodes. *ChemSusChem* **2012**, *5*, 1926-1934.
96. Chen, L.; Toma, F. M.; Cooper, J. K.; Lyon, A.; Lin, Y.; Sharp, I. D.; Ager, J. W., Mo-doped $BiVO_4$ photoanodes synthesized by reactive sputtering. *ChemSusChem* **2015**, *8*, 1066-1071.
97. Hahn, N. T.; Mullins, C. B., Photoelectrochemical performance of nanostructured Ti- and Sn-doped α-Fe_2O_3 photoanodes. *Chemistry of Materials* **2010**, *22*, 6474-6482.
98. Song, J.; Seo, M. J.; Lee, T. H.; Jo, Y.-R.; Lee, J.; Kim, T. L.; Kim, S.-Y.; Kim, S.-M.; Jeong, S. Y.; An, H.; Kim, S.; Lee, B. H.; Lee, D.; Jang, H. W.; Kim, B.-J.; Lee, S., Tailoring crystallographic orientations to substantially enhance charge separation efficiency in anisotropic $BiVO_4$ photoanodes. *ACS Catalysis* **2018**, *8*, 5952-5962.
99. Kim, T. W.; Choi, K.-S., Nanoporous $BiVO_4$ photoanodes with dual-layer oxygen evolution catalysts for solar water splitting. *Science* **2014**, *343*, 990-994.
100. Pihosh, Y.; Turkevych, I.; Mawatari, K.; Uemura, J.; Kazoe, Y.; Kosar, S.; Makita, K.; Sugaya, T.; Matsui, T.; Fujita, D.; Tosa, M.; Kondo, M.; Kitamori, T., Photocatalytic generation of hydrogen by core-shell WO_3/$BiVO_4$ nanorods with ultimate water splitting efficiency. *Scientific Reports* **2015**, *5*, 11141.
101. Osterloh, F. E., Inorganic nanostructures for photoelectrochemical and photocatalytic water splitting. *Chemical Society Reviews* **2013**, *42*, 2294-2320.
102. Jang, J.-W.; Friedrich, D.; Müller, S.; Lamers, M.; Hempel, H.; Lardhi, S.; Cao, Z.; Harb, M.; Cavallo, L.; Heller, R.; Eichberger, R.; van de Krol, R.; Abdi, F. F., Enhancing charge carrier lifetime in metal oxide photoelectrodes through mild hydrogen treatment. *Advanced Energy Materials* **2017**, *7*, 1701536.
103. Zhong, M.; Hisatomi, T.; Kuang, Y.; Zhao, J.; Liu, M.; Iwase, A.; Jia, Q.; Nishiyama, H.; Minegishi, T.; Nakabayashi, M.; Shibata, N.; Niishiro, R.; Katayama, C.; Shibano, H.; Katayama, M.; Kudo, A.; Yamada, T.; Domen, K., Surface modification of CoO_x loaded $BiVO_4$ photoanodes with ultrathin p-type NiO layers for improved solar water oxidation. *Journal of the American Chemical Society* **2015**, *137*, 5053-5060.

104. Abdi, F. F.; van de Krol, R., Nature and light dependence of bulk recombination in Co-Pi-catalyzed $BiVO_4$ photoanodes. *The Journal of Physical Chemistry C* **2012**, *116*, 9398-9404.
105. Kim, M.; Lee, B.; Ju, H.; Kim, J. Y.; Kim, J.; Lee, S. W., Oxygen-vacancy-introduced $BaSnO_{3-\delta}$ photoanodes with tunable band structures for efficient solar-driven water splitting. *Advanced Materials* **2019**, *31*, 1903316.
106. Brillet, J.; Yum, J.-H.; Cornuz, M.; Hisatomi, T.; Solarska, R.; Augustynski, J.; Graetzel, M.; Sivula, K., Highly efficient water splitting by a dual-absorber tandem cell. *Nature Photonics* **2012**, *6*, 824-828.
107. Dias, P.; Schreier, M.; Tilley, S. D.; Luo, J.; Azevedo, J.; Andrade, L.; Bi, D.; Hagfeldt, A.; Mendes, A.; Grätzel, M.; Mayer, M. T., Transparent cuprous oxide photocathode enabling a stacked tandem cell for unbiased water splitting. *Advanced Energy Materials* **2015**, *5*, 1501537.
108. Ahmet, I. Y.; Berglund, S.; Chemseddine, A.; Bogdanoff, P.; Präg, R. F.; Abdi, F. F.; van de Krol, R., Planar and nanostructured n-Si/metal-oxide/WO_3/$BiVO_4$ monolithic tandem devices for unassisted solar water splitting. *Advanced Energy and Sustainability Research* **2020**, *1*, 2000037.
109. Abdi, F. F.; Han, L.; Smets, A. H.; Zeman, M.; Dam, B.; van de Krol, R., Efficient solar water splitting by enhanced charge separation in a bismuth vanadate-silicon tandem photoelectrode. *Nature Communications* **2013**, *4*, 2195.
110. Kayla J. Pyper, T. C. E., Bart M. Bartlett, Synthesis of $SnWO_4$ thin-film electrodes by hydrothermal conversion from crystalline WO_3. *Chinese Chemical Letters* **2015**, *26*, 474-478.
111. Harb, M.; Ziani, A.; Takanabe, K., Critical difference between optoelectronic properties of α- and β-$SnWO_4$ semiconductors: A DFT/HSE06 and axperimental investigation. *physica status solidi (b)* **2016**, *253*, 1115-1119.
112. A. Kuzmin, A. A., A. Kalinko, J. Timoshenko, R. Kalendarev, External pressure and composition effects on the atomic and electronic structure of $SnWO_4$. *Solar Energy Materials and Solar Cells* **2015**, *143*, 627-634.
113. Zhu, Z.; Sarker, P.; Zhao, C.; Zhou, L.; Grimm, R. L.; Huda, M. N.; Rao, P. M., Photoelectrochemical properties and behavior of α-$SnWO_4$ photoanodes synthesized by hydrothermal conversion of WO_3 Films. *ACS Applied Materials & Interfaces* **2017**, *9*, 1459-1470.
114. Ziani, A.; Harb, M.; Noureldine, D.; Takanabe, K., UV-Vis optoelectronic properties of α-$SnWO_4$: A comparative experimental and density functional theory based study. *APL Materials* **2015**, *3*, 096101.
115. Bozheyev, F.; Akinoglu, E. M.; Wu, L.; Lu, H.; Nemkayeva, R.; Xue, Y.; Jin, M.; Giersig, M., Band gap optimization of tin tungstate thin films for solar water oxidation. *International Journal of Hydrogen Energy* **2020**, *45*, 8676-8685.
116. Cho, I.-S.; Kwak, C. H.; Kim, D. W.; Lee, S.; Hong, K. S., Photophysical, photoelectrochemical, and photocatalytic properties of novel $SnWO_4$ oxide semiconductors with narrow band gaps. *Journal of Physical Chemistry C* **2009**, *113*, 10647-10653.
117. Harb, M.; Cavallo, L.; Basset, J.-M., Remarkable influence of α-$SnWO_4$ exposed facets on their photocatalytic performance for H_2 and O_2 evolution reactions. *The Journal of Physical Chemistry C* **2020**, *124*, 18684-18689.
118. Kölbach, M., Pulsed Laser Deposition of Efficient Ternary Metal Oxide Photoelectrodes. Doctoral Thesis, TU Berlin, **2019**.
119. Allen J. Bard, A. B. B., Fu-Ren F. Fan, Erick G. Walton, and Mark S. Wrighton, The Concept of fermi level pinning at semiconductor/liquid junctions. Consequences for energy conversion efficiency and selection of useful solution redox couples in solar devices. *Journal of the American Chemical Society* **1980**, *102*, 3671-3677.
120. Lewerenz, H. J., Surface states and fermi level pinning at semiconductor/ electrolyte junctions. *Journal of Electroanalytical Chemistry* **1993**, *356*, 121-143.
121. Bardeen, J., Surface states and rectification at a metal semi-conductor contact. *Physical Review* **1947**, *71*, 717-727.

122. Shockley, W., On the surface states associated with a periodic potential. *Physical Review* **1939**, *56*, 317-323.
123. Schottky, W., Zur Halbleitertheorie der Sperrschicht- und Spitzengleichrichter. *Zeitschrift für Physik* **1939**, *113*, 367-414.
124. Mott, N. F., The theory of crystal rectifiers. *Proceedings of the Royal Society of London. Series A. Mathematical and Physical Sciences* **1939**, *171*, 27-38.
125. Sivula, K., Metal oxide photoelectrodes for solar fuel production, surface traps, and catalysis. *The Journal of Physical Chemistry Letters* **2013**, *4*, 1624-1633.
126. Li, Z.; Luo, W.; Zhang, M.; Feng, J.; Zou, Z., Photoelectrochemical cells for solar hydrogen production: current state of promising photoelectrodes, methods to improve their properties, and outlook. *Energy & Environmental Science* **2013**, *6*, 347-370.
127. Gerischer, H., Electrolytic decomposition and photodecomposition of compound semiconductors in contact with electrolytes. *Journal of Vacuum Science and Technology* **1978**, *15*, 1422-1428.
128. Gerischer, H., On the stability of semiconductor electrodes against photodecomposition. *Journal of Electroanalytical Chemistry and Interfacial Electrochemistry* **1977**, *82*, 133-143.
129. Pourbaix, M., *Atlas of Electrochemical Equilibria in Aqueous Solutions*; Pergamon Press Ltd.: London, **1966**.
130. Park, S.-M.; Barber, M. E., Thermodynamic stabilities of semiconductor electrodes. *Journal of Electroanalytical Chemistry and Interfacial Electrochemistry* **1979**, *99*, 67-75.
131. Kim, J. H.; Hansora, D.; Sharma, P.; Jang, J.-W.; Lee, J. S., Toward practical solar hydrogen production – an artificial photosynthetic leaf-to-farm challenge. *Chemical Society Reviews* **2019**, *48*, 1908-1971.
132. Bae, D.; Seger, B.; Vesborg, P. C.; Hansen, O.; Chorkendorff, I., Strategies for stable water splitting via protected photoelectrodes. *Chemical Society Reviews* **2017**, *46*, 1933-1954.
133. Lowndes, D. H.; Geohegan, D. B.; Puretzky, A. A.; Norton, D. P.; Rouleau, C. M., Synthesis of novel thin-film materials by pulsed laser deposition. *Science* **1996**, *273*, 898-903.
134. Willmott, P. R.; Huber, J. R., Pulsed laser vaporization and deposition. *Reviews of Modern Physics* **2000**, *72*, 315-328.
135. Eason, R., *Pulsed Laser Deposition of Thin Films*; Wiley, **2007**.
136. Schou, J., Physical aspects of the pulsed laser deposition technique: the stoichiometric transfer of material from target to film. *Applied Surface Science* **2009**, *255*, 5191-5198.
137. Kölbach, M.; Harbauer, K.; Ellmer, K.; van de Krol, R., Elucidating the pulsed laser deposition process of $BiVO_4$ photoelectrodes for solar water splitting. *The Journal of Physical Chemistry C* **2020**, *124*, 4438-4447.
138. Herklotz, A.; Dörr, K.; Ward, T. Z.; Eres, G.; Christen, H. M.; Biegalski, M. D., Stoichiometry control of complex oxides by sequential pulsed-laser deposition from binary-oxide targets. *Applied Physics Letters* **2015**, *106*, 131601.
139. Yang, A.; Chen, Z.; Islam, S. M.; Vittoria, C.; Harris, V. G., Cation engineering of Cu-ferrite films deposited by alternating target laser ablation deposition. *Journal of Applied Physics* **2008**, *103*, 07E509.
140. Smith, H. M.; Turner, A. F., Vacuum deposited thin films using a ruby laser. *Appl. Opt.* **1965**, *4*, 147-148.
141. Lorenz, M.; Ramachandra Rao, M. S., 25 Years of Pulsed Laser Deposition. *Journal of Physics D: Applied Physics* **2013**, *47*, 030301.
142. Dijkkamp, D.; Venkatesan, T.; Wu, X. D.; Shaheen, S. A.; Jisrawi, N.; Min-Lee, Y. H.; McLean, W. L.; Croft, M., Preparation of Y-Ba-Cu oxide superconductor thin films using pulsed laser evaporation from high T_c bulk material. *Applied Physics Letters* **1987**, *51*, 619-621.
143. Greer, J. A., History and current status of commercial pulsed laser deposition equipment. *Journal of Physics D: Applied Physics* **2013**, *47*, 034005.

144. Yamamoto, S.; Sumita, T.; Sugiharuto; Miyashita, A.; Naramoto, H., Preparation of epitaxial TiO_2 films by pulsed laser deposition technique. *Thin Solid Films* **2001**, *401*, 88-93.
145. Scherrer, B.; Li, T.; Tsyganok, A.; Döbeli, M.; Gupta, B.; Malviya, K. D.; Kasian, O.; Maman, N.; Gault, B.; Grave, D. A.; Mehlman, A.; Visoly-Fisher, I.; Raabe, D.; Rothschild, A., Defect segregation and its effect on the photoelectrochemical properties of Ti-doped hematite photoanodes for solar water splitting. *Chemistry of Materials* **2020**, *32*, 1031-1040.
146. Malviya, K. D.; Klotz, D.; Dotan, H.; Shlenkevich, D.; Tsyganok, A.; Mor, H.; Rothschild, A., Influence of Ti doping levels on the photoelectrochemical properties of thin-film hematite (α-Fe_2O_3) photoanodes. *The Journal of Physical Chemistry C* **2017**, *121*, 4206-4213.
147. Zhang, S.; Ahmet, I.; Kim, S.-H.; Kasian, O.; Mingers, A. M.; Schnell, P.; Kölbach, M.; Lim, J.; Fischer, A.; Mayrhofer, K. J. J.; Cherevko, S.; Gault, B.; van de Krol, R.; Scheu, C., Different photostability of $BiVO_4$ in near-pH-neutral electrolytes. *ACS Applied Energy Materials* **2020**, *3*, 9523-9527.
148. Gottesman, R.; Levine, I.; Schleuning, M.; Irani, R.; Abou-Ras, D.; Dittrich, T.; Friedrich, D.; van de Krol, R., Overcoming phase-purity challenges in complex metal oxide photoelectrodes: a case study of $CuBi_2O_4$. *Advanced Energy Materials* **2021**, *11*, 2003474.
149. Fàbrega, C.; Murcia-López, S.; Monllor-Satoca, D.; Prades, J. D.; Hernández-Alonso, M. D.; Penelas, G.; Morante, J. R.; Andreu, T., Efficient WO_3 photoanodes fabricated by pulsed laser deposition for photoelectrochemical water splitting with high faradaic efficiency. *Applied Catalysis B: Environmental* **2016**, *189*, 133-140.
150. Grave, D. A.; Dotan, H.; Levy, Y.; Piekner, Y.; Scherrer, B.; Malviya, K. D.; Rothschild, A., Heteroepitaxial hematite photoanodes as a model system for solar water splitting. *Journal of Materials Chemistry A* **2016**, *4*, 3052-3060.
151. Grave, D. A.; Klotz, D.; Kay, A.; Dotan, H.; Gupta, B.; Visoly-Fisher, I.; Rothschild, A., Effect of orientation on bulk and surface properties of Sn-doped hematite (α-Fe_2O_3) heteroepitaxial thin film photoanodes. *The Journal of Physical Chemistry C* **2016**, *120*, 28961-28970.
152. Lee, D.; Wang, W.; Zhou, C.; Tong, X.; Liu, M.; Galli, G.; Choi, K.-S., The impact of surface composition on the interfacial energetics and photoelectrochemical properties of $BiVO_4$. *Nature Energy* **2021**, *6*, 287-294.
153. Einstein, A., Über einen die Erzeugung und Verwandlung des Lichtes betreffenden heuristischen Gesichtspunkt. *Annalen der Physik* **1905**, *322*, 132-148.
154. Klein, A.; Mayer, T.; Thissen, A.; Jaegermann, W., Photoelectron spectroscopy in materials science and physical chemistry: analysis of composition, chemical Bonding and electronic structure of surfaces and interfaces. *Bunsen-Magazin* **2008**, *10*, 124-139.
155. Hüfner, S., *Photoelectron Spectroscopy: Principles and Applications*; Springer, **2003**.
156. Gorgoi, M; Svensson, S.; Schäfers, F.; Öhrwall, G.; Mertin, M.; Bressler, P.; Karis, O.; Siegbahn, H.; Sandell, A.; Rensmo, H.; Doherty, W.; Jung, C.; Braun, W.; Eberhardt, W., The high kinetic energy photoelectron spectroscopy facility at BESSY progress and first results. *Nuclear Instruments and Methods in Physics Research Section A: Accelerators, Spectrometers, Detectors and Associated Equipment* **2009**, *601*, 48-53.
157. Schaefers, F.; Mertin, M.; Gorgoi, M., KMC-1: a high resolution and high flux soft X-ray beamline at BESSY. *Review of Scientific Instruments* **2007**, *78*, 123102.
158. Zachäus, C. Water Oxidation Catalysts: Mechanism and Their Interaction at the Semiconductor-Electrolyte Interface. Doctoral Thesis, TU Berlin, **2016**.
159. Fischer Scientific, ICP-OES Systems and Technologies. https://www.thermofisher.com /de/de/home/industrial/spectroscopy-elemental-isotope-analysis/spectroscopy-elemental-isotope-analysis-learning-center/trace-elemental-analysis-tea-information/icp-oes-information/icp-oes-system-technologies.html. (accessed 13.07.2021)
160. Gottesman, R.; Song, A.; Levine, I.; Krause, M.; Islam, A. T. M. N.; Abou-Ras, D.; Dittrich, T.; van de Krol, R.; Chemseddine, A., Pure $CuBi_2O_4$ photoelectrodes with increased stability by

rapid thermal processing of Bi_2O_3/CuO grown by pulsed laser deposition. *Advanced Functional Materials* **2020**, *30*, 1910832.
161. Song, A.; Levine, I.; van de Krol, R.; Dittrich, T.; Berglund, S. P., Revealing the relationship between photoelectrochemical performance and interface hole trapping in $CuBi_2O_4$ heterojunction photoelectrodes. *Chemical Science* **2020**, *11*, 11195-11204.
162. Brattain, W. H., Evidence for surface states on semiconductors from change in contact potential on illumination. *Physical Review* **1947**, *72*, 345.
163. Brattain, W. H.; Bardeen, J., Surface properties of germanium. *The Bell System Technical Journal* **1953**, *32*, 1-41.
164. Kronik, L.; Shapira, Y., Surface photovoltage phenomena: theory, experiment, and applications. *Surface Science Reports* **1999**, *37*, 1-206.
165. Chen, R.; Fan, F.; Dittrich, T.; Li, C., Imaging photogenerated charge carriers on surfaces and interfaces of photocatalysts with surface photovoltage microscopy. *Chemical Society Reviews* **2018**, *47*, 8238-8262.
166. Dittrich, T.; Fengler, S., *Surface Photovoltage Analysis of Photoactive Materials*; World Scientific, **2019**.
167. Park, Y.; McDonald, K. J.; Choi, K.-S., Progress in bismuth vanadate photoanodes for use in solar water oxidation. *Chemical Society Reviews* **2013**, *42*, 2321-2337.
168. Klahr, B.; Hamann, T., Water oxidation on hematite photoelectrodes: insight into the nature of surface states through in situ spectroelectrochemistry. *The Journal of Physical Chemistry C* **2014**, *118*, 10393-10399.
169. Prévot, M. S.; Jeanbourquin, X. A.; Bourée, W. S.; Abdi, F.; Friedrich, D.; van de Krol, R.; Guijarro, N.; Le Formal, F.; Sivula, K., Evaluating charge carrier transport and surface States in $CuFeO_2$ photocathodes. *Chemistry of Materials* **2017**, *29*, 4952-4962.
170. Irani, R.; Plate, P.; Höhn, C.; Bogdanoff, P.; Wollgarten, M.; Höflich, K.; van de Krol, R.; Abdi, F. F., The role of ultra-thin MnO_x co-catalysts on the photoelectrochemical properties of $BiVO_4$ photoanodes. *Journal of Materials Chemistry A* **2020**, *8*, 5508-5516.
171. Hermans, Y.; Murcia-López, S.; Klein, A.; van de Krol, R.; Andreu, T.; Morante, J. R.; Toupance, T.; Jaegermann, W., Analysis of the interfacial characteristics of $BiVO_4$/metal oxide heterostructures and its implication on their junction properties. *Physical Chemistry Chemical Physics* **2019**, *21*, 5086-5096.
172. Digdaya, I. A.; Adhyaksa, G. W. P.; Trzésniewski, B. J.; Garnett, E. C.; Smith, W. A., Interfacial engineering of metal-insulator-semiconductor junctions for efficient and stable photoelectrochemical water oxidation. *Nature Communications* **2017**, *8*, 15968.
173. Lewerenz, H. J., Surface states and fermi level pinning at semiconductor/electrolyte interfaces. *Journal of Electroanalytical Chemistry* **1993**, *365*, 121-143.
174. Lee, S. W.; Lee, Y. S.; Heo, J.; Siah, S. C.; Chua, D.; Brandt, R. E.; Kim, S. B.; Mailoa, J. P.; Buonassisi, T.; Gordon, R. G., Improved Cu_2O-based solar cells using atomic layer deposition to control the Cu oxidation state at the p-n junction. *Advanced Energy Materials* **2014**, *4*, 1301916.
175. Lu, J.; Aarik, J.; Sundqvist, J.; Kukli, K.; Hårsta, A.; Carlsson, J.-O., Analytical TEM characterization of the interfacial Llayer between ALD HfO_2 film and silicon substrate. *Journal of Crystal Growth* **2005**, *273*, 510-514.
176. Ding, X.; Wang, X.; Feng, Y.; Shen, W.; Liu, L., Low operation current of Si/HfO_2 double layers based RRAM device with insertion of Si film. *Japanese Journal of Applied Physics* **2020**, *59*, SGGB16.
177. Kuzmin, A.; Zubkins, M.; Kalendarev, R., Preparation and characterization of tin tungstate thin films. *Ferroelectrics* **2015**, *484*, 49-54.
178. McColm, I. J.; Steadman, R.; Howe, A., Preparation, structure, and mössbauer spectra of tin tungsten bronzes. *Journal of Solid State Chemistry* **1970**, *2*, 555-562.

179. Jain, A.; Jain, A.; Ong, S. P.; Hautier, G.; Chen, W.; Richards, W. D.; Dacek, S.; Cholia, S.; Gunter, D.; Skinner, D.; Ceder, G.; Persson, K. A., Commentary: the Materials Project: a materials genome approach to accelerating materials innovation. *APL Materials* **2013**, *1*, 011002.
180. Smekal, W.; Werner, W. S. M.; Powell, C. J., Simulation of electron spectra for surface analysis (SESSA): a novel software tool for quantitative Auger-electron spectroscopy and X-ray photoelectron spectroscopy. *Surface and Interface Analysis* **2005**, *37*, 1059-1067.
181. Magomedov, A.; Al-Ashouri, A.; Kasparavičius, E.; Strazdaite, S.; Niaura, G.; Jošt, M.; Malinauskas, T.; Albrecht, S.; Getautis, V., Self-assembled hole transporting monolayer for highly efficient perovskite solar cells. *Advanced Energy Materials* **2018**, *8*, 1801892.
182. Al-Ashouri, Magomedov, A.; Roß, M.; Jošt, M.; Talaikis, M.; Chistiakova, G.; Bertram, T.; Márquez, J. A.; Köhnen, E.; Kasparavičius, E.; Levcenco, S.; Gil-Escrig, L.; Hages, C. J.; Schlatmann, R.; Rech, B.; Malinauskas, T.; Unold, T.; Kaufmann, C. A.; Korte, L.; Niaura, G.; Getautis, V.; Albrecht, S., Conformal monolayer contacts with lossless interfaces for perovskite single junction and monolithic tandem solar cells. *Energy & Environmental Science* **2019**, *12*, 3356-3369.
183. Le Formal, F.; Tétreault, N.; Cornuz, M.; Moehl, T.; Grätzel, M.; Sivula, K., Passivating surface states on water splitting hematite photoanodes with alumina overlayers. *Chemical Science* **2011**, *2*, 737-743.
184. Dittrich, T.; Awino, C.; Prajongtat, P.; Rech, B.; Lux-Steiner, M. C., Temperature dependence of the band gap of $CH_3NH_3PbI_3$ stabilized with PMMA: A modulated surface photovoltage study. *The Journal of Physical Chemistry C* **2015**, *119*, 23968-23972.
185. Xie, M.; Fu, X.; Jing, L.; Luan, P.; Feng, Y.; Fu, H., Long-lived, visible-light-excited charge carriers of TiO_2/$BiVO_4$ nanocomposites and their unexpected photoactivity for water splitting. *Advanced Energy Materials* **2014**, *4*, 1300995.
186. Zhang, X.; Zhang, L.; Xie, T.; Wang, D., Low-temperature synthesis and high visible-light-induced photocatalytic activity of BiOI/TiO_2 heterostructures. *The Journal of Physical Chemistry C* **2009**, *113*, 7371-7378.
187. Dittrich, T.; Gonzáles, A.; Rada, T.; Rissom, T.; Zillner, E.; Sadewasser, S.; Lux-Steiner, M., Comparative study of Cu(In,Ga)Se_2/CdS and Cu(In,Ga)Se_2/In_2S_3 systems by surface photovoltage techniques. *Thin Solid Films* **2013**, *535*, 357-361.
188. Favaro, M.; Uecker, R.; Nappini, S.; Píš, I.; Magnano, E.; Bluhm, H.; van de Krol, R.; Starr, D. E., Chemical, structural, and electronic characterization of the (010) surface of single crystalline bismuth vanadate. *The Journal of Physical Chemistry C* **2019**, *123*, 8347-8359.
189. Jovic, V.; Laverock, J.; Rettie, A. J. E.; Zhou, J. S.; Mullins, C. B.; Singh, V. R.; Lamoureux, B.; Wilson, D.; Su, T. Y.; Jovic, B.; Bluhm, H.; Söhnel, T.; Smith, K. E., Soft X-ray spectroscopic studies of the electronic structure of M: $BiVO_4$ (M = Mo, W) single crystals. *Journal of Materials Chemistry A* **2015**, *3*, 23743-23753.
190. Jovic, V.; Rettie, A. J. E.; Singh, V. R.; Zhou, J.; Lamoureux, B.; Buddie Mullins, C.; Bluhm, H.; Laverock, J.; Smith, K. E., A soft X-ray spectroscopic perspective of electron localization and transport in tungsten doped bismuth vanadate single crystals. *Physical Chemistry Chemical Physics* **2016**, *18*, 31958-31965.
191. Gatos, H. C.; Lagowski, J., Surface photovoltage spectroscopy—a new approach to the study of high-gap semiconductor surfaces. *Journal of Vacuum Science and Technology* **1973**, *10*, 130-135.
192. Balestra, C. L.; Łagowski, J.; Gatos, H. C., Determination of surface state energy positions by surface photovoltage spectrometry: CdS. *Surface Science* **1971**, *26*, 317-320.
193. Liu, Z.; Handa, K.; Kaibuchi, K.; Tanaka, Y.; Kawai, J., Comparison of the Sn L edge X-ray absorption spectra and the corresponding electronic structure in Sn, SnO, and SnO_2. *Journal of Electron Spectroscopy and Related Phenomena* **2004**, *135*, 155-158.
194. Bianconi, A., Surface X-ray absorption spectroscopy: surface EXAFS and surface XANES. *Applications of Surface Science* **1980**, *6*, 392-418.

195. Grządziel, L.; Krzywiecki, M.; Szwajca, A.; Sarfraz, A.; Genchev, G.; Erbe, A., Detection of intra-band gap defects states in spin-coated sol-gel SnO_x nanolayers by photoelectron spectroscopies. *Journal of Physics D: Applied Physics* **2018**, *51*, 315301.
196. Cox, D. F.; Fryberger, T. B.; Semancik, S., Oxygen vacancies and defect electronic states on the SnO_2 (110)-1x1 surface. *Physical Review B* **1988**, *38*, 2072-2083.
197. Haeberle, J.; Machulik, S.; Janowitz, C.; Manzke, R.; Gaspar, D.; Barquinha, P.; Schmeißer, D., Gap states in the electronic structure of SnO_2 single crystals and amorphous SnO_x thin films. *Journal of Applied Physics* **2016**, *120*, 105101.
198. Themlin, J. M.; Sporken, R.; Darville, J.; Caudano, R.; Gilles, J. M.; Johnson, R. L., Resonant-photoemission study of SnO_2: cationic origin of the defect band-gap states. *Physical Review B* **1990**, *42*, 11914-11925.
199. Trani, F.; Causà, M.; Ninno, D.; Cantele, G.; Barone, V., Density functional study of oxygen vacancies at the SnO_2 surface and subsurface sites. *Physical Review B* **2008**, *77*, 245410.
200. Kılıç, Ç.; Zunger, A., Origins of coexistence of conductivity and transparency in SnO_2. *Physical Review Letters* **2002**, *88*, 095501.
201. Gerischer, H., On the stability of semiconductor electrodes against photodecomposition. *Journal of Electroanalytical Chemistry and Interfacial Electrochemistry* **1977**, *82*, 133-143.
202. Hu, S.; Shaner, M. R.; Beardslee, J. A.; Lichterman, M.; Brunschwig, B. S.; Lewis, N. S., Amorphous TiO_2 coatings stabilize Si, GaAs, and GaP photoanodes for efficient water oxidation. *Science* **2014**, *344*, 1005-1009.
203. Seger, B.; Pedersen, T.; Laursen, A. B.; Vesborg, P. C. K.; Hansen, O.; Chorkendorff, I., Using TiO_2 as a conductive protective layer for photocathodic H_2 evolution. *Journal of the American Chemical Society* **2013**, *135*, 1057-1064.
204. Lee, D. K.; Choi, K.-S., Enhancing long-term photostability of $BiVO_4$ photoanodes for solar water splitting by tuning electrolyte composition. *Nature Energy* **2018**, *3*, 53-60.
205. Nandjou, F.; Haussener, S., Degradation in photoelectrochemical devices: review with an illustrative case study. *Journal of Physics D: Applied Physics* **2017**, *50*, 124002.
206. Toma, F. M.; Cooper, J. K.; Kunzelmann, V.; McDowell, M. T.; Yu, J.; Larson, D. M.; Borys, N. J.; Abelyan, C.; Beeman, J. W.; Yu, K. M.; Yang, J.; Chen, L.; Shaner, M. R.; Spurgeon, J.; Houle, F. A.; Persson, K. A.; Sharp, I. D., Mechanistic insights into chemical and photochemical transformations of bismuth vanadate photoanodes. *Nature Communications* **2016**, *7*, 12012.
207. Berglund, S. P.; Abdi, F. F.; Bogdanoff, P.; Chemseddine, A.; Friedrich, D.; van de Krol, R., Comprehensive evaluation of $CuBi_2O_4$ as a photocathode material for photoelectrochemical water splitting. *Chemistry of Materials* **2016**, *28*, 4231-4242.
208. Kang, D.; Hill, J. C.; Park, Y.; Choi, K.-S., Photoelectrochemical properties and photostabilities of high surface area $CuBi_2O_4$ and Ag-doped $CuBi_2O_4$ photocathodes. *Chemistry of Materials* **2016**, *28*, 4331-4340.
209. Sivula, K.; Le Formal, F.; Grätzel, M., Solar water splitting: progress using hematite (α-Fe_2O_3) photoelectrodes. *ChemSusChem* **2011**, *4*, 432-449.
210. Peerakiatkhajohn, P.; Yun, J.-H.; Chen, H.; Lyu, M.; Butburee, T.; Wang, L., Stable hematite nanosheet photoanodes for enhanced photoelectrochemical water splitting. *Advanced Materials* **2016**, *28*, 6405-6410.
211. Mi, Q.; Zhanaidarova, A.; Brunschwig, B. S.; Gray, H. B.; Lewis, N. S., A quantitative assessment of the competition between water and anion oxidation at WO_3 photoanodes in acidic aqueous electrolytes. *Energy & Environmental Science* **2012**, *5*, 5694-5700.
212. Hill, J. C.; Choi, K.-S., Effect of electrolytes on the selectivity and stability of n-type WO_3 photoelectrodes for use in solar water oxidation. *The Journal of Physical Chemistry C* **2012**, *116*, 7612-7620.

213. Gerrard, W. A., Photoelectrolysis using a tungsten oxide anode in chlorine and sulphate solutions. *Journal of Electroanalytical Chemistry and Interfacial Electrochemistry* **1978**, *86*, 421-424.
214. Persson, K. A.; Waldwick, B.; Lazic, P.; Ceder, G., Prediction of solid-aqueous equilibria: scheme to combine first-principles calculations of solids with experimental aqueous states. *Physical Review B* **2012**, *85*, 235438.
215. Biesinger, M. C.; Payne, B. P.; Lau, L. W. M.; Gerson, A.; Smart, R. S. C., X-Ray photoelectron spectroscopic chemical state quantification of mixed nickel metal, oxide and hydroxide systems. *Surface and Interface Analysis* **2009**, *41*, 324-332.

F. List of Figures

Acknowledgement

Without the support of numerous people, the completion of a PhD project is, of course, not possible. First of all, I would like to thank Prof. Dr. Roel van de Krol and Dr. Fatwa F. Abdi for giving me the opportunity to conduct this PhD project and the constant guidance and support. From the first moment of the interview on, it was clear for me that it will be a fruitful collaboration. I thank Dr. Fatwa Abdi for the regular discussions that were always a source for inspiration.

For being a reviewer of my thesis, I would like to acknowledge Prof. Dr. Menny Shalom. For kindly taking over the chair of the promotion committee, I would like to thank Prof. Dr. Matthias Drieß.

I would like to thank the Helmholtz international research school (HI-SCORE) for funding of this project and the organization of meeting and seminar talks. Also, I would like to acknowledge the MatSEC (Materials for solar energy conversion) graduate school for organization of meetings and retreats, although in the second half of my PhD everything had to take place online. Finally, I would like to my fellow HI-SCORE and MatSEC colleagues.

An important outcome of this thesis are the synchrotron measurements. Performing the measurements at BESSY would not have been possible without a strong team that also willingly worked on the weekends and took over night shifts. I would like to thank Dr. Fatwa F. Abdi, Dr. Moritz Kölbach, Markus Schleuning, Dr. Rowshanak Irani, Dr. Keisuke Obata, Dr. Ibbi Y. Ahmet, Erwin Fernandez and Jennifer Velázquez Rojas. For the technical assistance at the beamline, I would like to thank Dr. Roberto Felix Duarte and Dr. Regan Wilks.

As often in science, the interpretation of experimental data is more comprehensible with the addition of theoretical calculations. I would like to Dr. Moussab Harb for helping us with the DFT calculations.

Without the necessary technical equipment, this work would of course not have been possible. And the same goes for the people that are taking care of the equipment. I would like to thank our engineers and technicians Karsten Harbauer, Christian Höhn and Ursula Michalczik for the assistance with the PLD, XPS and ICP-OES.

For assistance in the XRD core lab I would like to thank René Gunder and Dr. Michael Tovar.

For the assistance with the SPV measurement I would like to thank Dr. Tomas Dittrich and Tamar Grosz.

I also would like to thank my fellow Master, PhD and Postdoc colleagues at the institute for solar fuels at Helmholtz-Zentrum Berlin: Dr. Moritz Kölbach, Markus Schleuning, Dr. Rowshanak Irani, Dr. Keisuke Obata, Dr. Ibbi Y. Ahmet, Soniya Gahlawat, Erwin Fernandez, Jennifer Velázquez Rojas, Raphael Präg, Tamar Grosz, Dr. Marlene Lamers, J. Mark C. M. Dela Cruz, Dr. Prince Bassi, Dr. Ronen Gottesman. The time is short while I'm writing this, so I hope that I didn't forget anyone. Although it was challenging to work collaboratively under the conditions of the pandemic we still managed to be productive. I would like to thank J. Mark C. M. Dela Cruz who worked with me as a Master student.

Finally, I also would like to thank everyone else who supported me outside of work, most notable my friends and family.